Check for updates

Recent progress in water-splitting and supercapacitor electrode materials based on MOF-derived sulfides

Matheus I. da Silva, [iD] Ítalo R. Machado, [iD] Henrique E. Toma, [iD] Koiti Araki, [iD] Lucio Angnes [iD]* and Josué M. Gonçalves [iD]*

Metal–organic frameworks (MOFs) are being extensively reported as ideal templates or precursors for energy storage and conversion materials thanks to their unique architectures with high surface area, high ordered porosity, the concentration of heteroatoms, and adjustable structures, allied with the possibility of carrying out chemical processes while preserving their structure and enhancing or incorporating new properties, and essential features for the rational design of multifunctional electrode materials for energy technologies. In fact, MOF-derived materials exhibit versatile nanostructures, outstanding electrochemical performances and stability, overcoming the relatively low conductivity of MOF precursors. In this review, the recent progress on MOF-derived sulfide-based electrode materials for energy applications are summarized. The main strategies used for the design of MOF-derived sulfides for supercapacitors and the current trends as electrocatalysts for water-splitting, more specifically for HER and OER are discussed. Finally, perspectives and possible insights into the future development of MOF-derived electrode materials toward a more sustainable society are anticipated.

1. Introduction

The development of sustainable and renewable energy sources is urgent and essential for addressing the growing concerns about the seriousness of the energy crisis and environmental pollution.[1] It is, therefore, crucial to find substitutes for fossil fuels and develop new efficient technologies for providing clean energy[2] to achieve a sustainable society.

The development of high-performance energy conversion and storage functional technologies is in high demand, mainly focusing on solar energy conversion devices (such as

Department of Fundamental Chemistry, Institute of Chemistry, University of São Paulo, Av. Prof. Lineu Prestes 748, São Paulo, SP, 05508-000, Brazil. E-mail: josuefisicoquimico@hotmail.com; luangnes@iq.usp.br

Matheus Ireno da Silva obtained a Bachelor's degree in Chemistry from the Federal Institute of Education, Science and Technology of São Paulo (IFSP), Brazil, in 2017. Currently, he is a Natural Sciences PhD student at the Institute of Chemistry at the University of São Paulo (IQ-USP) Brazil, with an emphasis on Nanotechnology and Supramolecular Chemistry. His research interests are focused on the synthesis, characterization, and application of self-assembled nanoparticles and nanocomposites, aiming at the improvement of their performances in sensors, electrocatalysis and photocatalysis, and energy storage, production and conversion by synergistic effects.
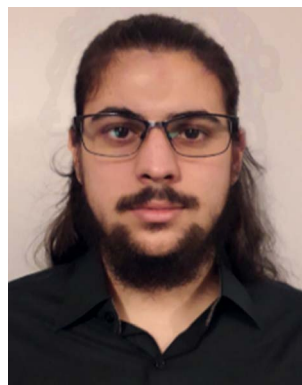
Ítalo Reis Machado obtained a Bachelor's degree in Chemistry at Mackenzie Presbyterian University (São Paulo, Brazil) in 2018. Currently, he is a Natural Sciences Master's degree student at the Institute of Chemistry at the University of São Paulo (IQ-USP) Brazil, with an emphasis on nanotechnology and supramolecular chemistry. His research interests are focused on the synthesis, characterization and application of catalysts for energy conversion based on supramolecular precursors.

photovoltaics and solar water-splitting cells) and electrochemical energy storage devices (especially supercapacitors and batteries).[1] However, in order to introduce these applications competitively into the market, great challenges need to be overcome,[3] especially in the development of robust and low-cost electrocatalytic materials to minimize the overpotential of the tetra-electronic and tetra-protonic reaction associated with the oxidation of water to dioxygen, and the design of high energy density electrode materials, especially at high-power densities.

Among the different materials studied, much attention has recently been given to materials derived from metal–organic frameworks (MOFs). These materials can "inherit" the main important properties of MOFs, such as high specific surface area, satisfactory porosity, tunable morphology, conductivity, electrochemical activity, stability, and multifunctionalities,[4] leaving aside the relatively low conductivity and lack of chemical/structural robustness of pristine MOFs, inheriting only the essential structural and compositional properties from

their MOF precursors.[5] MOFs are being used intensively as sacrificial templates and metal precursors, performing an important role in the design of hollow micro/nanostructured materials with extended internal voids and functional shells.[6]

A variety of MOF-derived materials have recently been reported for different applications, as highlighted in some review articles. For instance, Wang *et al.*[7] recently reported the application of MOF-derived mixed metal (Ni, Co, Mn) oxides in lithium-ion batteries (LIBs), supercapacitors (SCs), and lithium-ion capacitors (LICs), while Gonçalves and colleagues[8,9] summarized the recent advances in the use of MOF-derived materials, such as metals, metal oxides/hydroxides, metal sulfides, metal phosphides, carbon materials or their composites and their potential as electrode materials in electrochemical sensors. Still in the field of energy storage, Y. Li, J. Zhang and M. Chen[10] reviewed the progress on MOF-derived carbon and composites as advanced anode materials for potassium ion batteries (PIBs). Other reviews have comprehensively highlighted the perspectives of materials derived
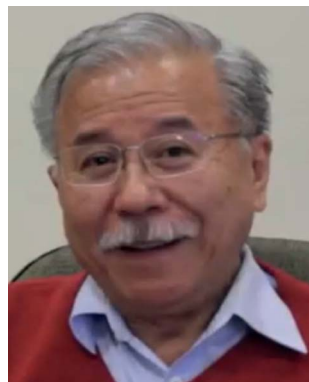
Henrique Eisi Toma holds a PhD in Chemistry and is a Professor at the University of São Paulo. He is a Guggenheim Fellow, a member of the Brazilian Academy of Sciences, TWAS, and Grã-Cruz of the National Science Order. His major interests are Inorganic, Bioinorganic, Supramolecular Chemistry, and Molecular Nanotechnology.

Lucio Angnes is a Full Professor at the Institute of Chemistry at the University of São Paulo. His research interests include the construction of electrodes with new and alternative materials, the development of modified electrodes, arrays of microelectrodes, the design of different procedures for enzyme immobilization (on electrodes or inside microchannels), and the association of the created devices with flowing systems (flow and batch injection analysis). He has authored 180 research papers, is a member of the Scientific Board of Biosensors & Bioelectronics, Electroanalysis, Journal of Pharmaceutical Research and Biosensors. He is also a member of the São Paulo State Academy of Science.

Koiti Araki is a Full Professor at the Institute of Chemistry at the University of São Paulo since 2006, a principal researcher in the Supramolecular Chemistry and Nanotechnology Lab, and a member of the Sao Paulo State Academy of Science. His research interests are focused on the design and preparation of functional hybrid nano-biomaterials and nanocomposites by coordinative supramolecular chemistry approaches that can help tackle the main challenges in energy, nanomedicine, and environment.

Josué Martins Gonçalves is a postdoctoral researcher in the group headed by Prof. Lucio Angnes at the University of São Paulo (USP), Brazil, and the recipient of a prestigious research fellowship from FAPESP. He graduated with a degree in Chemistry from the University Vale do Acaraú (UVA) in 2014 and received his PhD from USP in 2019, under the supervision of Prof. Koiti Araki. His current research interests include the applications of nanomaterials in sensors, electrocatalysis, energy conversion, and storage devices.

This journal is © The Royal Society of Chemistry 2022

J. Mater. Chem. A, 2022, **10**, 430–474 | **431**

from MOFs for supercapacitors.[4,5,11] For example, Chen et al.[12] reported the preparation methods, morphology, and performance of MOF-based derivatives in supercapacitors, while Ahmad et al.[11] reviewed the use of zeolitic imidazolate framework (ZIF)-derived porous carbon materials for the same purpose. Complementarily, Ye et al.[13] recently reported an overview on the progress in pristine MOFs, MOF composites, and their derivatives for next-generation rechargeable batteries including lithium–sulfur batteries, lithium–oxygen batteries, sodium-ion batteries, potassium-ion batteries, Zn-ion batteries, and Zn–air batteries.

There is considerable activity in the field of energy conversion, especially focusing on the oxidation and reduction processes involved in the water-splitting reaction. For example, X. Wen & Jingqi Guan[14] summarized the current developments on several transition metal MOFs and MOFs-derived electrocatalysts for the hydrogen evolution reaction (HER), whereas Q. Shao, J. Yang & X. Huang[15] reviewed the MOF-based catalysts for electrochemical oxygen evolution reaction (OER) applications, including MOF-derived catalysts based on structured carbon-based, metal-based and substrate-engineered strategies. Recently, Choudhary et al.[16] discussed the advantages of combining MOFs with conducting polymers (CP) to form MOF@CP hybrids, the current problems, and possible solutions on designing higher performance electrode materials for supercapacitor devices. The incorporation of redox-active species, which increases the number of exchanged electrons per metal ion, is the only way to increase the faradaic specific charge capacitance of materials. Accordingly, this strategy becomes much more interesting as the size of such a ligand decreases; sulfide is the smallest one and has unique electronic, bonding, and redox properties. It can be considered the analogue of the oxide ion in transition metal oxides but with electrochemically accessible sulfide/disulfide redox processes that can boost the specific charge/capacitance of materials made from, or hybrids incorporating them.

Numerous review articles have more recently reported the use of transition metal sulfides (TMSs) as promising materials for various applications, especially for energy conversion and storage[17–19] due to their low cost, fascinating redox reversibility, and electronic conductivity as compared to metal oxides.[20] The sulfur atom in the sulfide exhibits a lower electronegativity than oxygen, being one of the few small ligands amenable to fast reversible redox processes involving the formation of S–S bonds. This results in a flexible phase structure that can provide superior charge capacities while facilitating the transfer of electrons and improving the electrochemical performances,[20] providing a promising material for energy technologies. For instance, Sakuda et al.[21] demonstrated multielectron processes in metal sulfides; more specifically, mechanochemically processed Li_2TiS_3 and Li_3NbS_4 can provide specific capacities as high as 425 mA h g and 386 mA h g, respectively, indicating the transfer of 2.5 to 3.5 electrons. Gonçalves et al.[22] reviewed the recent progress in core@shell sulfide electrode materials for advanced supercapacitor devices. Y. Gao & L. Zhao reviewed the recent advances in nanostructured TMSs-based electrode materials for cathode materials of asymmetric

supercapacitors.[20] Zhang et al.[23] demonstrated the high potentiality of CoS_2 as a cathode material for Zn-ion batteries using nonaqueous electrolytes, given the efficient Zn^{2+} intercalation/deintercalation mediated by reversible $2S^{2-}/S_2^{2-}$ redox processes operating in a multivalent system, demonstrating interesting perspectives as materials for high-capacity batteries. Also, rGO/CoS_2 nanoparticle porous hybrids[24] showed favorable open structures for electrolyte diffusion and improved electrochemical performance, where cobalt sulfide is responsible for the enhanced specific capacitance, as well as rate capability and cycling stability, as expected for a promising electrode material for advanced energy storage devices.

Li and collaborators[25] summarized the interface engineering of transition metal sulfide–MoS_2 heterostructure composites as effective electrocatalysts for water-splitting. However, to the best of our knowledge, there is no report summarizing the recent progress on materials based on MOF-derived TMSs in a comprehensive way focusing on the possible effects associated with sulfide electrochemical properties. Therefore, in this review article, we focus on the recent advances in MOF-derived sulfides-based electrode materials for energy applications and the main strategies used for the design and activation of such porous materials (Scheme 1), especially for electrode materials of supercapacitors, and the current trends as electrocatalysts for water-splitting, more specifically for the HER and OER. Finally, the perspectives and possible future directions will be discussed.
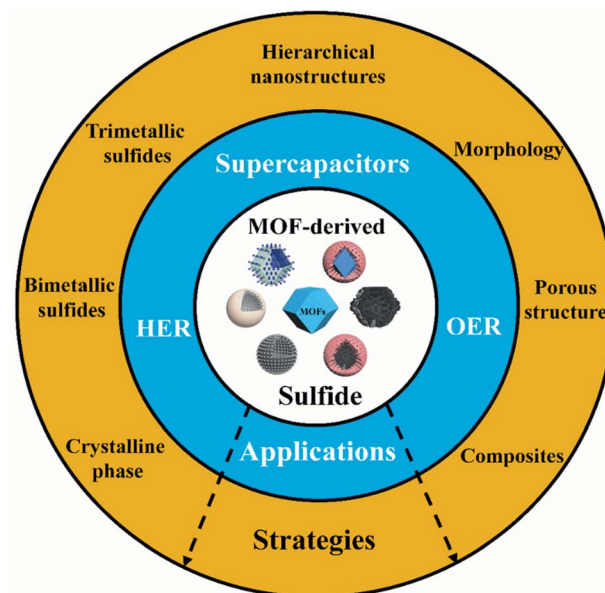
Scheme 1 Applications and strategies for the use and development of electrode materials based on MOF-derived sulfides. The MOF and MOF-derived structures in the center of the scheme were reproduced with permission from ref. 26–28. Adapted with permission.[26] Copyright© 2018 Wiley-VCH Verlag GmbH & Co. KGaA, Weinheim. Adapted with permission.[27] Copyright© 2015 Wiley-VCH Verlag GmbH & Co. KGaA, Weinheim. Adapted with permission.[28] Copyright Marketplace™, Royal Society of Chemistry.

432 | J. Mater. Chem. A, 2022, 10, 430–474

This journal is © The Royal Society of Chemistry 2022

Table 1 Comparison of the relevant electrochemical parameters of MOF-derived transition metal sulfide-based materials and their performance in supercapacitive energy storage devices assembled with a suitable cathode material[b]

Electrode material derivatives	Precursors	Method	Electro-chemical System	Specific capacitance or specific vapacity	Potential window (V): ref. electrode	Rate capability: current density range	Stability retention: cycle numbers	Highest energy density (W h kg⁻¹)	Highest power density (W kg⁻¹)	Negative electrode material in SC	Ref.
Mono-metallic											
CoS_2	ZIF-67	Calcination; sulfidation	Three-electrode	$375.2 C\ g^{-1}$ $(750.4\ F\ g^{-1})$ at $1\ A\ g^{-1}$	0.0 to 0.5 Hg/HgO	~70% 1 to 20	92.1% 10 000	52.1 at 401 W kg⁻¹	7871 at 37 W h kg⁻¹	AC	52
			SC	$146\ F\ g^{-1}$ at $0.5\ A\ g^{-1}$	0.0 to 1.6	71% 0.5 to 20	89% 5000				
CoS_2@CNTs	Co-MOF	Calcination; gas-sulfidation	Three-electrode	$825\ F\ g^{-1}$ at $0.5\ A\ g^{-1}$	0.0 to 0.4 SCE	32.5% 0.5 to 10	82.9% 5000	—	—	—	62
			SC	—							
CoS_x@MnO_2	ZIF-67 @MnO_2	Sulfidation	Three-electrode	$1720\ F\ g^{-1}$ at $0.5\ A\ g^{-1}$	0.0 to 0.5 Hg/HgO	71% 1 to 10	80% 5000	49.56 at 800 W kg⁻¹	8000 at 33.75 W h kg⁻¹	BAC	66
			SC	$145\ F\ g^{-1}$ at $1\ A\ g^{-1}$	0.0 to 1.6	—	92% 5000				
Co_3S_4/ MWCNT	ZIF-67/ MWCNT	Hydrothermal/sulfidation; calcination	Three-electrode	$850.3\ F\ g^{-1}$ at $2\ A\ g^{-1}$	0.0 to 0.45 SCE	81.9% 2 to 30	78.98% 5000	—	—	—	65
Co_3S_4@PPy	ZIF-67@PPy	Hydrothermal/sulfidation	Three-electrode	$1706\ F\ g^{-1}$ at $1\ A\ g^{-1}$	0.0 to 0.5 SCE	73.2% 1 to 10	68.1% 5000	50.5 at 849.1 W kg⁻¹	8516.1 at 22.0 W h kg⁻¹	AC	70
			SC	$125.9\ F\ g^{-1}$ at $1\ A\ g^{-1}$	0.0 to 1.7	/	82.8% 10 000				
Co_9S_8@ SNCC	S,N-containing Co-MOF	Calcination/ etching	Three-electrode	$429\ F\ g^{-1}$ at $1\ A\ g^{-1}$	−0.1 to 0.4 Hg/HgO	78.3% 1 to 20	98% 2000	—	—	—	72
NiCo-LDH/ Co_9S_8/CC	Co-MOF/CC	Ion-exchange/ etching; hydrothermal; sulfidation	Three-electrode	$2850\ F\ g^{-1}$ at $1\ A\ g^{-1}$	0.0 to 0.4 Ag/AgCl	72.4% 1 to 10	92.6% 5000	38.0 W kg⁻¹	8000 W h kg⁻¹	AC	53
			SC	$106\ F\ g^{-1}$ at $1\ A\ g^{-1}$	0.0 to 1.6	82.5% 1 to 10	93.1% 5000				
C/NiCo-LDH/Co_9S_8	ZIF-67-C	Hydrothermal; sulfidation	Three-electrode	$1653\ F\ g^{-1}$ at $4\ A\ g^{-1}$	0.0 to 0.5 SCE	62% 4 to 20	95.4%3000	39.0 at 2400 W kg⁻¹	7400 at 30.1 W h kg⁻¹	CNT	6
			SC	$194\ F\ g^{-1}$ at $4\ A\ g^{-1}$	/	77.8% 4 to 12	90.9% 10 000				
CF@Ni CoZn-LDH/Co_9S_8-QD	2D Zn-MOF	Co-precipitation/ etching; hydrothermal	Three-electrode	$2504\ F\ g^{-1}$ at $1\ A\ g^{-1}$	0.0 to 0.5 Hg/HgO	62% 1 to 20	—	56.4 at 875 W kg⁻¹	8200 at 42 W h kg⁻¹	CNS-SCN	67
			SC	$132.6\ F\ g^{-1}$ at $1\ A\ g^{-1}$	0.0 to 1.75	80.2% 1 to 10	95.3% 8000				
α-NiS/rGO	Ni-MOF-74/rGO	Gas-sulfidation; calcination	Three-electrode	$744\ C\ g^{-1}$ at $1\ A\ g^{-1}$	0.0 to 0.5 Ag/AgCl	80.6% 1 to 50	89% 20 000	93.0 at 962 W kg⁻¹	4634 at 54.0 W h kg⁻¹	C/NG-A	74
			SC	—	0.0 to 1.6	58% 1 to 50	93% 10 000				
NiS_2@C	Ni-MOF	Calcination/ sulfidation	Three-electrode	$833\ F\ g^{-1}$ at $0.5\ A\ g^{-1}$	0.0 to 0.4 SCE	55.8% 0.5 to 10	81.6% 5000	—	—	—	61
			SC	—	—	—	—				

This journal is © The Royal Society of Chemistry 2022

J. Mater. Chem. A, 2022, **10**, 430–474 | **433**

Table 1 (*Contd.*)

Electrode material derivatives	Precursors	Method	Electrochemical System	Specific capacitance or specific capacity	Potential window (V): ref. electrode	Rate capability; current density range	Stability retention: cycle numbers	Highest energy density (W h kg⁻¹)	Highest power density (W kg⁻¹)	Negative electrode material in SC	Ref.
NiS₂/ZnS	Ni/Zn-BDC MOF	Hydrothermal/sulfidation	Three-electrode / SC	1198 F g⁻¹ at 1 A g⁻¹ / 89.7 F g⁻¹ at 1 A g⁻¹	0.0 to 0.45 SCE / 0.0 to 1.6	49.4% 1 to 10 / 69.1% 1 to 10	~87% 1000 / 88.7% 1500	28.0 at 478.9 W kg⁻¹	7509.7 at 19.4 W h kg⁻¹	AC	71
Ni-Ni₃S₄@NC/CNTs SC	Ni-MOF/CNTs	Calcination; hydrothermal/sulfidation	Three-electrode / 64	1490 F g⁻¹ at 1 A g⁻¹ / 127.5 F g⁻¹ at 1 A g⁻¹	0.0 to 0.5 SCE / 0.0 to 1.5	53.7% 1 to 10	84.5% 3000	—	39.8 at 749.8 W kg⁻¹	—	CNT
CuS/CNTs	CNTs@HKUST-1	Hydrothermal/sulfidation	Three-electrode / SC	606.7 F g⁻¹ at 1 A g⁻¹ / 126.2 F g⁻¹ at 2 A g⁻¹	0.0 to 0.5 Hg/HgO / 0.0 to 1.5	44.5% 1 to 10 / 42.5% 2 to 10	—	38.4 at 750 W kg⁻¹	~7600 at ~19.0 W h kg⁻¹	CNC	69
SC Cu₉S₈@C@PPy/CC	HKUST-1	Two-step electrodeposition	Three-electrode	270.72 F g⁻¹ at 10 mV s⁻¹	−0.4 to 0.5 SCE	44.7% 10 to 100	80.4, 3000	—	—	—	58
Bi-metallic Zn-Co-S/NF	ZIF-Co₅₀% Zn₅₀%	Solvothermal	Three-electrode / SC	1646 F g⁻¹ at 1 A g⁻¹ / 126.2 F g⁻¹ at 2 A g⁻¹	−0.1 to 0.3 SCE / 0.0 to 1.5	89.5% 1 to 15 / 42.5% 2 to 10	90% 500 / 89% 2000	39.41 at 1493 W kg⁻¹	7080 at 17.7 W h kg⁻¹	AC	59
Zn₀.₇₆Co₀.₂₄S-NC/CC	Zn₀.₇₆Co₀.₂₄-MOF/CC	Hydrothermal; sulfidation	Three-electrode / SC	2133.2 F g⁻¹ at 1.25 A g⁻¹ / 290 F g⁻¹ at 1 A g⁻¹	0.0 to 0.6 Ag/AgCl / 0.0 to 1.6	76.4% 1.25 to 20 / 72.3% 1 to 16	95.63% 10 000 / 91.82% 5000	92.59 at 846.2 W kg⁻¹	9517.98 at 65.73 W h kg⁻¹	MPC	55
ZnₓCo₁₋ₓS@Ni(OH)₂/CC	Zn/Co-MOF/CC	Calcination; hydrothermal/sulfidation; electrodeposition	Three-electrode / SC	2730 F g⁻¹ at 3 mA cm⁻² / 210.7 F g⁻¹ at 0.5 A g⁻¹	0.0 to 0.45 SCE / 0.0 to 1.6	76.6% 3 to 20 / 57.8% 0.5 to 10	87% 10 000 / 82% 10 000	75 at 400 W kg⁻¹	8000 at 40.1 W h kg⁻¹	ZnₓCo₁₋ₓS@VN/CC	75
Co₃S₄@FeCo₂S₄/NF	Co-MOF/NF	Ion-exchange/etching; sulfidation	Three-electrode / SC	2695 F g⁻¹ at 1 A g⁻¹ / 131 F g⁻¹ at 1 A g⁻¹	0.0 to 0.4 SCE / 0.0 to 1.6	69.8% 1 to 10 / 61.8% 1 to 10	84% 1000 / 89.6% 5000	43.6 at 770 W kg⁻¹	5510 at 13.3 W h kg⁻¹	NF/rGO	57
NiCo₂S₄/ACC	Co-MOF/ACC	Ion-exchange/etching; hydrothermal/sulfidation	Three-electrode / SC	2392 F g⁻¹ at 1 A g⁻¹ / 83.2 F g⁻¹ at 1 A g⁻¹	0.0 to 0.5 Hg/HgO / 0.0 to 1.6	80.3% 1 to 20 / 57.1% 1 to 10	85.1% 10 000 / 82% 10 000	30.1 at 800.2 W kg⁻¹	7800 at 16.89 W h kg⁻¹	AC/ACC	60
NiCo₂S₄@CC	CC@ZIF-67	Ion-exchange; calcination; hydrothermal/sulfidation	Three-electrode / SC	879.6 F g⁻¹ at 1 A g⁻¹ / 120 F g⁻¹ at 3 A g⁻¹	0.0 to 0.7 Hg/HgO / 0.0 to 1.5	88.7% 1 to 20 / 72.5% 3 to 15	~100% 1000 / 98.39% 10 000	37.5 at 2250 W kg⁻¹	11250 at 27.19 W h kg⁻¹	NC@CC	73
CF@NiCoZnS/NiCo₂S₄	CF@Zn-MOF	Hydrothermal; hydrothermal/sulfidation	Three-electrode	194 mA h g⁻¹, 1396.8 F g⁻¹ at 1 A g⁻¹	0.0 to 0.5 Hg/HgO	74.2% 1 to 20	/	48.7 at 800 W kg⁻¹	8000 at 32.3 W h kg⁻¹	CNS-CNT	76

434 | *J. Mater. Chem. A*, 2022, **10**, 430–474

This journal is © The Royal Society of Chemistry 2022

Review

Table 1 (Contd.)

Electrode material derivatives	Precursors	Method	Electro-chemical System	Specific capacitance or specific vapacity	Potential window (V): ref. electrode	Rate capability; current density range	Stability retention: cycle numbers	Highest energy density (W h kg^{-1})	Highest power density (W kg^{-1})	Negative electrode material in SC	Ref.
NiCo-alloy @(NiCo)$_9$S$_8$/ CF	Co-MOF/CF	Solvothermal; ion-exchange; reducing atmosphere; sulfidation	SC	137 F g^{-1} at 1 A g^{-1}	0.0 to 1.6	66.1% 1 to 10	70.1% 10 000	48.2 at 840 W kg^{-1}	8300 at 32.3 W h kg^{-1}	Fe$_x$O$_y$@ CNS	54
			Three-electrode	213 mA h g^{-1}, 1533.6 F g^{-1} at 1 A g^{-1}	0.0 to 0.5 Hg/HgO	80.3% 1 to 20	86% 5000				
			SC	16.8 mA h g^{-1} at 1 A g^{-1}	0.0 to 1.7	67% 1 to 10	83.5% 5000				
Ni-Co-S@NC	NiCo-BTC-MOF	Calcination; hydrothermal/ sulfidation	Three-electrode	543.9C g^{-1a}, 988.9 F g^{-1} at 1 A g^{-1}	0.0 to 0.55 Hg/HgO	67.3% 1 to 20	~100% 2000	39.6 at 808 W kg^{-1}	7910 at 27.1 W h kg^{-1}	AC	63
			SC	111.2 F g^{-1} at 1 A g^{-1}	0.0 to 1.6	68.5% 1 to 10	81.5% 3000				
CoNi$_2$S$_4$	ZIF-67	Co-precipitation/ etching; sulfidation	Three-electrode	1890 F g^{-1} at 4 A g^{-1}	0.0 to 0.45 Ag/AgCl	81.2% 4 to 20	71.6% 5000	35 at 640 W kg^{-1}	5760 at 18 W h kg^{-1}	YS-CS	77
			SC	98 F g^{-1} at 1 A g^{-1}	0.0 to 1.6		63.2% 5000				
CoNi$_2$S$_4$	ZIF-67	Sulfidation; ion-exchange	Three-electrode	1382 F g^{-1} at 4 A g^{-1}	0.0 to 0.45 Ag/AgCl	83.6% 1 to 10	70% 10 000	35.3 at 750 W kg^{-1}	3784 at 23.4 W h kg^{-1}	AC	79
			SC	113 F g^{-1} at 1 A g^{-1}	0.0 to 1.6	66.4% 1 to 5	79% 10 000				
CNWAs @Ni@ CoNi$_2$S$_4$/CC	Co-MOF/NF	Calcination; two-step electro-deposition	Three-electrode	3163 F g^{-1} at 1 A g^{-1}	0.0 to 0.5 Ag/AgCl	47.5% 1 to 40	95.5% 10 000	53.8 at 801 W kg^{-1}	8000 at 32.2 W h kg^{-1}	AC	56
			SC	151.3 F g^{-1} at 1 A g^{-1}	0.0 to 1.6	48% 1 to 30	90.1% 10 000				
Sn$_x$Ni$_{3-x}$S$_2$	Ni/Sn-MOF	Two-step hydrothermal	Three-electrode	1667 F g^{-1} at 1 A g^{-1}	0.0 to 0.45 SCE	66.2% 1 to 10	81.8% 5000	29.13 at 700 W kg^{-1}	—	AC	78
			SC	107 F g^{-1} at 1 A g^{-1}	0.0 to 1.4	57.9% 1 to 10	82.7% 5000				
Tri-metallic											
Ni-Zn-Co-S/NF	Zn-Co-ZIF/NF	Hydrothermal/ sulfidation	Three-electrode	358.1 mA h g^{-1}; 2.343.9 F g^{-1a} at 10 mA cm^{-2}	0.0 to 0.55 Hg/HgO	64.9% 10 to 100	85% 1000	91.7 at 458 W kg^{-1}	6696 at 66.9 W h kg^{-1}	Bi$_2$O$_3$/NF	68
			SC	114.7 mA h g^{-1} at 3 mA cm^{-2}	0.0 to 1.6	75% 3 to 60	88% 1000				
CF@NiCoZn-S/NiCo$_2$S$_4$	CF@ Zn-MOF	Hydrothermal; hydrothermal/ sulfidation	Three-electrode	194 mA h g^{-1}, 1396 F g^{-1a} at 1 A g^{-1}	0.0 to 0.5 Hg/HgO	74.2% 1 to 20	—	48.7 at 800 W kg^{-1}	8000 at 32.3 W h kg^{-1}	CNS-CNT	76
			SC	137 F g^{-1} at 1 A g^{-1}	0.0 to 1.6	66.1% 1 to 10	70.1% 10 000				

[a] Calculated by the authors. [b] SC = supercapacitor device; NF = nickel foam; CNT = carbon nanotubes; CNC = nitrogen-doped carbon polyhedrons interspersed into carbon nanotube films; NC = nitrogen-doped carbon; CC = carbon cloth; MPC = MOF-derived mesoporous carbon; C/NG-A = Co-modified N-doped graphene aerogel; CNWA = carbon nanowall arrays; PPy = polypyrrole; CF = carbon fibers; CNS = carbon nanosheets; MWCNT = multiwalled carbon nanotube; BAC = bioderived active carbon; LDH = layered double hydroxide; QD = quantum dots; SCN = single-walled carbon nanotubes; SNCC = S,N-containing carbon cuboid; YS-CS = yolk-shell carbon spheres.

This journal is © The Royal Society of Chemistry 2022

J. Mater. Chem. A, 2022, 10, 430–474 | 435

2. Synthesis protocols of MOF-derived sulfides

First defined by Yaghi's and Li's groups in the 1990s, MOFs, are a class of hybrid networks of supramolecular porous coordination polymers that are assembled by metal ions/clusters and organic linkers through coordination bonds and, thus, possess highly adjustable three-dimensional structures and controllable composition, as well as serve as sacrificial templates for the synthesis of derived materials with highly optimized morphologies.[29–31] MOF materials are usually formed by the coordinative self-assembly of metal ion connective species with bridging ligands, generally organic, generating a porous cyclic frame through co-precipitation, solvothermal, mechanochemical, liquid phase diffusion, microwave-assisted, electrochemical, sonochemical, or layering methods.[29,30] Alternative synthetic routes can lead to different crystallization rates, particle sizes, size distributions, and adsorption properties, as well as morphologies, which directly influence the properties of the resultant MOF material and derived materials.[29–31] Compared with other methods, the solvothermal method has the advantage of being time-saving and forming MOFs with regular morphology and high purity, thus being the most commonly used synthesis method.[31–33] It is worth noting that due to the numerous possible metal ions and organic ligands available for the preparation of MOFs, more than 20 000 have been prepared[32] and classified and some of the main types of MOFs are those based on the following. (a) Imidazoles as ligands, giving zeolite-like structures (ZIF), (b) benzenecarboxylates (HKUST), (c) those that are the result of polymorphism in MOFs (MIL), and those based on different metallic elements such as (d) alkaline earth (AEPF) and (e) rare earth metal ions (RPF).[33]

Given the high variability and feasibility of MOFs structures and compositions, materials with different specific surface areas and porosities, adsorption properties, electrochemical and catalytic performances, chemical and functional behaviors, *etc.*, can be achieved. Thus, the MOF properties can be adjusted for a wide range of electrochemical processes such as the oxygen reduction reaction (ORR), oxygen evolution reaction (OER), hydrogen evolution reaction (HER), and carbon dioxide reduction; they may also find applications as electrode materials in devices such as fuel cells, batteries, and supercapacitors.[29,31] Their unique porous structures made of metal ions and organic connectors resembling Prussian Blue-like materials invite us to
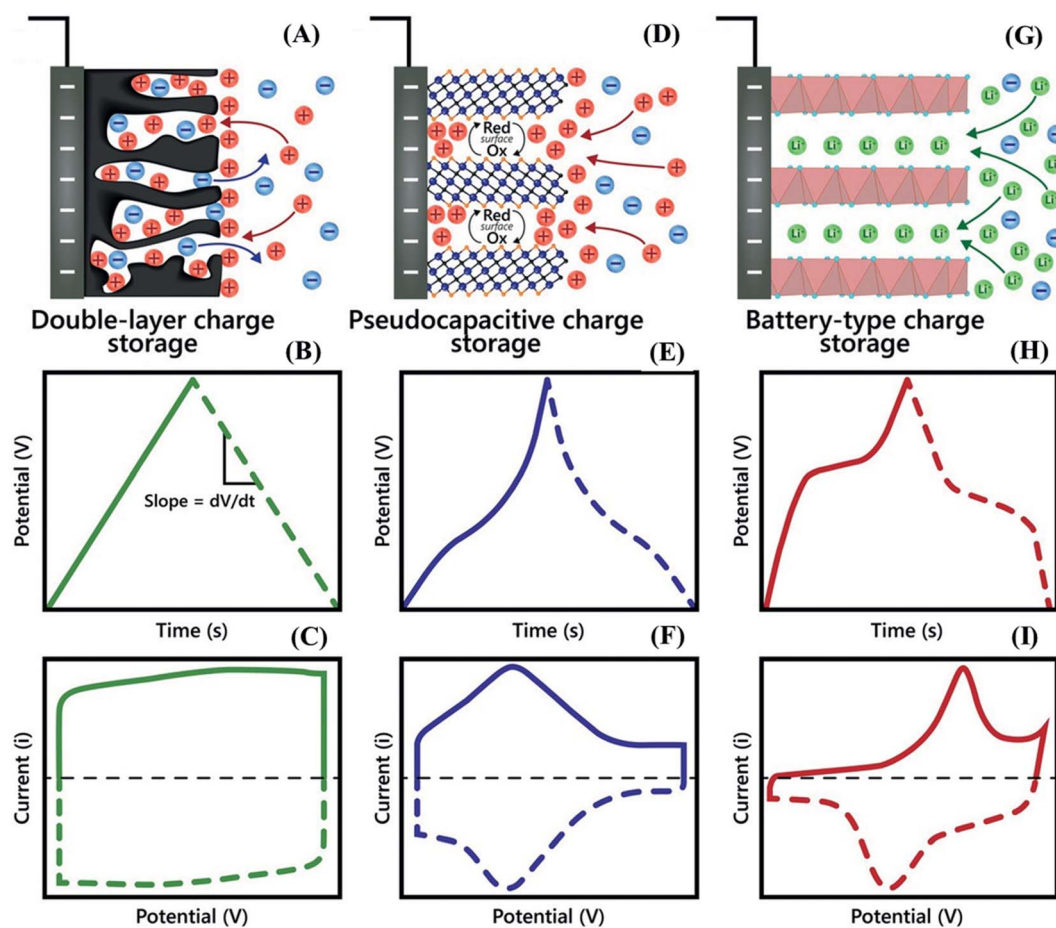

Fig. 1 A schematic illustration of the energy storage mechanisms with the corresponding electrochemical signatures (representative shapes of CV and GCD curves) of (A–C) electrical double layer capacitance, (D–F) pseudocapacitance, and (G–I) faradaic battery-type devices. Adapted with permission.[45] Copyright© 2019 Wiley-VCH Verlag GmbH & Co. KGaA, Weinheim.

436 | *J. Mater. Chem. A*, 2022, **10**, 430–474

This journal is © The Royal Society of Chemistry 2022

explore their possible faradaic and capacitive properties in energy storage and conversion devices. Nevertheless, the electronic and hopping charge-diffusion is not as efficient as expected, generally exhibiting intrinsically poor electrical conductivity, as well as structural instability. Accordingly, strategies to improve these properties while increasing the electrochemical properties were sought, leading to MOF-derived materials. These are materials obtained by chemothermal treatment (*e.g.* sulfidation) of MOFs, which were shown to be extremely beneficial since they mostly retain their three-dimensional structure and morphology while generating porous carbon materials doped with transition metal oxides, hydroxides, and sulfide nanoclusters, and carbon–metal nanocomposites, to deliver electrochemical performances comparable to other electrode materials.[33,34]

MOF-derived transition metal sulfides and their respective nanocomposites, as summarized in Tables 1, 2, and 3, can be prepared by the following: (i) calcination or solvothermal and subsequent sulfidation, in which metal oxides/hydroxides are initially produced and then sulfurized; (ii) one-step calcination in the presence of sulfur vapor; (iii) solvothermal sulfidation; (iv) electrochemical conversion; (v) acidic etching. Although each has been demonstrated to be a suitable approach, the sulfidation of MOF-derived metal oxides/hydroxides and the one-step sulfidation of MOFs by calcination and solvothermal methods are the most common ones, especially using ZIFs and HKUSTs structures as precursors. Interestingly, such sacrificial MOF templates can be easily prepared on highly conductive substrates to produce binder-free electrode materials. ZIFs, HKUSTs, and similar MOFs have been demonstrated to be desirable precursors with well-defined porous/hollow morphologies that can enhance the electrochemical properties of the resultant MOF-derived transition metal sulfide-based electrode materials, as comprehensively discussed in this review.

3. Background in water–splitting and supercapacitor systems

3.1. Supercapacitors: electrochemical signatures

One of the main differences between supercapacitors and batteries is that the former generally possess high-power density and they can be charged/discharged in very short periods of time, thus providing bursts of energy when needed.[35] In this sense, to generate solutions to the challenges of modern society, supercapacitor devices have been intensively studied by the scientific community, especially in the design of high-performance supercapacitor materials and devices, which can be divided into two categories, electrical double-layer capacitors (EDLC) and pseudocapacitors, according to the electrode material type and charge/discharge mechanism.[36]

The EDLCs are characterized by high-power densities ($\sim$15 kW kg^{-1}) but have low energy densities (5–10 W h kg^{-1}) that restrict their applications in energy storage.[35] The charges are stored electrostatically at the electrode/electrolyte interface (a non-faradaic process, Fig. 1A), and the main electrochemical

signature of assembled devices is a potential independent of the surface density of charges,[35,37] characterized by rectangular box-shaped cyclic voltammograms (CVs) (Fig. 1C), and galvanostatic charge/discharge (GCD) profiles with symmetric triangular-shaped patterns (Fig. 1B).

In contrast to EDLCs, pseudocapacitor materials can provide both high energy and high power, which are ideal characteristics for most applications, especially in mobile devices. This intermediate performance between EDLCs and batteries is consistent with capacitive and faradaic processes taking place at the electrode material surface (Fig. 1D). Pseudocapacitive electrodes exhibit ultrafast redox reactions approaching the charge/discharge kinetics of a capacitor, giving rise to an electrochemical signature characterized by a CV profile similar to that of adsorbed redox species generally described as quasi-rectangular CVs (Fig. 1F) and quasi-triangular GCD curves (Fig. 1E).[35,37] This condition is achieved when the properties of accessible electrochemically active sites change as a function of the redox state of nanostructured materials with suitable electrical conductivity and ion diffusion properties. The most well-known pseudocapacitors are based on ruthenium oxides (RuO_2) and manganese oxides (MnO_2); however, this list has recently been expanded to include other oxides, as well as nitrides and carbides.[38]

On the other hand, the electrolyte diffusion-controlled processes and phase change associated with the electrode materials during the charge–discharge process make the electrochemical signature of battery-type electrode materials quite different from that of supercapacitor materials. As a consequence, the potential of the battery-type electrode remains constant, characterized by a couple of well-defined redox peaks in the CV (Fig. 1I) profiles and a plateau in the charge/discharge profiles (Fig. 1H).[37] Some typical examples of battery-type materials include metal oxides,[3,39] hydroxides,[40–42] sulfides,[22] selenides,[43] and phosphides[44] based on Ni, Co, and Cd.

At this point, it is important to mention that many researchers still mistakenly refer to battery-type materials as pseudocapacitors simply because they exhibit fast charge/discharge features, although several review articles have been published and explain the main differences, as mentioned above. In addition, special attention should be given when calculating the energy stored in the different types of materials since the charge storage mechanisms are completely different. For example, the energy stored in battery-type electrode materials is due to relatively complex faradaic processes and should be calculated from the CV and GCD profiles and expressed as specific capacity (mA h g^{-1}) or specific charge (C g^{-1}), whereas the correct unit for supercapacitive materials is F g^{-1} since there is more simple physical adsorption of ions at the interface, which is directly proportional to the surface area of the electrode, giving rise to capacitance.

3.2. Water-splitting

The accelerated population growth and the incessant search for a better quality of life imply a surge of energy demands, leading to the massive consumption of nonrenewable energy sources

This journal is © The Royal Society of Chemistry 2022

J. Mater. Chem. A, 2022, **10**, 430–474 | **437**

and environmental pollution at a speed never seen before. Therefore, the development of clean and renewable alternative energy sources is heavily demanded. Among the possibilities, the conversion of renewable energy into a high-energy chemical is one of the most promising ways for clean energy storage, where the electro- and photochemical water-splitting into H_2 and O_2 stands out among the most auspicious alternatives since the chemical energy stored in these gaseous small molecules

Fig. 2 (A) Scheme of a typical water electrolysis system. (B) Water-splitting semi-reaction under acidic and alkaline conditions. Schematic representation of the mechanism of the hydrogen evolution reaction under (C) acidic and (D) alkaline conditions, where M stands for the active sites on the electrode surface. (E) The adsorbate evolution mechanism (AEM) of OER processes in acidic (blue lines) and alkaline (orange lines) electrolytes. The purple lines denote the reaction of MOOH intermediates to generate oxygen, and the green lines the reaction of two M–O intermediates to produce an oxygen molecule. Here, M stands for the active sites on the electrode surface. (F) The elementary steps of the AEM mechanism under acidic and alkaline conditions. Adapted with permission.[47] Copyright© 2020 Wiley-VCH GmbH.

438 | J. Mater. Chem. A, 2022, 10, 430–474

This journal is © The Royal Society of Chemistry 2022

can be subsequently recovered in fuel cells or internal combustion engines while regenerating water in a cyclic way. There is a need for efficient and reliable hydrogen and oxygen production systems, especially considering that H_2 has the highest gravimetric energy density among all chemical fuels (142 MJ kg^{-1}), whereas O_2 is the most widely used and naturally occurring oxidizing agent.[46]

In essence, the water-splitting reaction ($H_2O \rightarrow H_2 + \frac{1}{2}O_2$) can be divided into two half-reactions, the hydrogen evolution reaction (HER) and the oxygen evolution reaction (OER), taking place concomitantly at the cathode and the anode, respectively (Fig. 2A).[36] Additionally, as shown in Fig. 2B, both reactions involve protons and consequently, these electrochemical reactions and associated potentials are dependent on the pH and diffusion of ions in acidic and alkaline conditions. Thus, the water-splitting processes are intrinsically limited, especially owing to the multielectronic and multiprotonic nature and consequent slow kinetics of the OER process. Accordingly, developing efficient electro- and photocatalysts for the HER and OER is fundamental for improving the energy conversion efficiency and reliability of clean and renewable energy technologies and improving their competitiveness.[46]

The HER is a representative of two-electron transfer reactions involving the adsorption and desorption of intermediates,[47] as shown in Fig. 2C and D. Its mechanism can be divided into two steps, where the first elemental step always is the Volmer semi-reaction or, in other words, the reduction of a proton by an electron generating a hydrogen atom (H*) adsorbed on the electrode material surface (M), and the second elementary step can be either the Tafel or the Heyrovsky semi-reactions, or both simultaneously.[46] The complete reaction mechanism in acidic and alkaline media are shown in Fig. 2C and D, respectively. The determination of which step is the possible rate-controlling step is indicated by the Tafel slope value of the HER polarization curve. The Tafel slope values under standard conditions are 118, 39, and 29.5 mV dec^{-1} for the Volmer, Heyrovsky, and Tafel reactions, respectively, implying that the Volmer step is always the rate-determining step, independent of the subsequent reaction pathway. Accordingly, the development of an electrocatalyst with an appropriate adsorption strength can decrease the activation energy and maximize the reaction kinetics.[46] As for the oxygen evolution reaction, despite the thermodynamic potentials shown in Fig. 2B, a much larger potential is always required in the actual electrolysis of water due to its complex multielectronic and multiprotonic mechanism (Fig. 2E and F), which is strongly dependent on the solution pH thus being entirely different under acidic and alkaline conditions. The production of O_2 requires the transfer of a total of four electrons, which occurs through multiple pH-dependent monoelectronic elementary steps that are expected to require large amounts of activation energy, responsible for the sluggishness and large overpotentials to overcome the kinetic barrier. Similar to the HER, the optimal OER catalytic activity can be achieved by tuning the binding energies of the semi-reaction intermediates. Accordingly, if the catalytic sites on the surface bind the intermediates too strongly, the reaction becomes sluggish due to the low reversibility, whereas too weak binding energies will not sufficiently activate the intermediate species to improve their kinetics. Thus, the design of OER catalysts profoundly relies on the fine-tuning of the adsorption energies of the oxygen intermediate species on the electroactive sites while maximizing other relevant parameters. The electrodes for the OER and HER should be made not only with materials with high density of electrocatalytic active sites but also with enhanced surface area, good electrical conductivity and fast ion-diffusion rates. Interestingly enough, all those requirements can be met by MOF-derived transition metal sulfides making them one of the most promising electrode materials.

A more in-depth comprehension of the HER and OER reactions and the electrocatalyst performances is dependent on the interpretation of the experimental results and parameters such as the onset potential, overpotential (η), Tafel slope (b), and exchange current density (j_0).[46,48] The oxidation and reduction processes involved in the water-splitting reaction need an additional potential to the thermodynamic potential, denoted overpotential (η), to overcome the kinetic barrier and promote the production of O_2 and H_2 at a suitable rate. The potentials are dependent on the local pH where the overpotential can be as large as several hundreds of millivolts to reach a certain current density, typically $j = 10$ mA cm^{-2}, as shown in the LSV depicted in Fig. 3A. Thus, the overpotential of a generic reaction (eqn (1)), under a given experimental condition, is the difference between the applied potential E and the standard potential E^0 (eqn (2)), or E_{eq} (eqn (3)), and can be easily evaluated using the Nernst equation (eqn (3)), where E_{eq} is the thermodynamic potential under any condition except the standard one. Thus, electrode materials exhibiting lower overpotentials for the HER or OER present larger electrocatalytic activity.

$$O + ne^- \rightleftarrows R \tag{1}$$
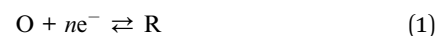
$$\eta = E - E^0 \tag{2}$$

$$E_{eq} = E^0 + \frac{RT}{nF}\ln\frac{C_O}{C_R} \tag{3}$$

In a typical LSV experiment, the measured current (i) corresponds to the sum of the cathodic and anodic currents (eqn (4)) and is dependent on the relative concentrations of oxidized and reduced species in equilibrium on the working electrode-solution interface. Consequently, i_0 depends on both the reduction (eqn (5)) and oxidation (eqn (6)) reactions, as expressed by the Butler–Volmer equation (eqn (7)), as illustrated in Fig. 3B. At zero overpotential the sum of both currents is null, as they have the same magnitude but opposite signals. The current at zero overpotential, named the exchange current (i_0), carries information about the electrocatalyst-substrate charge-transfer processes. Notwithstanding, at positive or negative enough potentials, only the oxidation current (i_a), or reduction (i_c) current, has a relevant contribution to the total current (i). Accordingly, the Butler–Volmer expression at, for example, positive enough potentials can be simplified as the Tafel equation (eqn (8)), which considers only the anodic current. Similar reasoning can be applied at negative enough potentials and the cathodic current. This equation can be rewritten as the

Fig. 3 (A) i–E curves for a water-splitting reaction. Reproduced with permission.[49] CC BY 4.0. (B) Current density plot, j (solid line) and extrapolations of the anodic current density j_a (upper dashed line) and cathodic current density j_c (lower dashed line) as a function of the overpotential η, according to the Butler–Volmer equation, with $\alpha_c = 0.5$. Reproduced with permission.[50] Copyright© 2014 IUPAC & De Gruyter Berlin Boston. (C) A plot of the overpotential η as a function of the natural logarithm of the anodic and cathodic current densities according to the Butler–Volmer equation, with $\alpha_c = 0.5$. Reproduced with permission.[50] Copyright© 2014 IUPAC & De Gruyter Berlin Boston. (D) A plot of η vs. log i showing a change in the Tafel slope as a function of current for the same electrocatalyst. Reproduced with permission.[51] Marketplace™, Royal Society of Chemistry. Panel (A–D) adapted with permission.[48] Marketplace™, Royal Society of Chemistry.

overpotential as a function of the logarithm of the current (eqn (9)), allowing the determination of the exchange current density (j_0) and the Tafel slope (b) (Fig. 3C). This last parameter provides essential information about the electrocatalytic activity of electrode materials, indicating how fast the current increases as a function of the overpotential. This means that a proportionally larger overpotential is needed to reach the appointed current density as the b values increase, thus indicating lower electrocatalytic efficiency, while lower b values indicate larger electrocatalytic activity. Additionally, since it is related to the rate-determining step of the corresponding heterogeneous electron-transfer reaction mechanism, the Tafel slope also provides relevant information about that key step in a multi-step mechanism. For instance, as the overpotential increases, a change in the reaction mechanism can take place, switching the reaction to a more electrocatalytic active mode, as shown in Fig. 3D.

$$i = i_a + i_c \tag{4}$$

$$i_C = nFk_c[C_O]\exp\left(-\frac{\alpha_c nFE}{RT}\right) \tag{5}$$

$$i_a = nFk_a[C_R]\exp\left(\frac{\alpha_a nFE}{RT}\right) \tag{6}$$

$$i = i_0\left[\exp\left(\frac{\alpha_a nFE}{RT}\right) + \exp\left(\frac{\alpha_c nFE}{RT}\right)\right] \tag{7}$$

$$i = i_0\left[\exp\left(\frac{\alpha_a nFE}{RT}\right)\right] \tag{8}$$

$$b = \frac{\eta}{\log\left(\dfrac{i}{i_0}\right)} = \frac{2.303RT}{\alpha F} \tag{9}$$

4. MOF-derived sulfide-based materials for supercapacitors

Transition metal oxides electrode materials have been widely studied over the past years as supercapacitive materials, especially those based on Co_3O_4, by tuning their properties by

440 | *J. Mater. Chem. A*, 2022, **10**, 430–474

This journal is © The Royal Society of Chemistry 2022

morphology control and doping methods. These approaches can result in quite positive changes, to surpass many of the downsides, since the changes in morphology can provide a larger surface area, thus activating larger percentages of redox sites, while doping with other transition metal ions can provide additional electrochemically active sites, or nanostructuring properties increasing the capacitance. Nevertheless, the substitution of oxygen atoms by sulfur atoms can even further enhance their electrochemical properties and potential applications since sulfide is a softer and more electrochemically accessible ligand than oxide, which can boost the specific capacitance of the resultant electrode material while increasing the electrical conductivity. Transition metal sulfides (TMSs) are among the most promising cathode materials for supercapacitor devices, even more than their corresponding oxide and hydroxide counterparts. For example, they exhibit fascinating properties including high theoretical charge capacity, redox reversibility, and improved intrinsic conductivity,[6,52–78] especially those based on mixed TMSs, such as bimetallic M_x-$Co_{1−x}S$ and $M_xCo_{3−x}S_4$, or even trimetallic M–N–Co–S (*e.g.* M and N = Zn, Ni), which present richer redox activity, superior stability, higher charge/electron transfer rates, more controllable structural features and lower band-gap energy owing to synergistic effects provided by the different active sites with multiple oxidation states. Additionally, the substitution of oxygen by sulfur generates more flexible systems given its lower electronegativity, which reduces the volume variation during charge/discharge processes leading to more stable structures. In addition, the narrower band-gap increases the conductivity and allows faster electron transport along the material.[52–55]

Even though the intrinsic electrochemical properties of a given TMS can vary depending on the microenvironment of the metallic center, the possible faradaic reactions can be quite similar despite their composition. Considering the possible reaction mechanisms, first of all, there is evidence that TMSs (M = mono-, bi- and trimetallic sulfides composed of Co, Fe, Zn, Ni, Cu, and/or Mn) react with $OH^−$ ions while transferring electrons to produce metal sulfides/hydroxides (eqn (10)), which then can react further to produce metal sulfides/oxides releasing additional electrons (eqn (11)).[6,52–78] For example, Huang *et al.*[68] proposed that the Co_9S_8 sites of the Ni–Zn–Co–S electrode material react with 9 $OH^−$ ions to produce 9 electrons and $Co_9S_8(OH)_9$, which can further react with 9 $OH^−$ to produce $Co_9S_8O_9$ and 9 more electrons. In contrast, the Ni_3S_4 centers react with 3 $OH^−$ to produce 3 electrons and the stable $Ni_3S_4(OH)_3$ that does not react further, generating the respective oxide derivative. In all these reactions, the sulfide remains as a spectator ligand while the coordination number of the metal ion increases by one.

$$M_xS_y + nOH^− \rightarrow M_xS_yOH_n + ne^− \qquad (10)$$

$$M_xS_yOH_n + nOH^− \rightarrow M_xS_yO_n + nH_2O + ne^− \qquad (11)$$
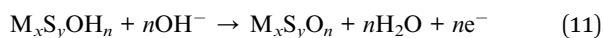
Although these are promising materials, their actual specific charge capacity, electrical conductivity, and cycling stability are quite low and hinder their electrochemical performance, such that additional improvements are needed to meet the stringent

requirements for practical applications.[54] Such drawbacks can be partially overcome by composition control and the production of mixed TMSs, whose improvements in the charge/discharge properties are not yet high enough to make those electrode materials competitive for the development of real devices. Thus, rigorous structural and morphological control also have been explored to improve the electrochemical properties of TMS-based electrodes, where the increase in the electrode surface area, the density of redox-active sites and conductivity while improving the stability are the main goals. Nevertheless, designing competitive nanostructured electrode materials based on new highly porous architectures with enhanced accessible surface area is still a big challenge but an effective strategy for improving their electrochemical performances, since it provides a much larger concentration of effective faradaic reaction sites and can decrease the resistance for the diffusion of electrolytes and charge carriers.[6,52–78]

TMSs have more recently been prepared using MOF as a sacrificial template, taking advantage of their tunable functionalities, essentially the well-ordered highly porous 3D structure with enhanced surface area and diverse morphology. Interestingly, all such good features of the parent material were shown to be preserved in the MOF-derived TMS materials, providing the most needed properties for supercapacitor applications.[6,52–78] These electrode materials have been designed to explore the easy preparation and structural stability while overcoming the poor conductivity of precursor MOFs responsible for poor electrochemical performances and cycling stability during the operation of assembled energy devices.[13] Additionally, many of the MOF-derived materials present hollow nanostructures, which combine the advantages of both the ordered high porosity and thin pore walls of the precursor MOF structure. Hollow structures tend to increase the specific charge capacity due to the enhanced contact area with the electrolyte and higher density of active redox sites, while the porous walls behave as nanosized subunits that further increase the specific surface area, minimizing the distances over which the ions should diffuse.[6,52,53,60,65,66,68,70,71,73,77,79] Thus, the sacrificial template methods rely on the site substitution of oxides/hydroxides ligands by sulfide ($S^{2−}$) ions, to generate TMSs with the finest structural control and optimized porous structure of the MOF template.

However, preparing the actual electrode optimizing the electrochemical and mechanical properties as well as the electric contact is another challenge that must be overcome. Generally, the deposition of the electroactive material on the electrode is dependent on the incorporation of a suitable binder that tends to impart significant resistance for charge diffusion. Fortunately, MOFs were found to adhere and grow on different substrates, generating stable materials constituting a very interesting strategy for the preparation of electrodes. The direct growth of MOF arrays on highly conductive substrates, *e.g.*, carbon nanotubes (CNTs), nickel foam (NF), and carbon cloth (CC), is particularly beneficial for the electrode performance since it provides stronger adhesion and excellent electric contact with the electroactive material. It also prevents the agglomeration of the transition metal sulfides due to the oriented growth and production of self-supported MOF

This journal is © The Royal Society of Chemistry 2022

J. Mater. Chem. A, 2022, 10, 430–474 | 441

nanoarrays, thus avoiding the need for binder additives that may pose unwanted resistance and reduce the effective surface area.[53,55,60,67–69,73,76]

Many MOF-derived TMSs-based supercapacitive materials have been prepared and their electrochemical properties evaluated in recent years. We have categorized them as mono-, bi- and trimetallic sulfides and they are listed in Table 1, together with the most relevant electrochemical parameters and their performances in energy storage devices, but a more in-depth analysis is generally required to understand the

improvements in performance achieved with these materials. Thus, they were subcategorized according to their structuration in conventional transition metal sulfide particles and hetero-structured materials, extending the discussion beyond the metal sites dictating the possible faradaic reactions and their major electrochemical properties.

4.1. Pristine–metal sulfide-based electrodes

The superiority of cobalt sulfides over cobalt oxides becomes apparent by the direct comparison of the results presented by
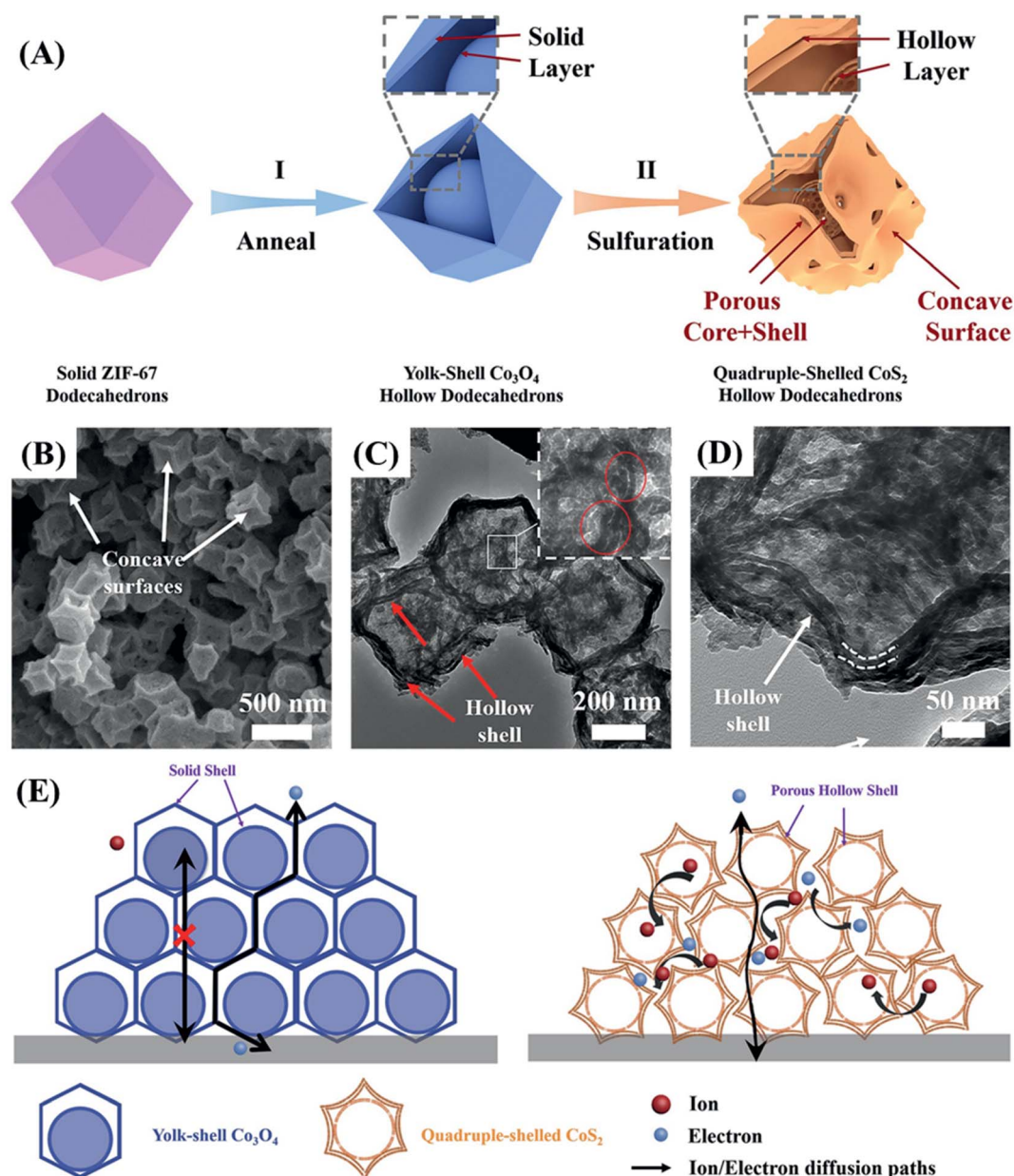
Fig. 4 (A) Schematic illustration of the fabrication process of quadruple-shelled CoS_2 hollow dodecahedron electrodes by the stepwise synthesis approach. (I) Transformation of a ZIF-67 particle to a yolk–shell Co_3O_4 hollow dodecahedron by the annealing process. (II) Formation of a quadruple-shelled CoS_2 hollow dodecahedron upon sulfidation reaction. (B) SEM and (C, D) TEM images of quadruple-shelled CoS_2 hollow dodecahedrons. (E) Schematic illustration showing the main reasons for the enhanced performance of quadruple-shelled CoS_2 hollow dodecahedrons as compared with yolk–shell Co_3O_4 hollow dodecahedrons. Reproduced with permission.[52] Copyright© 2019 Elsevier Ltd. All rights reserved.

442 | J. Mater. Chem. A, 2022, **10**, 430–474

This journal is © The Royal Society of Chemistry 2022

Jia et al.[52] for MOF-derived Co_3O_4 and CoS_2 materials and the respective electrodes prepared by slurry-casting application in supercapacitor devices. Firstly, yolk–shell Co_3O_4 dodecahedrons were prepared by the sacrificial pyrolysis of zeolite imidazole framework-67 (ZIF-67) and controlled annealing to preserve the regular structure of that precursor, obtaining a material with a specific capacity of 173C g^{-1} at 1 A g^{-1}, 45% capacity retention at 20 A g^{-1} and 80% stability retention. This was then converted into porous quadruple-shelled CoS_2 hollow dodecahedrons (Fig. 4A), which retained the dodecahedron morphology but acquired concave surfaces consistent with the interplay of the recrystallization growth mechanism during the sulfidation process. This slight morphological change was confirmed by SEM, TEM (Fig. 4B) and HRTEM images, SAED spectra, and XRD diffractograms, and the material delivered a specific capacitance of 375.2C g^{-1} at 1 A g^{-1}, about 70% capacity retention at 20 A g^{-1} and retained 92.1% of its initial capacitance even after 10 000 cycles. This work[52] demonstrated the many benefits of the structural etching provided by the sulfidation process while maintaining the highly ordered and porous morphology of the precursor MOF. It is interesting to note that these multi-shell structures not only increase the specific surface area but also provide additional shorter electron diffusion paths for the electrochemical process as compared with solid or one-shell hollow particles. Those favorable characteristics were confirmed by measurements carried out in slurry-cast electrodes, which generally present several drawbacks associated with the use of polymer binders and conductive agents that tend to reduce their overall performance. This is summarized in the schematic illustration shown in Fig. 4C, where the ion and electron paths in yolk–shell Co_3O_4 hollow dodecahedrons and quadruple-shelled CoS_2 hollow dodecahedrons are compared. Thus, the improved performance of CoS_2 over Co_3O_4 is provided not only by the substitution of oxygen atoms for sulfur atoms, but by the unique porous quadruple-shelled CoS_2 hollow dodecahedron structure obtained by the sulfidation of MOF-derived Co_3O_4. This last nanostructure provided extended electrolyte interfaces and adjoint contacts, maximizing the density of available active sites while shortening the ion and electron diffusion lengths, and avoiding strains and volume changes during the charge/discharge processes; these are key characteristics to enhance performance and durability in operation conditions.

It is known that hollow structure cavities can improve the proportion of electroactive sites and contact area with the electrolyte, which is beneficial for increasing the specific capacitance of the material only if accessible to the electrolyte. The porous and concave nanosized walls ensure a larger specific surface area while greatly shortening the diffusion lengths of ions and electrons, speeding up the charge–discharge processes.[66] In addition, the hollow interior can alleviate eventual volume expansion during the electrochemical process, preventing significant structural distortion and thus increasing the cycling stability.[79] Moreover, bi- and trimetallic sulfides exhibit superior electrochemical performance to monometallic sulfides, thanks to the synergistic contributions from the different metallic ions, enriching faradaic reactions and

increasing the electrical conductivity. Accordingly, hollow bimetallic,[60,71,73,77,79] and trimetallic[68] sulfide electrode materials, as well as those based on bulk bimetallic sulfides,[59,78] are being extensively studied.

Chameh et al.[59] and Fu et al.[78] synthesized bulk bimetallic sulfide nanoparticles with similar specific capacitances by a simple two-step hydrothermal method. A hydrothermally prepared MOF precursor was subjected to a hydrothermal sulfidation process, and the resultant materials were used to produce slurry-casted electrodes on nickel foam (NF). They also studied Zn–Co–S/NF electrodes (Fig. 5B) prepared with spherical and petal-like morphology materials derived from ZIF-50 : 50 (Zn : Co) (Fig. 5A) and compared them with a mono-metallic Co–S/NF electrode. Zn–Co–S/NF delivered a specific capacitance of 1646 F g^{-1} at 1 A g^{-1}, retaining 89.5% of this value at 15 A g^{-1} and 90% of the capacitance after 500 cycles, as compared with the Co–S/NF electrode that presented a specific capacitance of 414 F g^{-1} at 1 A g^{-1}. Fu et al.,[78] on the other hand, studied a popcorn-like Sn-doped Ni_3S_2 nanoparticles-based modified NF electrode ($Sn_xNi_{3-x}S_2$/NF), also comparing it with its monometallic Ni_3S_2 and SnS counterparts (Fig. 5C–F). $Sn_xNi_{3-x}S_2$/NF delivered a specific capacitance of 1667 F g^{-1} at 1 A g^{-1}, retaining 66.2%, and 81.8% of this value at 10 A g^{-1} and after 5000 cycles, respectively. In contrast, Co–S/NF,[59] Ni_3S_2/NF and SnS/NF[78] electrodes respectively delivered only 414 F g^{-1}, 534 F g^{-1}, and 175 F g^{-1}, even at a much lower current density of 1 A g^{-1}, demonstrating the advantages of the bimetallic materials.

These results confirmed that bimetallic sulfides present much higher performance than their monometallic counterparts due to synergistic effects involving the different metal ions. However, even though both bimetallic sulfide materials[59,78] present much larger specific capacitances, $Sn_xNi_{3-x}S_2$/NF suffers from relatively low rate capability, losing more than 33% of the specific capacitance upon a 10 fold increase in the current density. Both materials presented low rate capability when assembled in asymmetric supercapacitor devices. At high current densities, the electrochemical performance is probably being restrained by the limited ion-diffusion rates, such that only active sites next to the surface are contributing to the charge storage,[59] comparable to dense, non-nanostructured nanoparticles. Finally, despite the well-documented positive effect of a second metal ion on the capacitance of the electrode materials, the values normalized by the surface area should also be provided to make clear the influence of this factor on their performance.

A facile self-sacrificing route was employed by Li et al.[21] to prepare (Fig. 5G) MOF-derived NiS_2/ZnS hollow nanospheres (Fig. 5I and J), whereas MOF-derived $CoNi_2S_4$ hollow nanocages were produced by Wang et al.[77] and Cai et al.[79] using similar methods (Fig. 5H), both preserving the typical rhombic dodecahedron structure of ZIF-67 as illustrated in Fig. 5K–N. Slurry-casted electrodes produced with NiS_2/ZnS hollow nanospheres performed slightly behind (1198 F g^{-1} at 1 A g^{-1}) the other three materials. This sort of unexpected result can be explained, considering that it is based on a mixture of two metal sulfides with high specific capacitances, rather than a true

This journal is © The Royal Society of Chemistry 2022

J. Mater. Chem. A, 2022, **10**, 430–474 | **443**

bimetallic sulfide material. MOF-derived $CoNi_2S_4$ hollow nanocages demonstrated nearly twice the specific capacitance of CoS[77] and CoS_x,[79] its monometallic counterparts. The slurry-casted $CoNi_2S_4$ electrode prepared by Wang et al.[77] delivered a specific capacitance of 1890 F g^{-1} at 4 A g^{-1}, maintaining 81.2% of its specific capacitance at 20 A g^{-1} and 71.6% of charge capacity after 5000 cycles, whereas CoS delivered only 924 F g^{-1}, about half of the specific capacitance. Similarly, the slurry-casted $CoNi_2S_4$ electrode prepared by Cai et al.[79] presented nearly twice the specific capacitance of its monometallic counterpart, delivering a specific capacitance of 1382 F g^{-1} at 1 A g^{-1} with 83.6% of capacitance retention at 10 A g^{-1} and 70% of charge capacity after 10 000 cycles, while CoS_x delivered only 774 F g^{-1}.

The superior performance of these bimetallic sulfides can be explained by the incorporation of Ni^{2+}, an element exhibiting
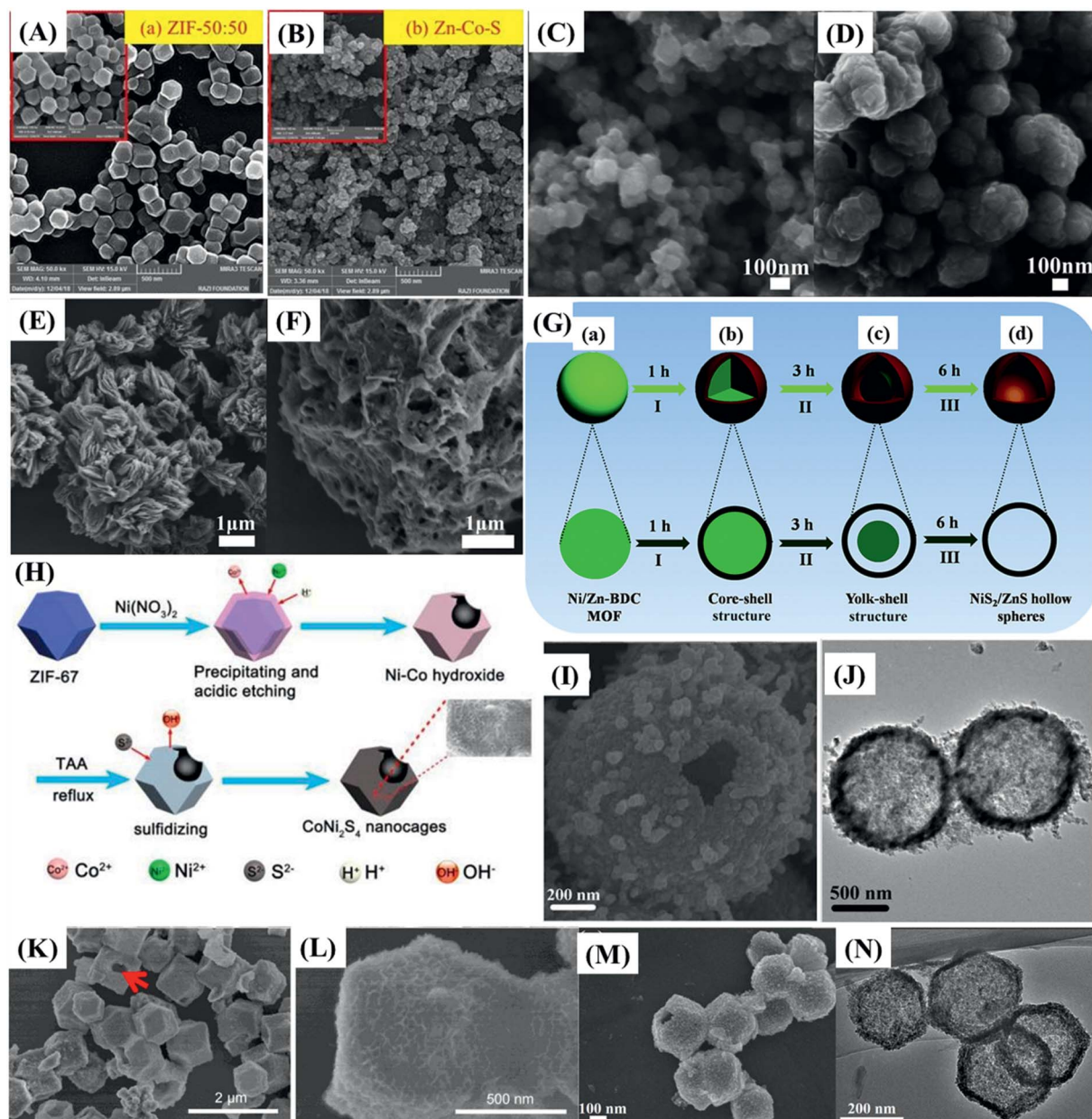
Fig. 5 FESEM images of (A) ZIF-50 : 50 and (B) Zn−Co−S. Reproduced with permission.[59] Copyright© 2019 Elsevier B.V. All rights reserved. FESEM images of (C) the Ni−Sn MOF precursor and (D) $Sn_xNi_{3−x}S_2$. SEM images of (E) Ni-MOF precursor and (F) NiS. Reproduced with permission.[78] Copyright© 2020 Elsevier B.V. All rights reserved. (G) Schematic illustration of the fabrication process of NiS_2/ZnS hollow nanospheres. Reproduced with permission.[71] Copyright Marketplace™, Royal Society of Chemistry. (H) Schematic illustration of the $CoNi_2S_4$ hollow nanocage fabrication process. Reproduced with permission.[77] Copyright© 2017. Published by Elsevier B.V. (I) SEM and (J) TEM images of NiS_2/ZnS. Reproduced with permission.[71] Copyright Marketplace™, Royal Society of Chemistry. (K−L) SEM images of cobalt-nickel sulfide nanocages. Reproduced with permission.[77] Copyright© 2017. Published by Elsevier B.V. (M) FESEM and (N) TEM image of $NiCo_2S_4$. Reproduced with permission.[79] Copyright© 2019 Elsevier B.V. All rights reserved.

well-known redox properties, in comparison with Co^{2+}, the previous element in the periodic table of elements. The similarity in size and properties of these elements provides a better match and occurrence of multiple valence states to the material, which is translated in a narrower band gap and improved electric conductivity. The increased porosity and roughness induced by the diffusion of Ni^{2+} and Co^{2+} through the shell during the cation exchange processes in the synthesis also enhance the surface area and the density of electrochemically active sites.
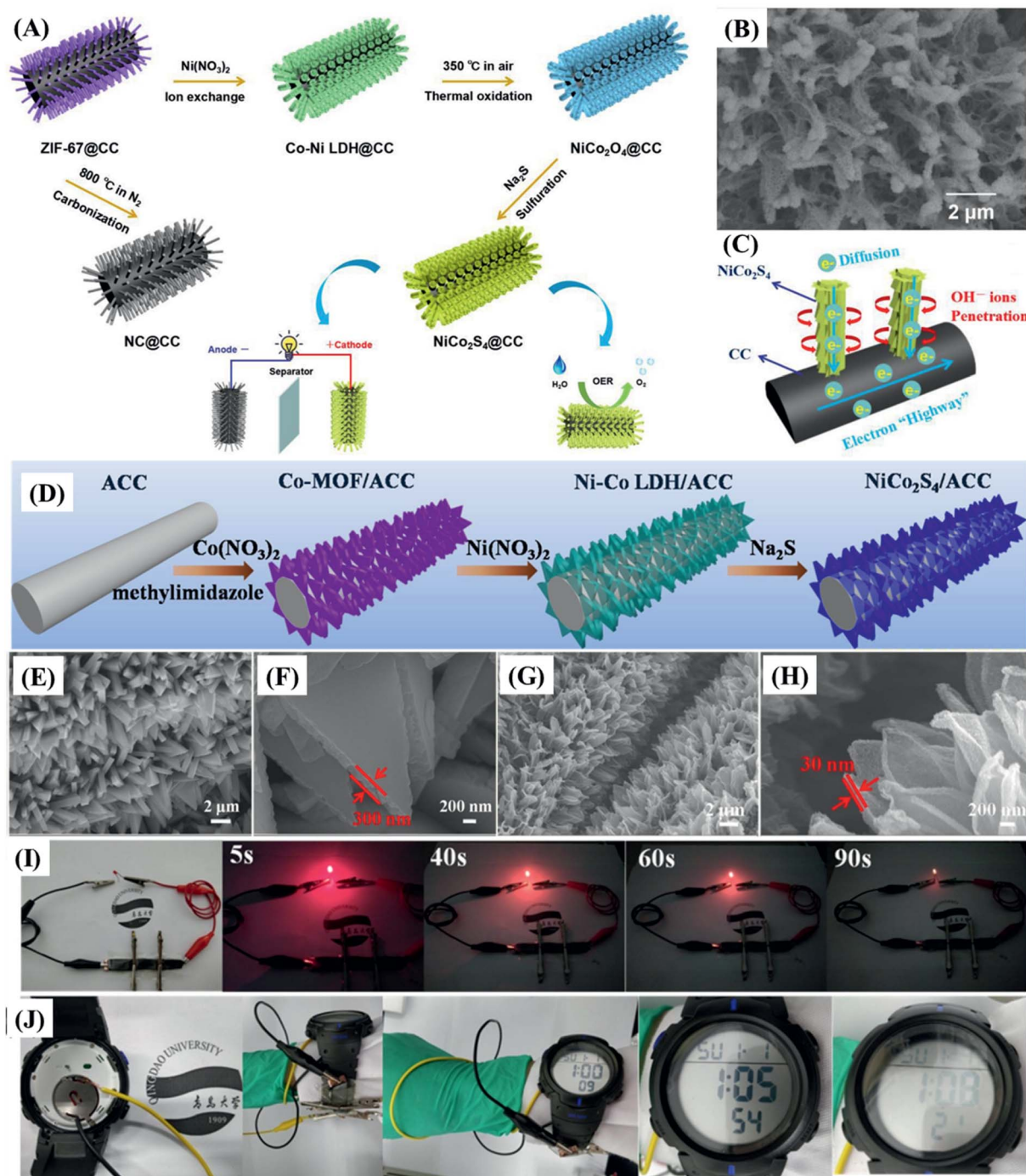
Fig. 6 (A) Schematic illustration of the fabrication process of $NiCo_2S_4$@CC for asymmetric supercapacitors and electrocatalysis. (B) SEM images of $NiCo_2S_4$@CC; (C) the mechanism of the synergistic effects. Reproduced with permission.[73] Copyright© 2020 Elsevier Ltd. All rights reserved. (D) Schematic illustration of the synthesis of MOF-derived ultrathin $NiCo_2S_4$ nanoarrays on electrochemically activated carbon cloth. (E and F) SEM images of Co-MOF/ACC and (G, H) $NiCo_2S_4$/ACC. (I) The brightness of a light-emitting diode (LED) bulb recorded as a function of time. (J) Electronic watch operated by three charged supercapacitors (green wristband). Reproduced with permission.[60] Copyright© 2019 Elsevier B.V. All rights reserved.

It should be emphasized here that slurry-casted electrodes incorporate a "dead mass" of polymer binders and conductive agents that not only block the electrochemically active sites but also increase the device weight and contribute negatively to the specific charge capacity and rate capability, given the resistance and poor electrochemical cyclability of the resultant materials. Zhao et al.[60] and Wang et al.[73] proposed carbon cloth (CC), lightweight materials presenting excellent conductivity, robustness, and flexibility, as ideal electrode substrates, especially when electrochemically treated (denoted as activated carbon cloth, ACC), conferring excellent hydrophilic character for the direct deposition/growth of bimetallic nickel–cobalt sulfide. This strategy eliminates the negative burden of the binder and other additives, delivering the maximum performance of the electrode materials, which is the reason it should be employed in high-performance energy storage and conversion devices.

Wang et al.[73] reported a "one for two" strategy to prepare MOF-derived $NiCo_2S_4$ nanorods directly on carbon cloth ($NiCo_2S_4$@CC) (Fig. 6A), minimizing the interfacial resistance

since it provides the best electrical contact between the active materials and conductive substrates while avoiding the use of "dead mass". The growth of nanostructured materials on the surface greatly increased the specific surface area and made it possible to optimize the electrolyte/active material interface, exploiting the large diameter of CC carbon fibers (Fig. 6B and C). The $NiCo_2S_4$@CC electrode exhibited a specific capacitance of 879.6 F g^{-1} at 1 A g^{-1}, which is significantly higher than that presented by $NiCo_2O_4$@CC (702.4 F g^{-1}) and Co–Ni LDH@CC (577.6 F g^{-1}) precursor electrodes. However, this result is still behind that presented by the $NiCo_2S_4$/ACC and Ni–Zn–Co–S/NF electrodes, as described in detail below.

Zhao et al.[60] proposed the synthesis of MOF-derived ultrathin and porous $NiCo_2S_4$ hollow nanosheets arrays with enriched edge sites on electrochemically-activated flexible carbon cloth (Fig. 6D–H), which delivered 2392 F g^{-1} at 1 A g^{-1} and maintained 80.3% of this value at 20 A g^{-1}, with a cycling stability of 85.1% after 10 000 cycles, when assembled in a supercapacitor device. The potential for real application of $NiCo_2S_4$/ACC
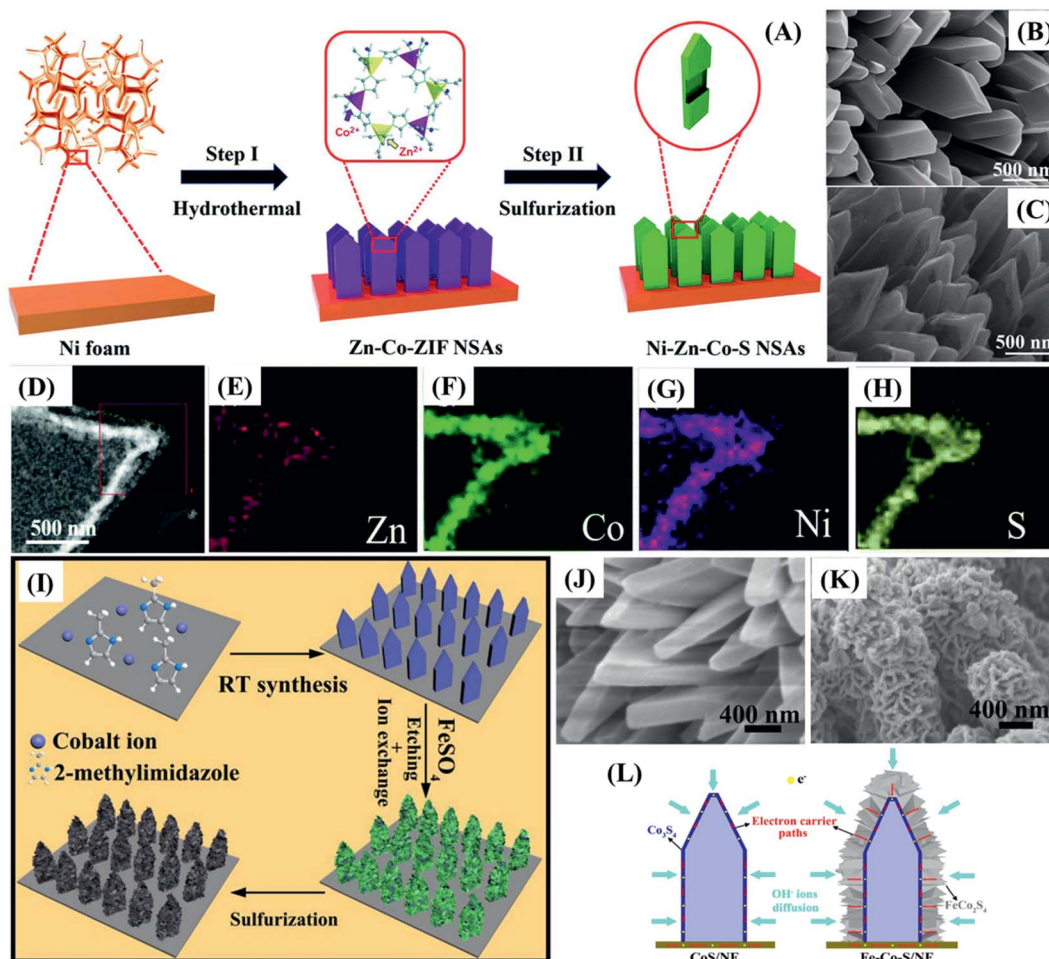

Fig. 7 (A) Schematic illustration showing the growth of Ni–Zn–Co–S NSAs on the NF substrate. (B) SEM images of solid Zn–Co-ZIF NSAs and (C) hollow Ni–Zn–Co–S NSAs on the NF substrate at different magnifications. (D) HAADF image and (E–H) EDS elemental mappings of different elements. Reproduced with permission.[68] Copyright Marketplace™, Royal Society of Chemistry. (I) Schematic illustration of the Co_3S_4@$FeCo_2S_4$/NF electrode fabrication process. SEM images of (J) Co-MOF/NF and (K) Co_3S_4@$FeCo_2S_4$/NF electrodes. (L) Scheme showing the charge carrier diffusion during the charging of CoS/NF and Fe–Co–S/NF electrodes. Reproduced with permission.[57] Copyright© 2019 Elsevier Ltd. All rights reserved.

electrodes in supercapacitors was illustrated by supplying energy to a light-emitting diode (LED) (Fig. 6I), and an electronic watch (Fig. 6J, three supercapacitors in the green wristband). Huang et al.,[68] on the other hand, developed strategies for the preparation/growth of mesoporous and hollow trimetallic sulfide materials, namely Ni–Zn–Co–S nano-sword arrays (NSAs), directly onto nickel foam (NF) substrates by a two-step method (Fig. 7A–C). The Ni–Zn–Co–S/NF electrode delivered a specific charge capacity of 358.1 mA h g^{-1} (2343.9 F g^{-1} from our estimate from the corresponding GCD), retention of 64.9% of that value at 100 mA cm^{-2}, and charge capacity of 85% after 1000 cycles.

The outstanding performances of both electrodes are attributed not only to the exceptional benefits provided by the hollow mesoporous structured metal sulfide, boosting the interface contact area and the diffusion of electrolyte but also to the following: (1) the bimetallic[73] and trimetallic[60] compositions ensure even higher electrical conductivity and density of electrochemical reaction sites in comparison to monometallic sulfides; (2) the binder-free direct contact of the electrode substrate (ACC[73] and NF[60]) and the active material providing good electrical contact and mechanical adhesion; (3) the high conductivity and wettability of ACC and NF, facilitating and speeding up the electron and ion transport; (4) the unique properties of nanostructured nanosheet[73] and nano-sword[60] arrays, especially their exceptionally high surface area and voids, more completely exposing the active material to the electrolyte (Fig. 7D–H).

A binder-free MOF-derived hierarchical core@shell Co_3S_4@-$FeCo_2S_4$/NF electrode was produced by Le et al.[57] by controlling the etching/ion-exchange reaction between Co-MOF and $FeSO_4$, and the subsequent solvothermal sulfidation generating a hierarchical core@shell hollow nanostructure with a shell of $FeCo_2S_4$-nanosheets coating on the Co_3S_4 hollow nanoarray directly deposited on Ni foam (Fig. 7I). The core@shell hollow nanostructures (Fig. 7K) can significantly improve the electrochemical performance of the electrode by providing a higher density of accessible active sites, presenting synergistic effects. The hollow Co_3S_4 nanoarray core directly grown on nickel foam served as electron transfer channels to the $FeCo_2S_4$ nanosheets shell while providing more accessible active sites, bestowing superior electroactivity and electrical conductivity associated with its bimetallic composition. Such a highly nanostructured system ensures a larger electrode/electrolyte contact area, providing abundant electrochemical active sites with richer redox properties while accommodating more capacitive double-layer charges (Fig. 7L). Accordingly, the Co_3S_4@$FeCo_2S_4$/NF electrode delivered 2695 F g^{-1} at 1 A g^{-1}, much more than the CoS/NF electrode (1500 F g^{-1} at 1 A g^{-1}), a rate capability of 69.8% at 10 A g^{-1}, and capacitance retention of 84% after 1000 cycles.

4.2. Carbonaceous support for metal sulfide nanocomposites and hybrid materials

The relevance of materials and frameworks with excellent conductivity and surface area cannot be neglected and are fundamental for the design of high-performance electrodes,

whose active material delivers the best of its performance, especially when it is directly deposited on their surface, minimizing the contact resistances. This is a general approach that has provided much better results than using the slurry-casting method for the production of electrodes made of nanocomposites and hybrid materials based on MOF-derived cobalt sulfides. Such supporting structures serve as the bridge between the electrode active material and the current collector,[62,65,66,70,72] or electrode materials themselves.

Among the possibilities, carbonaceous materials such as carbon nanotubes (CNTs),[62,64,65,69] reduced graphene oxide,[74] and other carbon nanostructures[55,58,61,70,72] are being extensively investigated as electrode materials of electric double-layer capacitors (EDLCs), given their large specific surface area, high electric conductivity, undisputable chemical and mechanical stability, and ecofriendly nature. Despite all these excellent characteristics, EDLCs present relatively low specific capacitance and energy density, which limit their use.[62,65] However, such a drawback can be easily overcome by depositing a battery-type or pseudo-supercapacitive material that can provide a high density of redox sites. Such a synergistic association is extremely well suited with cobalt sulfides, especially by the direct production/deposition of nanoparticles on the surface. The resultant materials exhibit enhanced electrochemical performances, given the improved electric conductivity and good overall stability. However, there are few reports on this kind of nanocomposite, due to the difficulties in adjusting the production process of MOF-derived nanostructured materials with suitable physicochemical and adhesion properties on those carbon materials.[65] In this context, nanocomposites based on MOF-derived cobalt,[62,65] and copper[69] sulfides on CNTs were successfully prepared and considered for application in supercapacitor devices, as discussed below.

Zou et al.[62] prepared highly dispersed CoS_2 nanoparticles, embedded in a CNT network matrix, with tunable pore size diameters, by the in situ gas-sulfidation of three different Co@CNTs nanocomposites. They were produced via the calcination-thermolysis of Co-MOF precursors based on o-, m- and p-bdc^{2-} ligands (Fig. 8A–C), as cationic cobalt species can catalyze the graphitization process, thus playing a crucial role in the formation of negatively charged CNTs. The slurry-casted p-CoS_2@CNTs electrode presented the highest performance, delivering the specific capacitance of 825 F g^{-1} at 0.5 A g^{-1}, rate capability of 32.5% at 10 A g^{-1}, and capacitance retention of 82.9% after 5000 cycles. Niu et al.[69] used an in situ approach to prepare MOFs-derived CuS polyhedrons embedded in interpenetrating CNTs networks (CuS/CNTs, or CCS), using a mixture of positively charged copper hydroxide nanowires (CHNs) and CNTs as precursors, producing flexible and binder-free thin films (Fig. 8D and E). The CuS/CNTs electrode delivered a specific capacitance of 606.7 F g^{-1} at 1 A g^{-1} and presented a rate capability of 44.5% but the cycling stability was not measured. Similarly, Yang et al.[64] realized a slurry-casted Ni–Ni_3S_4@NC/CNTs electrode, based on a nanocomposite of CNTs and Ni–Ni_3S_4 nanoparticles core and nitrogen-doped carbon shell. This nickel sulfide-based material was obtained upon controlled calcination/sulfidation of Ni-MOF/CNTs composite

This journal is © The Royal Society of Chemistry 2022

J. Mater. Chem. A, 2022, 10, 430–474 | 447

assembled by compounding a nitrogen-rich functional ligand (H_6TDPAT) with CNTs (Fig. 8F and G). Ni–Ni_3S_4@NC/CNTs presented a specific capacitance of 1490 F g^{-1} at 1 A g^{-1}, much higher than that of NiO/Ni/CNTs (320 F g^{-1}), Ni–Ni_3S_4@NC (484 F g^{-1}), Ni-MOF/CNTs (55.9 F g^{-1}) electrodes, and all other CNTs-based nanocomposites,[62,65,69] in addition to a rate capacity of 53.7% at 10 A g^{-1} and capacitance retention of 84% after 5000 cycles.

The improved performance of that nanocomposite can be associated with the incorporation of CNTs, which greatly enhanced the electron-transfer rate and the electrochemical stability since they act as conducting bridges interconnecting the CoS_2,[62] CuS,[69] and Ni–Ni_3S_4 nanoparticles.[64] The abundant inherent porosity and larger pore size of p-CoS_2@CNTs in comparison to o-CoS_2@CNTs and m-CoS_2@CNTs, inherited from its MOF precursor structure, provided a better electrolyte

Fig. 8 (A) Schematic illustration of the preparation of CoS_2@CNTs. (B and C) FESEM images of p-CoS_2@CNTs. Reproduced with permission.[62] Copyright© 2017, American Chemical Society. (D) Schematic illustration of the preparation process of the HKUST-1-derived CuS polyhedron nanocomposite interspersed in carbon nanotubes thin film (CCS). (E) Typical SEM images of CuS/CNTs thin film. Reproduced with permission.[69] Copyright© 2019 Elsevier Ltd. All rights reserved. (F) Scheme of the synthesis of the MOFs-derived Ni–Ni_3S_4@NC/CNTs composite. (G) SEM images of Ni–Ni_3S_4@NC/CNTs. Reproduced with permission.[64] Copyright© 2020 American Chemical Society. Schematic illustration of the preparation of Co_3S_4/MWCNT, presenting the (H) whole process and (I) the formation of the hollow Co_3S_4 on interpenetrating the MWCNT structure. (J) FESEM and (K) TEM images of the Co_3S_4/MWCNT. Reproduced with permission.[65] Copyright© 2018, American Chemical Society.

diffusion and higher density of active sites.[62] Additionally, the interpenetrating CNTs network in CuS/CNTs[69] and Ni–Ni_3S_4@NC/CNTs[64] electrodes not only increased the electrical conductivity further but also enhanced the overall mechanical stability of the material and ensured the access of the electrolyte to more redox sites, making them electrochemically active. Additionally, the nitrogen doping and the presence of nickel sites in Ni–Ni_3S_4@NC and Ni–Ni_3S_4@NC/CNTs could further improve the electrical conductivity of these materials. However, the slow ion and associated electron diffusion rates should limit the rate capability at higher current densities.

Tian et al.[65] combined the benefits of interpenetrating CNTs with the superior electrochemical performance of hollow nanoparticles, presenting an electrode with slightly higher specific capacitance, limited by the density of active sites but with much superior rate capability. They reported the MOF-template-assisted synthesis of a hollow quasi-polyhedron Co_3S_4/MWCNT nanocomposite by the functionalization of multiwalled carbon nanotubes (MWCNTs), the preparation of ZIF-67/MWCNT via a solvothermal process, and subsequent sulfidation and thermal annealing (Fig. 8H and I). The Co^{2+} ions added to the suspension were first electrostatically attracted by the negatively charged functionalized MWCNTs, adsorbing on them. Then, ZIF-67 was directly grown on the interpenetrating MWCNTs network by coordination-induced self-assembly of Co^{2+} ions with 2-methylimidazole (Fig. 8J and K). The electrode made with this nanocomposite delivered a specific capacitance of 850.3 F g^{-1} at 2 A g^{-1} with 81.9% rate capability at 30 A g^{-1}, and capacitance retention of 78.98% after 5000 cycles. Such good results can be associated with improved electron and ion transport between nanoparticles, and increased overall stability provided by the interpenetrating MWCNTs network and hollow ZIF-67 structure of the nanoparticles, which mitigate the negative effects of volume expansion during the charge/discharge processes. The high specific surface area, a consequence of abundant micro- and mesopores providing suitable pathways for electrolyte diffusion increasing the density of active sites, also plays a major role.

In addition to CNTs, reduced graphene oxide (rGO) can be used as a suitable conducting support for the growth of MOF structures and the subsequent sulfidation to generate interesting metal sulfide nanocomposites. In this context, a hierarchical porous hybrid electrode composed of α-NiS nanorods decorated rGO (α-NiS/rGO) was prepared by a facile in situ sulfidation of Ni–MOF-74/rGO (Fig. 9A and B) by Qu et al.[74] The α-NiS/rGO electrode delivered a specific capacity of 744C g^{-1} (1488 F g^{-1}) at 1 A g^{-1} and rate capacitance of 80.6% at a current density of up to 50 A g^{-1}, and capacitance retention of 89% after 20 000 cycles. In contrast to CNTs, rGO behaves as a flexible sheet and can wrap the nanoparticles to provide improved electric contact and electronic conductivity for fast energy storage, while the hierarchical porous structure of the nanohybrid facilitates electrolyte diffusion to the active sites of the nanocomposite material. It also confers the electrode with a huge enhancement of the electrochemical and mechanical stability, as well as surface area, thus providing very high specific capacitance. On the other hand, rough α-NiS nanorods

also exhibit high surface area, high density of enriched electrochemical sites, and good structural stability against volume change effects upon potential cycling, even further enhancing the electrochemical performance and long-term stability on cycling. The 1D morphology is far less prone to volumetric changes as compared to 3D bulk structures.

Carbon nanocomposites can also be realized by decorating high-surface-area porous carbon materials prepared by pyrolysis of MOFs with metal oxide or sulfide nanoparticles,[61,63,72] or as reported by Li et al.[61] who prepared a series of nanocomposites based on divalent metal (M = Co^{2+}, Zn^{2+}, Cd^{2+}, Ni^{2+}, and Cu^{2+}) sulfide particles surrounded by a carbon matrix (M_xS_y@C). Such materials were prepared by a one-pot calcination–sulfidation of M–MOF precursors, where the slurry-casted NiS_2@C electrode presented the highest specific capacitance of all of them, delivering a specific capacitance of 833 F g^{-1} at 0.5 A g^{-1} (55.8% of rate capability at 10 A g^{-1}), and 81.6% of capacitance retention after 5000 cycles. The superior performance of this electrode in comparison to the other M_xS_y@C electrodes was attributed to the highly porous 3D MOF-derived structure of NiS_2@C, associated with the high theoretical capacitance of NiS_2 and surface area of the graphitic material, and also to the nanostructure improving the mass transfer and electrolyte diffusion. Poor rate capability was observed at large charge–discharge current densities, probably caused by slow electrolyte diffusion and lower usage of the active sites under higher demand.

Another interesting example was presented by Liu et al.[72] who reported a simple method for the preparation of Co_9S_8@S,N-doped carbon cuboids (Co_9S_8@SNCC), using S,N-containing Co-MOFs nanocrystals as the precursor with controllable morphologies and sizes. A further thermal treatment led to its conversion to Co_9S_8@S,N-doped carbon bulk (Co_9S_8@SNCB) (Fig. 9C) having Co_9S_8 nanoparticles dispersed in a porous carbon network (Fig. 9D). The slurry-casted Co_9S_8@SNCC electrode delivered 429 F g^{-1} at 1 A g^{-1}, 78.3% rate capability at 20 A g^{-1}, and 98% capacitance retention after 2000 cycles, presenting superior performance as compared to a similar Co_9S_8@SNCB electrode (320 F g^{-1} at 1 A g^{-1}). This behavior can be attributed to the intimate interaction between the graphitic carbon and Co_9S_8 nanoparticles, which limits the strain and volume changes while increasing the electric conductivity and rate capability, even considering a slurry-casted electrode.

As an attempt to further optimize the properties of hybrid carbon-based materials, Yi et al.[63] presented a core@shell nanosphere structure (Ni–Co–S@NC) made of hollow Ni–Co–S (core) and N-doped carbon (NC) (shell). The core was prepared by the calcination of NiCo-MOF nanospheres to produce hollow Ni–Co_n alloy nanoparticles (n value = Ni/Co molar ratio) coated with NC, and subsequent sulfidation (Fig. 9E–J) in which the catalytic effect of Ni and Co nanoparticles induced the formation of graphitic carbon during the calcination process. The slurry-casted Ni–Co–S@NC electrode presented a specific charge capacity of 543.9C g^{-1} (988.9 F g^{-1}) at 1 A g^{-1}, 67.3% rate capability at 20 A g^{-1}, and near 100% capacity retention after 2000 cycles. The outstanding cycling stability indicates that the

This journal is © The Royal Society of Chemistry 2022
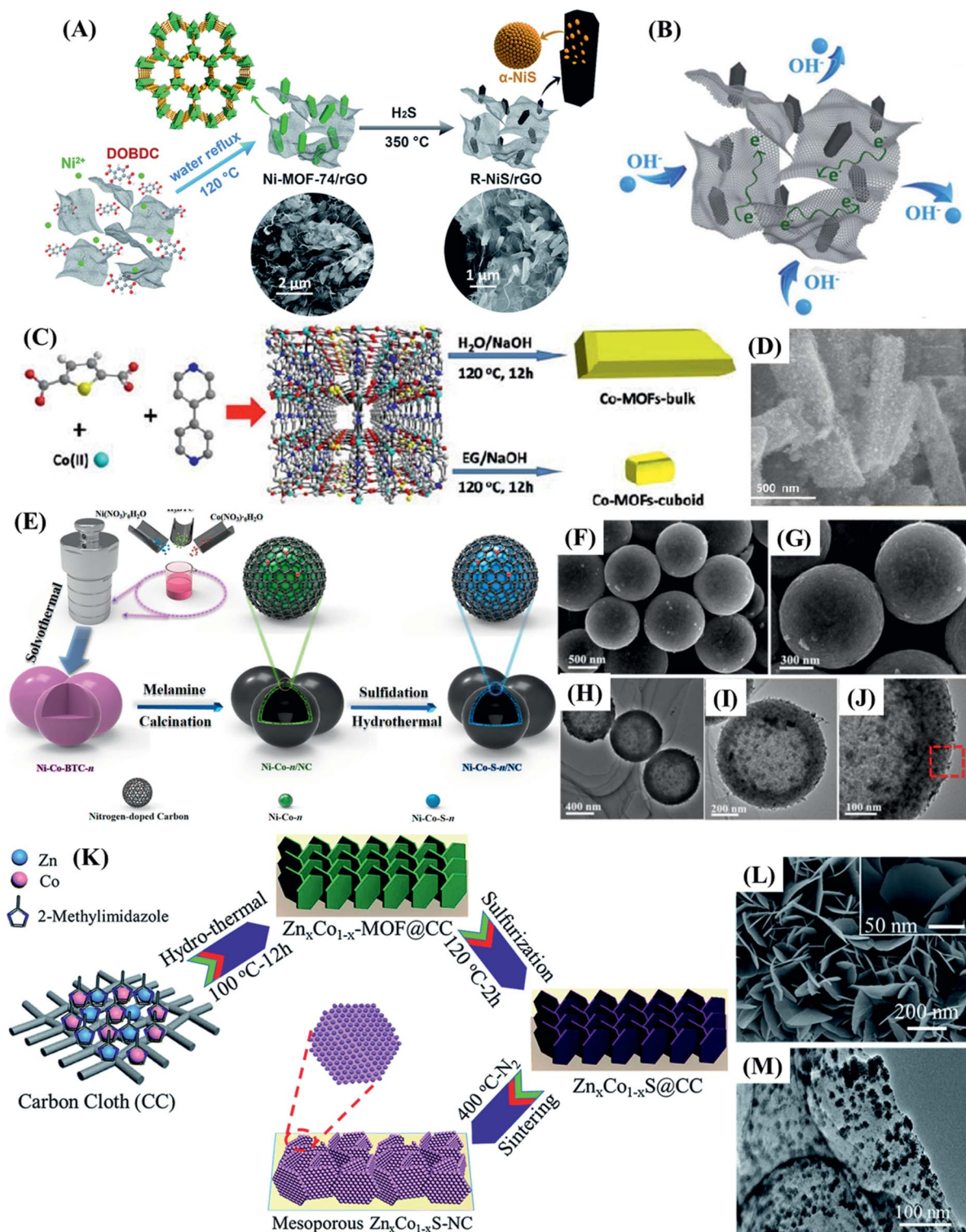
J. Mater. Chem. A, 2022, **10**, 430–474 | **449**

Fig. 9 (A) A schematic illustration of the synthesis procedure of R-NiS/rGO and its precursors. (B) A schematic illustration of the R-NiS/rGO structure and electron conduction pathway along the rGO sheets. Reproduced with permission.[74] Copyright Marketplace™, Royal Society of Chemistry. (C) Schematic illustration of the Co-MOFs crystals preparation process in water and ethylene glycol. (D) SEM image of Co_9S_8@SNCC. Reproduced with permission.[74] Copyright Marketplace™, Royal Society of Chemistry. (E) Procedure for the preparation of hollow Ni−Co−S@NC core@shell nanocomposites and the respective (F and G) SEM and (H–J) TEM images at different magnifications. Reproduced with permission.[63] Copyright© 2019 American Chemical Society. (K) Scheme illustrating the preparation process of MOF-derived nanosheets on carbon cloth and their conversion into mesoporous $Zn_{0.76}Co_{0.24}S$ nanoparticles embedded in N-doped carbon ($Zn_{0.76}Co_{0.24}S$-NC). (L) FESEM image of mesoporous $Zn_{0.76}Co_{0.24}S$-NC on a carbon cloth substrate. (M) TEM image of $Zn_{0.76}Co_{0.24}S$-NC. Reproduced with permission.[55] Copyright Marketplace™, Royal Society of Chemistry.

450 | J. Mater. Chem. A, 2022, 10, 430–474

This journal is © The Royal Society of Chemistry 2022

NC is effectively preventing the aggregation and solubilization of the encapsulated Ni–S nanoparticles during the charge/discharge processes, whereas the relatively high electrochemical performance is attributed to the synergistic effects of the bimetallic sulfide and N-doped graphitic carbon. The decay of the specific capacity in higher current densities was expected, considering the limitations imposed by resistance in a slurry-casted electrode.

The incorporation of carbonaceous materials into MOF-derived transition metal sulfides was performed by a different method by Javed *et al.*,[55] who obtained a binder-free and highly porous electrode made of mesoporous bimetallic sulfide nanoparticles ($Zn_{0.76}Co_{0.24}S$) embedded in ultra-thin nitrogen-doped carbon directly grown on a flexible carbon cloth ($Zn_{0.76}Co_{0.24}S$-NC/CC). The materials were produced by the controlled heat treatment of the MOF-derived $Zn_{0.76}Co_{0.24}S$/CC precursor in a N_2 atmosphere followed by annealing (Fig. 9K–M). This unique electrode delivered a specific capacitance of 2133.2 F g^{-1} at 1.25 A g^{-1}, 76.4% of rate capacity at 20 A g^{-1}, and 95.63% of charge capacity retention after 10 000 cycles, a value nearly 2.5 times larger than the specific capacitance of its oxide counterpart, $Zn_xCo_{x-1}O$-NC/CC (847.78 F g^{-1} at 1.25 A g^{-1}). The MOF-derived precursor prepared with an organic bridging ligand provided increased surface area and pore diameter to $Zn_{0.76}Co_{0.24}S$-NC/CC, resulting in enhanced ion diffusion rates and the capacity to buffer geometric changes, thus improving the rate capability and stability on cycling. In addition, the abundant content of pyridyl N-atoms in the carbon matrix generated many extrinsic defects and binding sites for the $Zn_{0.76}Co_{0.24}S$ nanoparticles and for electrochemical reactions.

These contributions seem to significantly improve the pseudo-capacitive charge storage, the conductivity, and overall stability of the electrode, constituting additional features that can be synergistically implemented to improve the performance of sulfide-based electrode materials.

A similar strategy was proposed by Wang *et al.*[56] to produce binder-free electrodes based on CC, but using a MOF-derived carbonaceous material to assemble a CNWAs@Ni@CoNi$_2$S$_4$/CC electrode. The MOF-derived carbon nanowall arrays (CNWAs) were initially fabricated on carbon cloth (CC) as the secondary substrate by a calcination method, followed by electrodeposition of a Ni metal layer, and final coating with CoNi$_2$S$_4$ nanosheet arrays (Fig. 10A–C). The CNWAs@Ni@CoNi$_2$S$_4$/CC electrode delivered the superb specific capacitance of 3163 F g^{-1} at 1 A g^{-1}, which is the highest of all MOF-derived electrode materials presented in this review, with a rate retention of 47.5% at 40 A g^{-1} and 95.5% of charge capacity retention after 10 000 cycles. Furthermore, it delivered 2825 F g^{-1} at a scan rate of 5 mV s^{-1}, whereas the similar CNWAs@CoNi$_2$S$_4$/CC and Ni@CoNi$_2$S$_4$/CC (Fig. 10D and E) electrodes delivered only 2035 and 1030 F g^{-1}, respectively. The outstanding performance of the CNWAs@Ni@CoNi$_2$S$_4$/CC electrode is attributed to some synergistic effects as follows. (a) The CC free-standing current collector; (b) the high surface area CNWAs uniformly distributed on the surface of CC, acting as a secondary substrate for the deposition of high mass loadings of CoNi$_2$S$_4$ nanosheet arrays while minimizing the "dead mass"; (c) the electrodeposition of the Ni layer on CNWAs/CC, reducing the interfacial resistance of CNWAs and CoNi$_2$S$_4$ nanosheet arrays while increasing the ion/electron diffusion rates; (d) the vertically
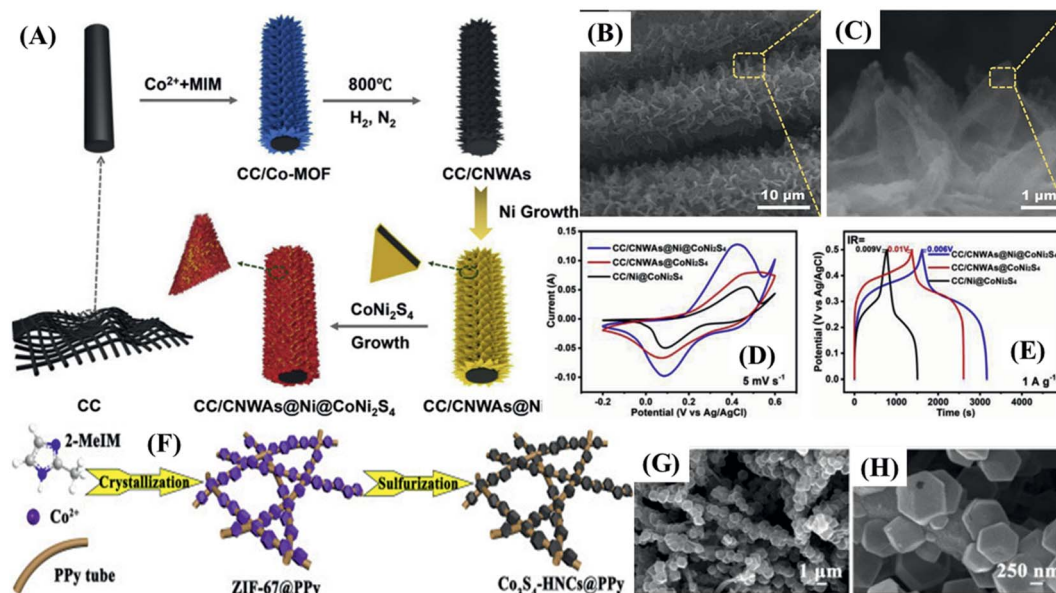

Fig. 10 (A) Scheme illustrating the preparation of the hierarchical CNWAs@Ni@CoNi$_2$S$_4$/CC electrode. (B) Low- and (C) high-magnification SEM images of CNWAs@Ni@CoNi$_2$S$_4$/CC nanosheet arrays electrode. (D) CV curves of CC/Ni@CoNi$_2$S$_4$, CC/CNWAs@CoNi$_2$S$_4$, and CC/CNWAs@Ni@CoNi$_2$S$_4$ electrodes at a scan rate of 5 mV s^{-1}. (E) GCD curves of the CC/Ni@CoNi$_2$S$_4$, CC/CNWAs@CoNi$_2$S$_4$, and CC/CNWAs@Ni@CoNi$_2$S$_4$ electrodes at a current density of 1 A g^{-1}. Reproduced with permission.[56] Copyright© 2019 Elsevier Ltd. All rights reserved. (F) Scheme illustrating the fabrication process of the Co$_3$S$_4$–HNCs@PPy hybrid. (G and H) FESEM images of Co$_3$S$_4$–HNCs@PPy. Reproduced with permission.[70] Copyright© 2020 Elsevier Ltd. All rights reserved.

This journal is © The Royal Society of Chemistry 2022

J. Mater. Chem. A, 2022, **10**, 430–474 | **451**

aligned $CoNi_2S_4$ nanosheet arrays providing high specific surface area and suitable electroactive sites, thus optimizing electrode/electrolyte interfaces until medium current densities are achieved (up to 40 A cm^{-2}).

Although those authors were able to successfully produce such nanocomposites, it is quite difficult to incorporate carbonaceous materials into MOF-derived materials, such that polymers have been used as a convenient strategy to incorporate highly conductive materials on them.[58,70] In contrast to carbonaceous materials, conducting polymers such as polypyrrole (PPy) can be conveniently prepared by *in situ* polymerization.[58,70] Liu *et al.*[58] assembled a Cu_9S_8@C@PPy/CC electrode by slurry-casting on CC the Cu_9S_8@C nanocomposite obtained by the calcination–vulcanization of a Cu-MOF (HKUST-1) with Cu_9S_8 bulk nanoparticles embedded in amorphous carbon, and finally electrodepositing PPy. The GCD curves of the Cu_9S_8@C@PPy/ CC electrode indicated a much higher specific capacitance as compared to Cu_9S_8@C/CC and Cu_9S_8/CC, demonstrating the beneficial role of conducting polymers on the electrode performance. Nevertheless, similar to slurry-casted electrodes based on bulk monometallic sulfide nanocomposites, it delivered only 270.72 F g^{-1} at 10 mV s^{-1}, with a poor rate capability of 44.7% at 100 mV s^{-1}, and 80.4% of capacitance retention after 3000 cycles. These results demonstrate the key relevance of surface area and concentration of electroactive sites to the electrode performance.

On the other hand, Cheng *et al.*[70] proposed a nanocomposite made of Co_3S_4 hollow nanocages (HNCs) derived from ZIF-67 inlaid in polypyrrole (PPy) tubules. In this way a Co_3S_4– HNCs@PPy hybrid with an intertwined "Co_3S_4-to-PPy-to-Co_3S_4" conductive network connecting them was prepared *via* a facile solution method (Fig. 10F) that retained the hierarchical mesoporous structure of the ZIF-67@PPy precursor after the sulfidation process (Fig. 10G and H), allowing fast electrolyte diffusion while improving the electric contacts and conductivity, thus enhancing the transport of charge. The properties of this nanocomposite material were similar to those of the hollow quasi-polyhedron Co_3S_4/MWCNT nanocomposite prepared by Tian *et al.*,[65] since both present penetrating and interconnecting charge-transfer networks intertwined into embedded hollow metal sulfide nanoparticles. Nevertheless, the slurry-casted Co_3S_4–HNCs@PPy electrode delivered 1706 F g^{-1} at 1 A g^{-1} and rate capacitance of 73.2% at 10 A g^{-1}, and retained 68.5% of its capacitance after 5000 cycles. These results are remarkably superior to those delivered by Co_3S_4–HNCs (480.4 F g^{-1}), PPy (115 F g^{-1}) and ZIF-67@ppy (93.6 F g^{-1}) electrodes at the same current density, and a physical mixture of PPy and Co_3S_4 (800.4 F g^{-1}). Clearly, the intertwined PPy plays a similar role to MWCNT connecting the Co_3S_4–HNCs nanoparticles and increasing the density of electroactive sites, while reducing the average charge diffusion length in the Co_3S_4 hollow nanocages, thus explaining the superior performance of the Co_3S_4– HNCs@PPy electrode. In fact, the optimized structure of the MOF-derived metal sulfide and strong electronic interaction with the polymer chain generates highways for fast charge transfer along the "Co_3S_4-to-PPy-to-Co_3S_4" networks. The inlaying of Co_3S_4–HNCs on PPy not only assured the intimate

electrical contact of all components of the nanocomposite but also prevented aggregation, thus improving the conductivity and mechanical stability of the electrode.

4.3. Non-carbonaceous support for metal sulfide nanocomposites and hybrid materials

Another strategy for producing high-performance nanocomposites and hybrid materials is substituting carbon-based materials with conducting materials such as layered double hydroxides (LDH),[6,53,67] ultrathin MnO_2 nanosheets,[66] metal alloys,[54] or even NiCoZn–S nanosheets.[76] These can be advantageously used as co-supports given the higher compatibility and adhesion/compatibility of metal sulfide nanoparticles, generating larger surface area, and more stable and electrochemically active interfaces. Fortunately, the highly demanded construction of multidimensional hierarchical nanoarrays with an optimal architecture can be solved in a simple way *via* the proper optimization of the methods used for the preparation of MOF-derived structures and the strategy for their interconnection.

Yang *et al.*[76] successfully designed a binder-free 3D hierarchical electrode material based on NiCoZn–S nanosheets coupled with granular $NiCo_2S_4$ nanowires, produced on carbon fiber cloths (CF@NiCoZn–S/$NiCo_2S_4$) by the hydrothermal sulfidation of a 2D-MOF-derived transition metal carbonate hydroxide (CF@NiCoZn–CH/NiCo–CH), as illustrated in Fig. 11A. The CF@NiCoZn–S/$NiCo_2S_4$ electrode delivered a performance of 194 mA h g^{-1} (corresponding to 698C g^{-1} or 1396 F g^{-1}) at 1 A g^{-1}, and retained 74.2% of this capacity at 10 A g^{-1} due to its unique hierarchical 1D-$NiCo_2S_4$ nanowire architecture (Fig. 11B and C) made of interconnected nanoparticles (Fig. 11D). This morphology exposed a higher density of active sites to the electrolyte, providing fast ion/electron transport. In addition, the 2D NiCoZn–S nanosheets with an even larger density of active sites, further enhanced the specific surface area and structural stability of the 3D CF electrode, providing excellent mechanical flexibility and structural orderliness, thus ensuring the superior performance of the NiCoZn– S/$NiCo_2S_4$ electrode.

The binder-free electrode strategy based on hierarchical MOF-derived materials was also explored by Yang *et al.*,[7] who grew granulated MOF nanosheets on carbon fibers that were subsequently converted into interconnected NiCo-alloy nanospheres that were finally sulfidated to produce NiCo-alloy@NiCo-sulfide core–shell nanoparticles (NiCo-alloy@$(NiCo)_9S_8$/CF) while keeping the original nanosheet arrays structure (Fig. 11E). The interconnected NiCo-alloy nanoparticles core provided efficient electron highways as demonstrated by the ultrahigh conductivity, whereas the $(NiCo)_9S_8$ shell with suitable thickness provided fast electrolyte diffusion and abundant effective electroactive sites, while preventing the oxidation of the alloyed nanoparticles (Fig. 11F and G). Due to these synergistic effects, the NiCo-alloy@$(NiCo)_9S_8$/ CF electrode delivered 213 mA h g^{-1} (or a specific capacitance of 1533.6 F g^{-1}) at 1 A g^{-1}, with a rate capability of 80.3% at 20 A g^{-1}, and a capacity retention of 86% after 5000 cycles.
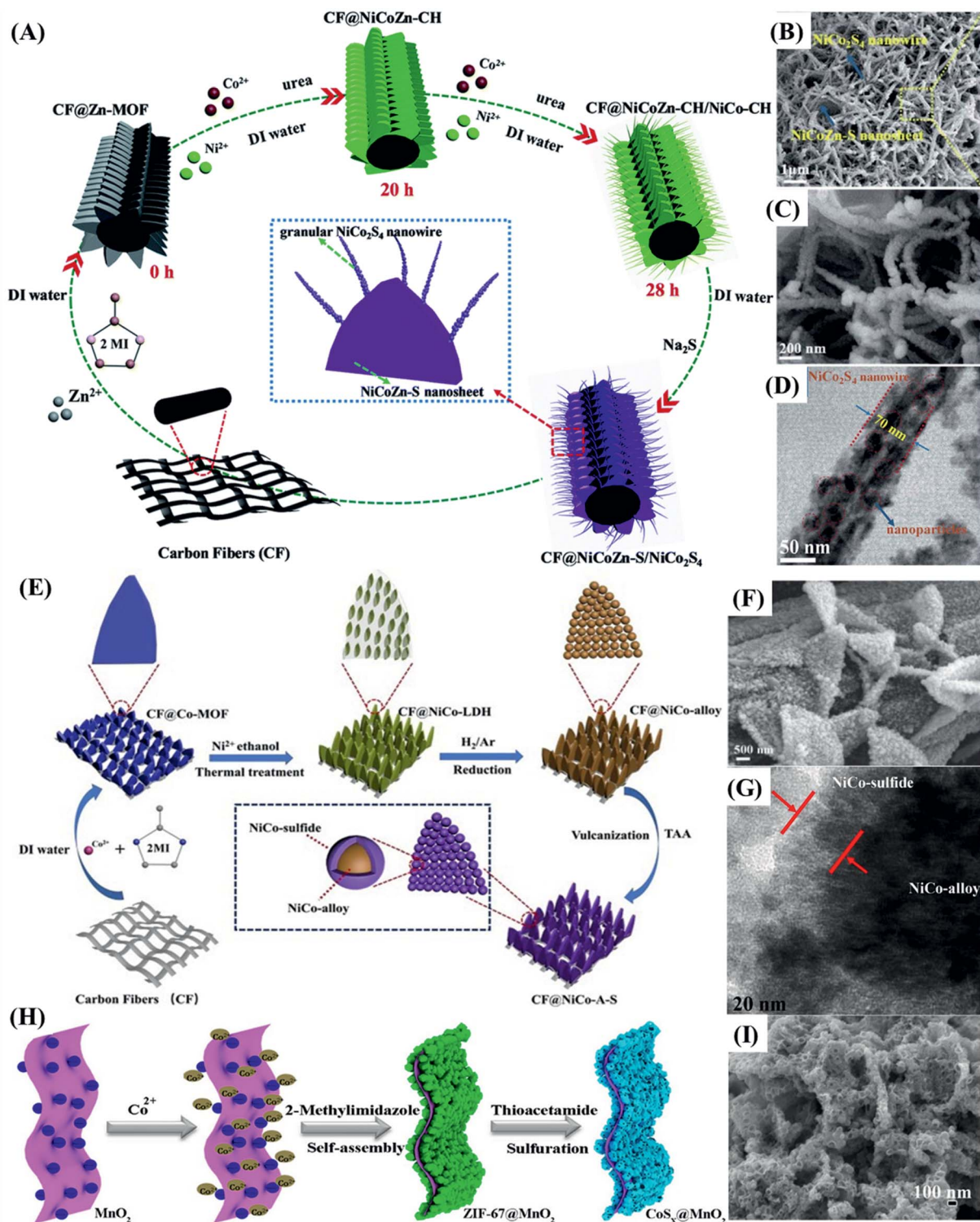
452 | *J. Mater. Chem. A*, 2022, **10**, 430–474

This journal is © The Royal Society of Chemistry 2022

Fig. 11 (A) Schematic showing the fabrication process of 3D hierarchical CF@NiCoZn–S/NiCo$_2$S$_4$ electrodes. (B, C) SEM and (D) TEM images of CF@NiCoZn–S/NiCo$_2$S$_4$ material at different magnifications. Reproduced with permission.[76] Copyright Marketplace™, Royal Society of Chemistry. (E) Scheme illustrating the fabrication of a NiCo-alloy@(NiCo)$_9$S$_8$/CF electrode. (F) SEM and (G) TEM images of CF@NiCo-A-S nanosheet arrays material. Reproduced with permission.[54] Copyright© 2019. Published by Elsevier B.V. (H) Scheme showing the synthesis of the CoS$_x$@MnO$_2$ material, and (I) its FESEM image. Reproduced with permission.[66] Copyright© 2017, American Chemical Society.

As discussed previously,[65] the surface of a negatively charged supporting material, rich in functional groups, can be spontaneously covered with Co^{2+} ions by electrostatic interactions, thus restraining the growth of MOF particles.[66] Therefore, Chen *et al.*[66] assembled a uniform network of small ZIF-67 nanocubes on the surface of MnO$_2$ ultrathin nanosheets, acting as

This journal is © The Royal Society of Chemistry 2022

J. Mater. Chem. A, 2022, **10**, 430–474 | **453**

a structure-directing agent, to form a sandwich-type structure ($ZIF\text{-}67@MnO_2$). This was subsequently transformed into hollow cobalt sulfide nanocages firmly anchored on both sides of the MnO_2 nanosheets ($CoS_x@MnO_2$) via a simple sulfidation process (Fig. 11H). Such 3D $CoS_x@MnO_2$ electrodes delivered 1635 F g^{-1} at 1 A g^{-1} with 71% rate capability at 10 A g^{-1} and 81% cycling stability after 5000 cycles, a performance significantly superior to that of pristine CoS_x electrodes (1013 F g^{-1} at 1 A g^{-1}). The structure of hierarchical 3D $CoS_x@MnO_2$ (Fig. 11I) was optimized to reduce the diffusion pathlength of electrolyte ions, in which the CoS_x hollow nanocages with ultrathin shells

offered a higher density of active sites and surface area, while the MnO_2 nanosheets improved the electrolyte diffusion and provided an interconnected network for charge transport.

More recently, layered double hydroxides (LDHs) have been extensively used as electrocatalysts, or electrodes in energy-storage devices, due to their unique lamellar structures exhibiting rapid ion transport channels, and the possibility of tuning the band gap energy and density of states, providing materials with high electrical conductivity.[6] The MOF-derived LDHs with multi-metallic structures presented higher electrical conductivity, improved ion diffusion efficiency, and reduced resistance

Fig. 12 (A) Scheme illustrating the synthesis of the hollow NiCo-LDH/Co$_9$S$_8$ hybrid. (B) Panoramic and single (inset) SEM images, and (C) TEM image (g) of NiCo-LDH/Co$_9$S$_8$ polyhedrons. (D) Optimized structures of NiCo-LDH/Co$_9$S$_8$ and (E) isolated Co$_9$S$_8$. Reproduced with permission.[6] Copyright© 2017 Wiley-VCH Verlag GmbH & Co. KGaA, Weinheim. (F) A schematic showing the fabrication process of the CC@NiCo-LDH/Co$_9$S$_8$ hybrid nanosheet arrays. (G–I) SEM images of the CC@NiCo-LDH/Co$_9$S$_8$ hybrid nanosheet arrays. (J) Schematic illustration displaying the merits of the hierarchical CC@NiCo-LDH/Co$_9$S$_8$ electrode for energy storage. Reproduced with permission.[53] Copyright© 2018. Published by Elsevier B.V. (L) Scheme illustrating the fabrication of the CF@NiCoZn-LDH/Co$_9$S$_8$-QD hybrid nanosheet arrays, and (M) its optimized structure. (N) SEM images of CF@NiCoZn-LDH/Co$_9$S$_8$-QD hybrid nanosheet arrays. Reproduced with permission.[67] Copyright© 2020 Wiley-VCH Verlag GmbH & Co. KGaA, Weinheim.

454 | *J. Mater. Chem. A*, 2022, **10**, 430–474

This journal is © The Royal Society of Chemistry 2022

at the interlayer regions. Among them, the trimetallic derivatives[67] and hollow structures[6,53] are especially suited as electrode materials and also as supporting materials for the deposition of other electroactive materials, such as transition metal sulfides. This procedure can be done using simple sulfidation methods to produce highly efficient hybrid electrode materials based on decorated trimetallic LDHs.[6,53,67]

Similar strategies can be used for the preparation of interesting new materials based on multi-metallic LDHs and Co_9S_8 by the selective sulfidation of Co-containing multi-metallic LDHs to induce the formation of Co_9S_8 nanoparticles. Notwithstanding the difficulties, Yang *et al.*[53] produced embedded Co_9S_8 nanoparticles, whereas Yang *et al.*[67] and Yilmaz *et al.*[6] produced interlayered Co_9S_8 nanoparticles. The synergistic effect of multi-metallic LDHs and interlayered Co_9S_8 resulted in high electrical conductivity, metallic-like conductivity, and significant electrolyte adsorption by van der Waals and hydrogen bond interactions.[53]

Yilmaz *et al.*[6] demonstrated the selective formation of interlayered Co_9S_8 by the sulfidation of MOF-derived hollow rhombic dodecahedron NiCo-LDHs to produce the NiCo-LDH/Co_9S_8 electrode material (Fig. 12A–C). From the optimized stoichiometry of the hybrid structure and isolated Co_9S_8 shown in Fig. 12D and E, the Co_9S_8 nanoparticles are likely very small (quantum dot-like dimensions), and can effectively enhance the structural stability and optimize the exposure of active sites for the redox reactions due to their extremely high surface area, although the authors did not mention it. The combination of tiny Co_9S_8 clusters with the NiCo-LDH system ensured the enhanced electron mobility throughout the structure by an electronic coupling and hopping mechanism involving a very high density of active sites. In addition, the NiCo-LDH/Co_9S_8 hybrid exhibited a H_2O chemisorption energy (absolute) of 0.87 eV, much higher than the individual components NiCo-LDH (0.24 eV) and Co_9S_8 (0.14 eV), which can further improve the overall electrolyte diffusion. All such features were reflected in the high capacitance of NiCo-LDH/Co_9S_8 of 1653 F g^{-1} at 4 A g^{-1}, with 62% and 95.4% capacitance retention respectively at 20 A g^{-1} and after 3000 cycles, which are quite high values for a monometallic sulfide-based electrode material.

Similar materials with different compositions and morphologies based on 2D LDH nanoarrays directly grown on conductive carbon materials (carbon cloth[67] and carbon fibers[53]) with binder-free tight contact, high surface area, and improved ion transport and redox reaction have also been realized. Yang *et al.*[53] embedded Co_9S_8 nanoparticles into hollow leaf-like NiCo-LDH nanoarrays directly grown on flexible carbon fibers (CC@NiCo-LDH/Co_9S_8) (Fig. 12F), exploring the hollow NiCo-LDH structure (Fig. 12G–I) to further reduce the ion diffusion resistance and increase the specific surface area (Fig. 12J). Likewise, Yang *et al.*[67] synthesized Co_9S_8 quantum dots (QDs) interlayered in NiCoZn-LDH nanosheets directly grown on carbon fibers (CF@NiCoZn-LDH/Co_9S_8-QD) (Fig. 12L and M), combining the benefits of trimetallic LDHs conductive support and ultrasmall electroactive nanoparticles (Fig. 12N). In this case, the high density of states of the trimetallic LDH ensured even higher electrical conductivity and ion-diffusion rates than

mono- or bimetallic LDH. The CC@NiCo-LDH/Co_9S_8 (ref. 53) electrode delivered 2850 F g^{-1} at 1 A g^{-1}, with 72.4% of rate capacity at 10 A g^{-1} and 92.6% capacitance retention after 5000 cycles, whereas CF@NiCoZn-LDH/Co_9S_8-QD[67] stayed behind with 2504 F g^{-1} at 1 A g^{-1}, and rate capacity of 62% at 20 A g^{-1}. Both electrodes presented extremely high performances, in comparison to monometallic sulfide-based electrodes. CC@NiCo-LDH/Co_9S_8 (ref. 53) gave the best performance, due to the many synergistic effects, and benefiting from the hollow bimetallic HDL with embedded cobalt sulfide nanoparticles[53] and trimetallic HDL hybrid structures with interlayered ultrasmall cobalt sulfide nanoparticles.[67]

In contrast, Sun *et al.*[75] based their work on the assumption that high electrical conductivity metal sulfides could be a suitable core material in core@shell heterostructures when coupled with a high pseudocapacitive shell material, especially in binder-free electrode architectures. Accordingly, they designed and fabricated a conductive scaffold of MOF-derived 2D Zn_x-Co_{1-x}S interconnected nanosheet arrays on CC, and electrodeposited and subsequently hydrothermally grew well-aligned 3D ultrathin $Ni(OH)_2$ nanoflakes and vanadium nitride (VN) to form core@shell binder-free electrodes (Fig. 13A). The specific capacitance of Zn_xCo_{1-x}S@$Ni(OH)_2$/CC (2730 F g^{-1} (8.1 F cm^{-2}) at 3 mA cm^{-2}) was nearly 1.3 and 2 times larger as compared to Zn_xCo_{x-1}O@$Ni(OH)_2$/CC and Zn_xCo_{1-x}S/CC electrodes. Also, its rate capability of 76.6% at 20 mA cm^{-2} and 87% capacitance retention after 10 000 cycles outperformed Zn_xCo_{1-x}S/CC and Zn_xCo_{x-1}O@$Ni(OH)_2$/CC. The 3D network architecture of interconnected and intersected Zn_xCo_{1-x}S@$Ni(OH)_2$ nanosheets (Fig. 13B–D) promoted the exposure of a larger electroactive surface area and facilitated ion and electron diffusion. On the other hand, the Zn_xCo_{1-x}S nanosheets core directly grown on CC enhanced the conductivity and buffered the strains caused by volume changes during the charge–discharge cycles, while the $Ni(OH)_2$ nanoflakes shell provided a high concentration of rapid reversible redox sites. Similarly, VN has recently been considered to be a promising material due to its high theoretical specific capacitance and energy density, as well as fast and reversible redox reactions. However, the weakly interconnected VN nanoparticles usually generate materials with poor mechanical stability that are unavoidably destroyed, or detached, during cycling. Nevertheless, the core@shell heterostructure exhibited reasonably good stability in comparison to the electrode prepared with pristine VN nanosheets, due to the presence of Zn_xCo_{1-x}S nanosheets efficiently buffering the volume changes during the charge–discharge processes. However, Zn_xCo_{1-x}S@VN/CC based on VN nanoparticles homogeneously distributed on top of Zn_xCo_{1-x}S nanosheets, exhibited the low capacitance of 1.35 F cm^{-2} at 3 mA cm^{-2}, which is twice as large as that of VN electrodes, with a rate capacity of 60% at 20 mA cm^{-2} and 80% of charge retention after 10 000 cycles. There is a long way to go to bring the performance of VN-based materials close to that of high-performance materials such as trimetallic LDHs and transition metal sulfides.

To facilitate the visualization of the eventual tendencies in the electrochemical performance of MOF-derived sulfides and
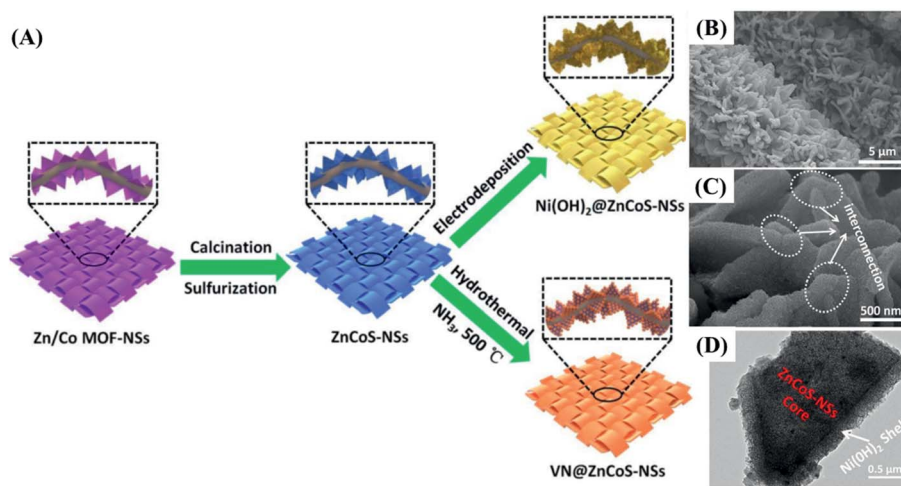
This journal is © The Royal Society of Chemistry 2022

J. Mater. Chem. A, 2022, **10**, 430–474 | **455**

Fig. 13 (A) Schematic illustration of the fabrication process of $Zn_xCo_{1-x}S@Ni(OH)_2/CC$ and $Zn_xCo_{1-x}S@VN/CC$ electrodes. (B) Low- and (C) high-magnification SEM. (D) TEM image of $Zn_xCo_{1-x}S@Ni(OH)_2/CC$. Reproduced with permission.[75] Copyright Marketplace™, Royal Society of Chemistry.

figure out the best preparation strategies, the electrodes with the top 10 highest specific capacitances are listed in Fig. 14. The best one is the binder-free $CNWAs@Ni@CoNi_2S_4/CC$ electrode (3163 F g^{-1} at 1 A g^{-1}),[56] which presented almost 1.7 times larger specific capacitance than the ninth-best one, the slurry-casted $CoNi_2S_4$ electrode (1890 F g^{-1} at 4 A g^{-1}).[77] Although they are based on the same nickel–cobalt sulfide nanoparticles, the deposition on nickel metal-covered CNWAs supported on carbon cloth plays a fundamental role in increasing the overall performance of the electrode, demonstrating the relevance of material design and nanostructure.

The tenth ($CoS_x@MnO_2$, 1720 F g^{-1} at 0.5 A g^{-1}),[66] eighth ($Zn_{0.76}Co_{0.24}S$-NC/CC, 2133.2 F g^{-1} at 1.25 A g^{-1}),[55] seventh (Ni–Zn–Co–S/NF, $2.343.9$ F g^{-1} at 10 mA cm^{-2})[68] and sixth ($NiCo_2S_4$/ACC, 2392 F g^{-1} at 1 A g^{-1})[60] materials with the best performances demonstrated that hollow nanostructures based on MOF-derived metal sulfides directly grown onto highly

conductive materials are key components of high-performance nanocomposites and hybrid electrode materials. In these strategies, the conducting substrate not only is a structure-directing agent with tight mechanical and electrical contact, but also significantly increases the electroactive surface area, overall stability, electrical conductivity, and ion-diffusion rates. Interestingly, due to their intrinsic similarities, the second (NiCo-LDH/Co_9S_8/CC, 2850 F g^{-1} at 1 A g^{-1})[62] and the fifth (CF@NiCoZn-LDH/Co_9S_8-QD, 2504 F g^{-1} at 1 A g^{-1})[67] best materials demonstrated the advantages of the selective sulfidation of Co-containing multi-metallic LDHs to produce binder-free electrodes with Co_8S_9 clusters in the interlayer space of multi-metallic LDHs. On the other hand, the third (Zn_xCo_{1-x}-S@Ni(OH)$_2$/CC) (2730 F g^{-1} at 3 mA cm^{-2})[75] and fourth (Co_3-S_4@FeCo$_2S_4$/NF, 2695 F g^{-1} at 1 A g^{-1})[57] best electrodes are both based on core@shell structures. The former exploiting the high specific capacitance of Ni(OH)$_2$ nanoflakes and high electrical conductivity of the interconnected $Zn_xCo_{1-x}S$ nanosheet arrays, whereas the latter takes advantage of the elevated ion-diffusion rates and faster electron transport provided by the hollow Co_3S_4 nanoparticles, in addition to the high specific capacitance and effective electroactive surface area of $FeCo_2S_4$ nanosheets.

In summary, MOF-derived sulfides can have their electrochemical performances enhanced further by exploring the synergic effects based on multi-metallic sulfides with highly conducting multivalence electroactive sites, associated with the high porosity and surface area inherited from the precursor MOF structures. Such a strategy relies on (a) hollow nanoparticles with superior ion and electron transport to optimize the availability of electroactive sites; (b) binder-free electrode architectures and reduced series resistance and "dead-mass" loading; (c) the preparation of nanocomposites and hybrid nanomaterials with intertwined and interconnected high conductivity structures; and (d) the preparation of core@shell heterostructures with highly conductive cores and electroactive shells to realize electrode materials with increasingly higher performances.
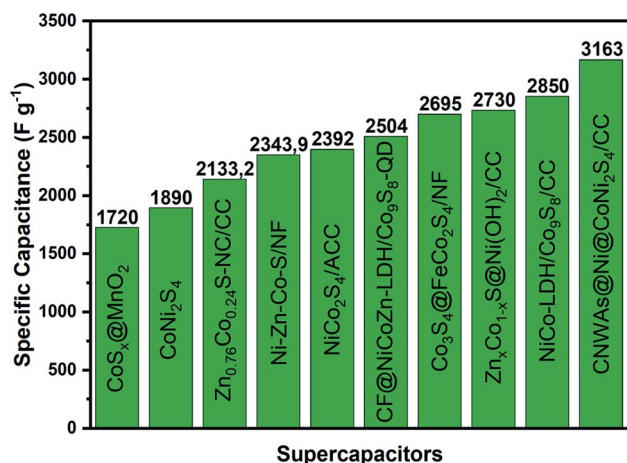

Fig. 14 A list of the MOF-derived sulfide electrode materials with the top 10 highest specific capacitances.

456 | *J. Mater. Chem. A*, 2022, **10**, 430–474

This journal is © The Royal Society of Chemistry 2022

5. MOF–derived metal sulfides as electrocatalysts for water-splitting

5.1. MOF-derived metal sulfides-based HER electrocatalysts

The performance of electrocatalysts is strongly dependent on parameters such as the surface area to expose and activate as many electrochemically active sites as possible, on account of the presence of interconnected channels and voids, and conducting components for efficient charge transport. These are the very same fundamental parameters considered previously in the case of electrode materials for supercapacitors. As such, there is the question of what is the key change that differentiates an electrode material from an electrocatalyst, which can be easily answered by considering the cytochromes, biomolecules enrolled in the electron transport chain coupled with oxidative phosphorylation and production of energy taking place in cells during respiration. Cytochrome-a, cytochrome-b, and cytochrome-c oxidase are all proteins containing iron protoporphyrin-IX (Fe-PPIX) as a prosthetic functional group. The first two act as electron relays while the last one is responsible for the catalytic reduction of dioxygen in water, a process involving four electrons and four protons. The two axial positions of Fe-PPIX in cytochrome-a and b are occupied by strongly bound ligands that define the Fe^{III}/Fe^{II} redox potential, whereas one of the axial positions of Fe-PPIX is open for the coordination and activation of an oxygen molecule. Thus, battery and supercapacitor electrode materials should be reversibly oxidized and reduced (charged/discharged) much like cytochrome-a and b, whereas cytochrome-c is a good example of an electrocatalyst. In this case, clearly, the electronic features leading to the bonding and consequent activation of the substrate, thus inducing its chemical transformation, is of the utmost relevance, but that cannot take place without, or is strongly limited by, the previously mentioned parameters. Accordingly, the efforts are all focused on finding materials that can be easily prepared and best account for all those requirements.

As highlighted previously, MOFs and materials derived from MOFs, are high-surface-area, electrochemically active materials possessing most of the ideal characteristics, and are being widely studied as electrocatalysts for water-splitting.[14,15,80,81] In this context, a thorough analysis of the role of MOF-derived sulfides should reveal eventual trends that can direct the search for even more efficient and robust electrocatalysts. The results summarized in Table 2 show that all electrocatalysts based on MOF-derived sulfides for HER contain cobalt, or were

Table 2 Performance parameters of recently reported MOF-derived metal sulfide-based HER electrocatalysts: overpotential at 10 mA cm^{-2}, Tafel slope, stability, and pH conditions[a]

Sulfide type	MOF-derived sulfide	Precursors	Method	Substrate	η_{10} (mV)	Tafel slope (mV dec^{-1})	Stability (h)	pH condition	Ref
Monometallic	WS$_2$/Co$_{1-x}$S@N,S co-doped porous carbon	PTA@ZIF-67	Sulfidation/carbonization	GCE	250	64	1000 cycles	0.5 M H$_2$SO$_4$	88
	CoS	Co-MOF	Calcination/hydrothermal sulfidation	CC	141	103	20	1 M KOH	82
	a-CoS$_x$	ZIF-67	Electrochemical conversion	FTO	168	76	20	(pH = 7) 1M PBS	83
	CoS@CoNi-LDH	Co-MOF	Calcination/hydrothermal sulfidation	CC	124	89	50	1 M KOH	82
	Co$_9$S$_8$	Co-MOF [(CH$_3$)$_2$NH$_2$][Co(HCOO)$_3$]	Solvothermal	GCE	272	107	500 cycles	0.5 M H$_2$SO$_4$	84
	CoS$_x$@MoS$_2$	Co-MOF [(CH$_3$)$_2$NH$_2$][Co(HCOO)$_3$]	Solvothermal/hydrothermal	GCE	239	103	500 cycles	0.5 M H$_2$SO$_4$	84
	CoS$_2$–MoS$_2$ HNAs	Co-MOF arrays	Etching of MOF/sulfidation	Ti foil	82	59	20	1 M KOH	85
	C/LDH/S	ZIF-67	Annealing/hydrothermal/sulfidation	NF	142	62	60	1 M KOH	6
	CoS	ZIF-67	Sulfidation	GCE	331	167	—	0.5 M H$_2$SO$_4$	87
	Porous Ag/Ag$_2$S-20	ZIF-67	Sulfidation/cation exchange	GCE	136	59	30	0.5 M H$_2$SO$_4$	87
Bimetallic	Ni–Co–S–340(60)	Ni–Co-BTC MOF	Solvothermal/calcination/sulfidation	GCE	129	96.1	22	1 M KOH	89
	CoS–MoS–Zn	BMOFs	Sulfidation/solvothermal	GCE	72.6	37.6	60	0.5 M H$_2$SO$_4$	86

[a] BMOFs = bimetallic (Co,Zn) organic frameworks; CC = carbon cloth; GCE = glassy carbon electrode; GC-RDE = glassy carbon rotating disk electrode; HNAs = heteronanosheet arrays; NF = nickel foam; WS$_2$/Co$_{1-x}$S@N,S co-doped porous carbon = bimetallic tungsten–cobalt sulfide-based heteroatom doped porous carbon.

This journal is © The Royal Society of Chemistry 2022

J. Mater. Chem. A, 2022, **10**, 430–474 | **457**

prepared from a precursor containing cobalt, and the incorporation of molybdenum significantly enhanced the electrocatalytic activity, indicating possible synergistic effects.

For example, K. Ao, Q. Wei, and W. A. Daoud[82] reported a calcination and hydrothermal sulfidation strategy to transform the Co-MOF nanorods (NRs) precursor deposited on carbon cloth (CC) directly into CoS NRs, as outlined in Fig. 15A. The CoS/CC electrocatalyst (Fig. 15B) presented an overpotential of 141 mV and a Tafel slope of 103 mV dec^{-1}. It is important to note that among the single-phase monometallic sulfides, CoS/CC showed superior electrocatalytic properties (especially in relation to the overpotential) as compared to several other MOF-derived sulfides, including amorphous cobalt sulfide (a-CoS$_x$, η_{10} = 168 mV and Tafel slope of 76 mV dec^{-1} (ref. 83)) and Co$_9$S$_8$ (η_{10} = 272 mV and Tafel slope of 107 mV dec^{-1} (ref. 84)), indicating the relevance of structural features to the electrocatalytic activity.

The strategy of using 3D sulfide NRs as scaffolds for the electrodeposition of LDHs (Fig. 15A) was demonstrated to be especially convenient since it can be carried out via a simple one-step electrodeposition method to generate heterostructured CoS@CoNi-LDH/CC electrodes, as shown in the SEM image of Fig. 15C. The combination of suitable structural and composition features led to remarkable HER electrocatalytic activity, as demonstrated by the low overpotential of 124 mV and a Tafel slope of only 89 mV dec^{-1}. The performance of this electrode is superior to that of the hybrid NiCo-LDH/Co$_9$S$_8$ hollow NPs derived from zeolitic imidazole frameworks (ZIFs) reported by Yilmaz et al.[6] (η_{10} = 142 mV and Tafel slope of 62 mV dec^{-1}). In addition, the overpotential of CoS@CoNi-LDH/CC increased by only 17 mV after 50 h of a continuous chronopotentiometry evaluation. These excellent electrocatalytic properties were assigned to the enhanced surface area and good electric contact with the conductive carbon microfibers, demonstrating that the combination of sulfides and hydroxides is a very promising strategy in the development of high-performance electrocatalysts for the HER.

Even better results have been obtained by combining different metal sulfides, especially upon the incorporation of Mo. For instance, Li and collaborators[85] prepared porous and hollow CoS$_2$–MoS$_2$ hetero-nanosheet arrays on Ti foil by a facile MOF-based strategy. More specifically, the controlled etching of MOF by MoO$_4^{2-}$ and in situ sulfidation resulted in a CoS$_2$–MoS$_2$ mixed sulfide with abundant heterointerfaces modulating the
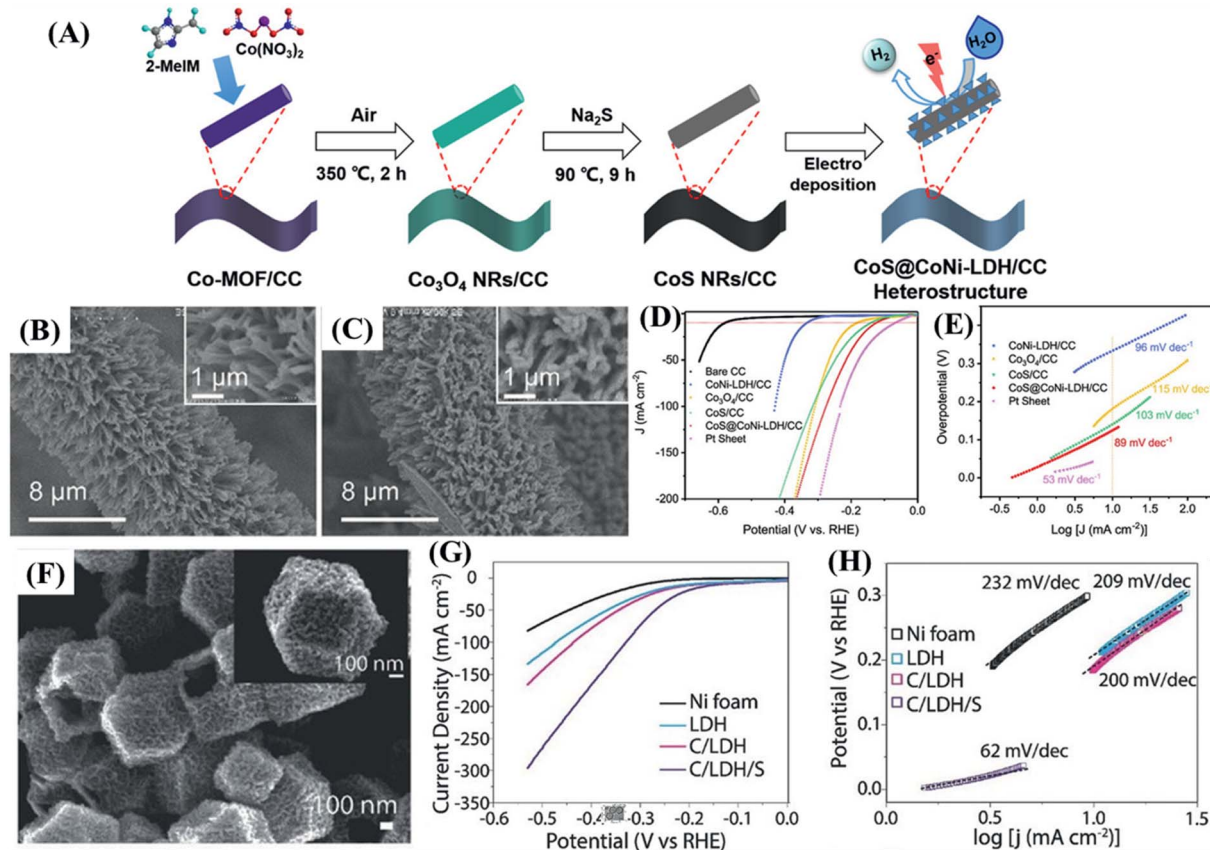

Fig. 15 (A) Scheme showing the synthesis of the heterostructured CoS/CC and CoS@CoNi-LDH/CC. SEM images of (B) CoS/CC and (C) CoS@CoNi-LDH/CC. HER performance. (D) Polarization curves of CC, CoNi-LDH/CC, Co$_3$O$_4$/CC, CoS/CC, CoS@CoNi-LDH/CC, and Pt sheet electrodes, and (E) the corresponding Tafel plots. Reproduced with permission.[82] Copyright© 2020 American Chemical Society. Panoramic and single-particle (inset) SEM images of (F) C/LDH/S polyhedrons. (G) HER polarization curves for nickel foam (Ni foam), LDH, C/LDH, and C/LDH/S electrodes at a scan rate of 5 mV s^{-1} and (H) the corresponding Tafel plots. Reproduced with permission.[6] Copyright© 2017 Wiley-VCH Verlag GmbH & Co. KGaA, Weinheim.
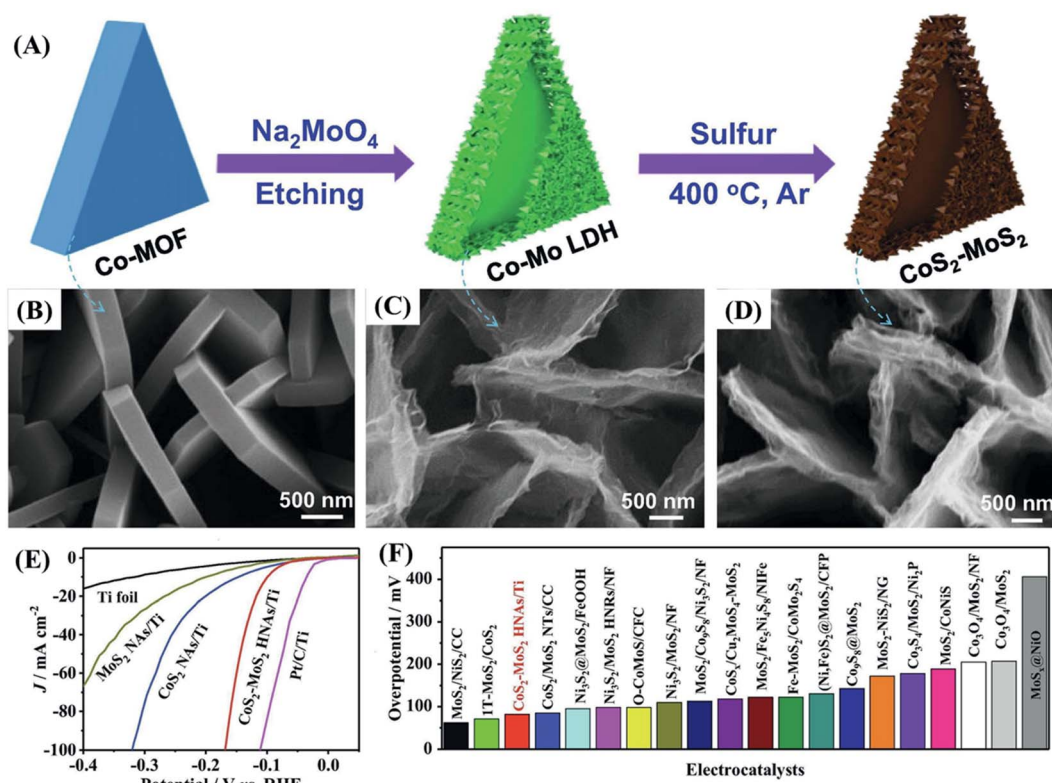
Fig. 16 Structural characterization of the CoS_2-MoS_2 HNAs/Ti electrode. (A) Schematic illustration of the synthesis of CoS_2-MoS_2 HNAs/Ti. SEM images of (B) Co-MOF NAs/Ti, (C) CoMo-LDH NAs/Ti, and (D) CoS_2-MoS_2 HNAs/Ti electrodes. HER performance of CoS_2-MoS_2 HNAs/Ti, and (E) comparative linear sweep voltammetry curves of the electrodes. (F) Overpotentials at 10 mA cm^{-2} for CoS_2-MoS_2 HNAs/Ti in comparison with recently reported excellent MoS_2-based HER catalysts. Reproduced with permission.[85] Copyright© 2020 Science Press and Dalian Institute of Chemical Physics, Chinese Academy of Sciences. Published by Elsevier B.V. and Science Press. All rights reserved.

local charge distribution, as outlined in Fig. 16A–D. The engineered CoS_2-MoS_2 heterostructure exhibited a low overpotential and Tafel slope for the HER of 82 mV and only 59 mV dec^{-1}, respectively (Fig. 16E), superior to that of MOF-derived hollow $CoS_x@MoS_2$ microcubes[84] (η_{10} = 239 mV and Tafel slope = 103 mV dec^{-1}, in 0.5 M H_2SO_4) and many other molybdenum-containing electrocatalysts (Fig. 16F). This excellent result was attributed to three main factors. (a) The well-exposed heterogeneous interfaces of CoS_2 and MoS_2 regulate the local charge distribution, dramatically lowering the kinetic barriers. (b) The hollow porous nanostructure allows fast electrolyte diffusion and high exposure of the surface electrochemically active sites. (c) The excellent adhesion and electric contact of the nanoarrays with the titanium foil generating stable binder-free electrodes exhibiting good electric conductivity and charge transfer capability.[85] This study demonstrated valuable insights for the development of MOF-derived heterogeneous electrocatalysts with tailored interface/surface morphologies for application in electrocatalysis.[85]

In addition to the preparation strategy of Co/Mo sulfides derived from MOFs, Yilmaz *et al.*[86] demonstrated an all-inclusive extrinsic morphological and intrinsic molecular topological *in situ* reconstruction of Zn–N coordinated Co–Mo disulfide (MoS–CoS–Zn, Fig. 17C and D) from structure-directing bimetallic CoZn-MOF (Fig. 17B), to generate specific heteroatomic

coordination sites and surface ligand functionalization, as outlined in Fig. 17A. Notably, MoS–CoS–Zn exhibited superior electrochemical activity toward the HER with an overpotential of 72.6 mV (*vs.* RHE) at 10 mA cm^{-2} (Fig. 17E) and a Tafel slope as low as 37.6 mV dec^{-1} (Fig. 17F), which is 61.4 mV lower than that of MoS–CoS (Fig. 17G). Comprehensive experimental spectroscopic studies and computational density functional theory (DFT) calculations revealed that the rationally designed electron-rich centers warrant efficient charge injection into the inert MoS_2 basal planes, augmenting the electronic density of inactive sites. Accordingly, the cooperative electrocatalytic activity can be tuned by (i) heteroatom doping and (ii) surface functionalization, opening new perspectives for the design of high-performance molybdenum disulfide-based HER electrocatalysts *via in situ* structural design and functionalization.

At this point, it is important to mention that so far all reported electrocatalysts are based on Co-containing MOF-derived sulfides, but can be modified to obtain even more efficient HER electrocatalysts. For instance, Xu *et al.*[87] developed a non-equivalent cation exchange strategy for the rational design and controlled synthesis of a porous Ag/Ag_2S heterostructure based on the rapid cation exchange by the MOF-derived CoS with lattice strain and abundant S-vacancies (Fig. 18A–D). This is made possible by the coordination loss and *in situ* epitaxial growth of metallic Ag, whose pore sizes and pore volumes can
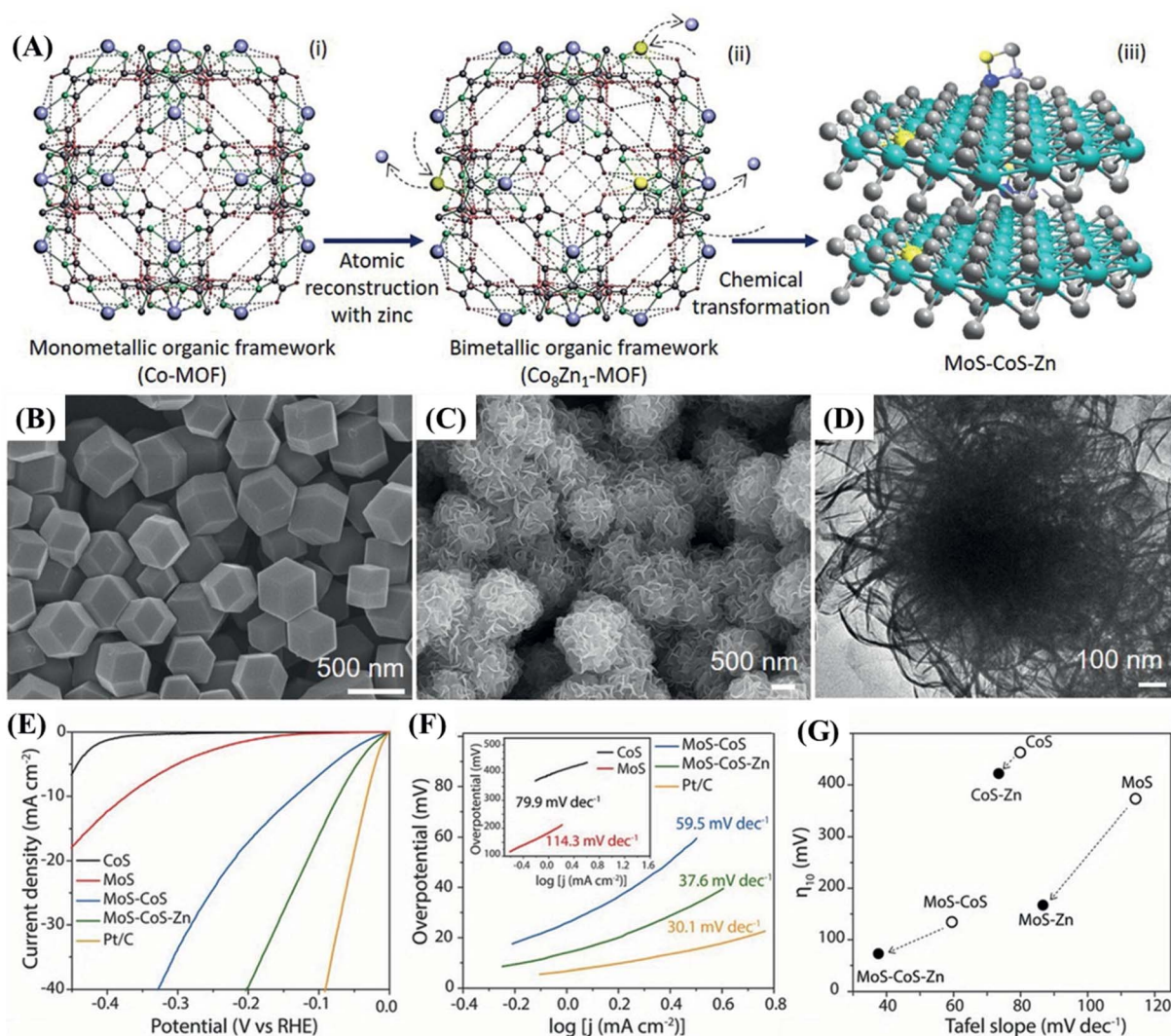
This journal is © The Royal Society of Chemistry 2022

J. Mater. Chem. A, 2022, **10**, 430–474 | **459**

Fig. 17 Scheme summarizing the conversion of (i) the monometallic organic framework (Co-MOF) into (ii) the bimetallic organic framework (Co_8Zn_1-MOF), and then to (iii) the MoS−CoS−Zn cobalt−molybdenum disulfide material. ((i) and (ii)) Purple, yellow, green, dark grey, and red spheres represent Co, Zn, N, C, and H, respectively. In the MoS−CoS−Zn crystal structure ((iii)), green, grey, yellow, dark blue, and purple spheres represent Mo, S, Zn, N, and Co atoms, respectively. (B) SEM image of the bimetallic organic framework (Co_8Zn_1-MOF). (C) SEM and (D) TEM images of MoS−CoS−Zn material. Electrochemical characterization of the HER electrocatalytic performance of CoS, MoS, MoS−CoS, and MoS−CoS−Zn. (E) HER polarization curves of CoS, MoS, MoS−CoS, MoS−CoS−Zn, and Pt/C recorded at a scan rate of 5 mV s^{-1} in 0.5 m H_2SO_4; (F) the corresponding Tafel plots. (G) Overpotentials at a current density of −10 mA cm^{-2} as a function of the Tafel slopes for pristine (CoS, MoS, and MoS−CoS) and Zn-coordinated (CoS−Zn, MoS−Zn, and MoS−CoS−Zn) electrocatalysts. Reproduced with permission.[86] Copyright© 2019 National University of Singapore. Published by Wiley-VCH Verlag GmbH & Co. KGaA, Weinheim.

be easily tuned. As a result, the Ag/Ag$_2$S catalyst required an overpotential of 136 mV to afford the current density of −10 mA cm^{-2}, and a low Tafel slope of 59 mV dec^{-1}, which is significantly much lower than the pristine CoS (η_{10} = Tafel slope = 167 mV dec^{-1}). According to the authors, metallic Ag uniformly dispersed on the surface of Ag$_2$S clusters and coupled with Ag$_2$S matrix can act as a good electron conductor, whereas the abundant S-vacancies caused by the lattice mismatch create more active sites and decrease the free energy for hydrogen adsorption (ΔG_H), thus enhancing the HER (Fig. 18E). As shown in the HRTEM image (Fig. 18F), the 3D porous Ag/Ag$_2$S heterostructure generated a corrugated morphology with compression strain that aggravated the lattice distortion and created

more vacancy sites (Fig. 18G), such that the defects induced by missing atoms can be clearly observed (Fig. 18H and I). More importantly, the ability to readily fine-tune the pore size of the Ag/Ag$_2$S heterostructure by changing the initial Ag$^+$ concentration provides a convenient way to induce lattice strains and S-vacancies simultaneously, which is fundamental for the optimization of the HER activity.

5.2. MOF-derived metal sulfides as OER electrocatalysts for water-splitting

The water-splitting reaction is one of the most promising renewable energy technologies, especially when coupled with

460 | J. Mater. Chem. A, 2022, 10, 430–474

This journal is © The Royal Society of Chemistry 2022

hydrogen fuel cells, thus closing the cycle. It is constituted by two semi-reactions, the reduction process leading to the evolution of hydrogen gas, as discussed in the previous section, and the oxidation process leading to the evolution of dioxygen gas. This reaction is especially challenging not only due to its tetraelectronic nature, but also given the release of four protons, imposing a quite high kinetic barrier. This sluggish reaction tends to limit the overall water-splitting reaction rate unless a quite high overpotential is provided[90] or efficient and robust electrocatalysts are used. In this context, the MOF-derived sulfides have demonstrated high prospects as electrode materials, given the excellent electrochemical and electrocatalytic properties towards the OER, which are frequently much better than achieved with standard materials based on noble metals such as Ir and Ru but using more abundant first-row transition metals.
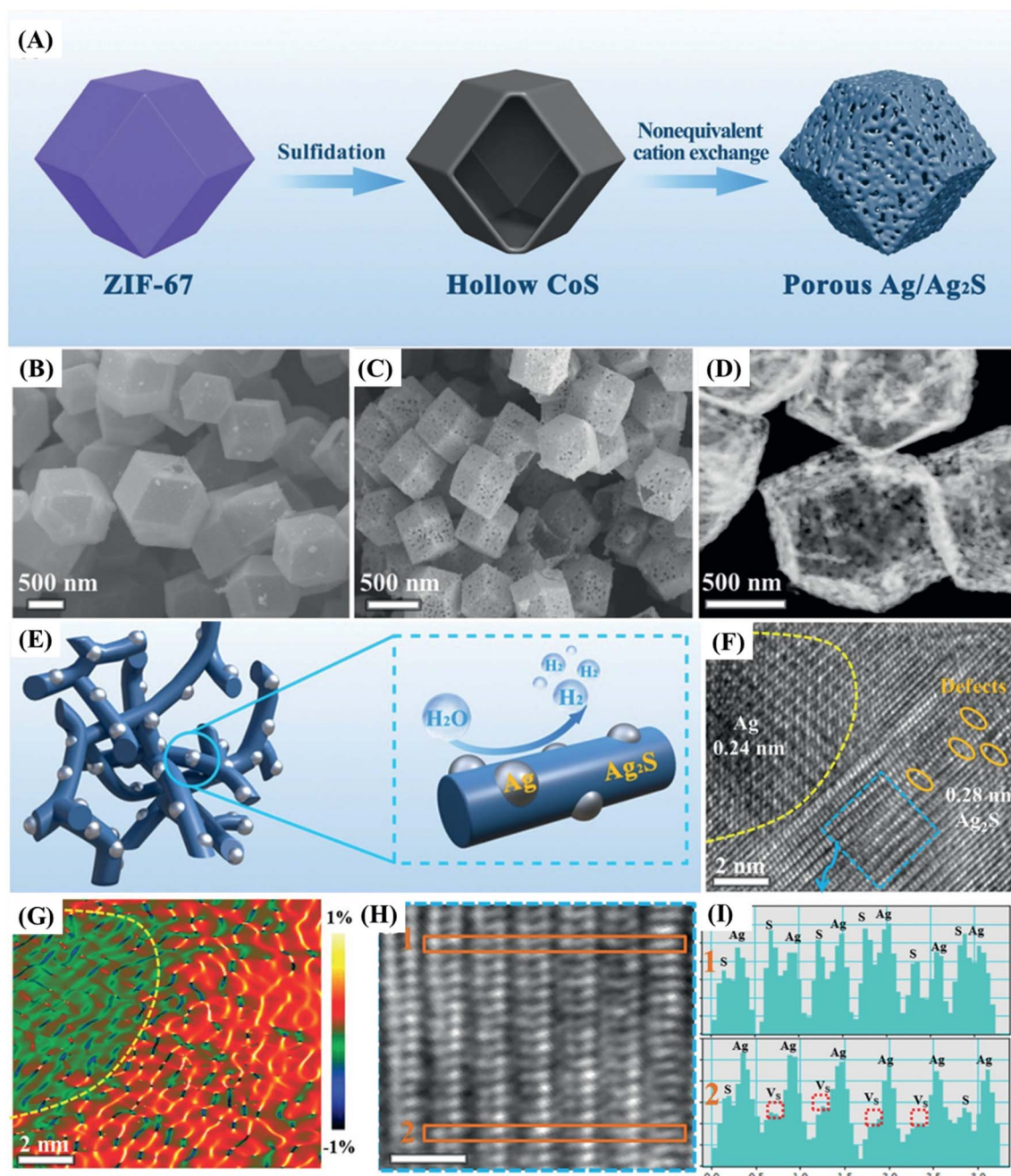

Fig. 18 (A) Scheme depicting the fabrication process of porous Ag/Ag$_2$S. SEM images of (B) the CoS precursor and (C, D) Ag/Ag$_2$S. (E) Schematic illustration of Ag/Ag$_2$S heterostructures, demonstrating the role of metallic Ag and Ag$_2$S clusters. (F) HRTEM image of Ag/Ag$_2$S. (G) The strain tensor map generated from the HRTEM image using geometric phase analysis. (H) HAADF–STEM image of Ag/Ag$_2$S. (I) A comparison of the strain intensity profiles along selected rectangular regions indicates the missed surface S atoms in Ag/Ag$_2$S. Scale bar, 0.5 nm. Reproduced with permission.[87] Copyright© 2021 Wiley-VCH GmbH.

This journal is © The Royal Society of Chemistry 2022

J. Mater. Chem. A, 2022, 10, 430–474 | 461

The cobalt sulfides are among the most extensively studied OER electrocatalysts, especially those prepared from ZIF-67 as the precursor. For example, Sun *et al.* successfully prepared the Co_9S_8/GN nanocomposite by subjecting a mixture of ZIF-67, graphene, and thioacetamide to a solvothermal process, followed by calcination. In this way, they combined the catalytic activity of cobalt sulfide NPs with the high electric conductivity and the excellent mechanical properties of graphene to generate a material with 450 mV of overpotential for the OER, lower than that of commercial Ir/C (570 mV). Similar results were achieved with a $Co_xS_y@C$ core@shell material obtained upon pyrolysis of ZIF-67 in a H_2S atmosphere, which presented $\eta_{10} = 470$ mV,[91] and a Co_9S_8/NSCNF electrode (η_{10} de 302 mV)[92] prepared by the deposition of cobalt sulfide on carbon nanofibers doped with sulfur and nitrogen, previously generated by the pyrolysis of a CdS@ZIF core@shell material.

Similarly, He *et al.*[93] prepared a $Co_3O_4@C$ material by calcination of a ZIF-67 precursor and reacted it with a Na_2S solution to get amorphous $CoS_x@C$ that was converted into the Co_{1-x}-S@C catalyst upon heat treatment in an argon atmosphere. Here, it is important to emphasize the need for fine control of the calcination temperature to obtain the desired materials, especially in the last heat treatment process, as depicted in the SEM micrographs of the materials obtained upon calcination of amorphous $CoS_x@C$ at 350, 400, and 450 °C (Fig. 19).

The combined analysis of the SEM images (Fig. 19A–C) and the DRX patterns (Fig. 19D) indicated that 350 °C is not enough to promote proper crystallization, while 450 °C is too high and converts the material into another cobalt sulfide material. Accordingly, 400 °C is the optimal processing temperature to obtain the desired porous dodecahedral structures exhibiting high electrocatalytic activity. This material presented the lowest η_{10} of 260 mV, as indicated by the dotted and dashed line in Fig. 19E, and the lowest Tafel slope of 85 mV dec^{-1}

(Fig. 19F), as expected for the most efficient OER electrocatalyst among them.

Among the preparation methods, those that can be carried out in a simple way, in a few steps, while allowing good control of the materials' properties are the most appealing, especially when considering the eventual large-scale commercial production. In this context, Du and collaborators used a cobalt MOF, denoted as Co-NSOMOF, a material containing oxygen, nitrogen, and sulfur in its structure, to prepare in a single pyrolysis step, the $(Co/Co_9S_8@NSOC)$ material[94] constituted by Co/Co_9S_8 nanoparticles encapsulated in a N, S, and O ternary-doped carbon matrix. This material exhibited a η_{10} of 373 mV that increased to 475 mV at a current density of 50 mA cm^{-2}, in comparison with 344 mV and 475 mV for RuO_2, indicating a better OER electrocatalytic performance at larger current densities. Such a good result was assigned to the synergistic effect of the cobalt sulfide and cobalt metal nanoparticles with the doped carbon, as well as the core@shell nanostructure preventing the migration and aggregation of those nanoparticles. The suitability and stability of such a nanomaterial were confirmed after a 10 h test carried out with $Co/Co_9S_8@$-NSOC, and 80 h test with $Co_{1-x}S@C$,[93] under operation conditions where only a small shift in overpotential was observed.

The relevance of the pyrolysis conditions was demonstrated but as expected, the structure and composition of the MOF precursors also played a fundamental role in defining the electrocatalytic properties. Liu *et al.*[72] investigated the effect of solvent viscosity in the preparation of the $[Co(Tdc)(Bpy)]_n$ precursor, where Tdc is thiophene-2,5-dicarboxylate and Bpy is 4,4'-bipyridine, using water and ethylene glycol as solvent, as shown in Fig. 20A. Both products were crystalline but exhibited contrasting DRX profiles (Fig. 20B) as well as morphologies. The material prepared in aqueous solution yielded large irregularly shaped crystals of up to a hundred micrometers, denoted

Fig. 19 SEM images of an amorphous $CoS_x@C$ sample calcined at (a) 350 °C, (b) 400 °C and (c) 450 °C, and the respective (d) XRD patterns, (e) *iR*-compensated LSV polarization curves and (f) Tafel plots. Reproduced with permission.[93] Copyright© 2018. Published by Elsevier B.V. on behalf of the Chinese Chemical Society and the Institute of Materia Medica, Chinese Academy of Medical Sciences.

462 | *J. Mater. Chem. A*, 2022, **10**, 430–474

This journal is © The Royal Society of Chemistry 2022

[Co(Tdc)(Bpy)]$_n$-*bulk* (Fig. 20C), probably as a consequence of aggregation, whereas well-formed large rectangular cuboid structures of a few micrometers were produced in more viscous ethylene glycol (Fig. 20D) as expected for a lower degree of agglomeration during the reaction.

The materials obtained upon pyrolysis, denoted as Co$_9$S$_8$@-SNCB (*bulk*) and Co$_9$S$_8$@SNCC (*cuboid*), retained the morphology of the respective precursors and respectively delivered η_{10} and Tafel slope of 420 mV and 129 mV dec^{-1}, and 330 mV and 80 mV dec^{-1} (Fig. 20E and F). The better performance of the cuboid derivative was attributed to the larger surface area provided by the graphitic structure of the carbon material, associated with the predominance of a mesoporous structure with higher pore volume, thus providing good stability (Fig. 20G) and suitable ion diffusion properties and contact with the electrocatalytic active sites.

Analogous to the cobalt-based materials, MOF-derived nickel sulfides also have been extensively explored as OER electrocatalysts. For example, Yang and coworkers prepared a core@-shell nickel sulfide, covered up with a N and S-doped carbon structure (NiS@N/S–C),[95] by the thermal decomposition of a nickel complex with vinylthiosemicarbazone. This material

presented a relatively large η_{10} of 417 mV, but is associated with a very low Tafel slope of 48 mV dec^{-1}, indicating fast electron diffusion and reaction kinetics. Such a high conductivity was attributed to the electronic structure of the doped carbon-containing N-pyridine, N-pyrrole, and S-thiophene sites that provide a suitable coordination environment for the metal ions to enhance their electrocatalytic properties.

Another interesting nickel-based material is the NGO/Ni$_7$S$_6$ produced by the solvothermal reaction of a nanoporous N-doped graphene oxide and MOF-74 (NGO/MOF-74) with thiourea, in a mixture of methanol (50 mL) and water (5 mL), at 200 °C, which delivered a η_{10} of 380 mV and a very low Tafel slope of 45.4 mV.[96] On the other hand, Lin *et al.*[97] prepared nickel sulfide alloyed with nickel–metal nanoparticles, based on the same strategy used to get the Co/Co$_9$S$_8$@NSOC composite.[94] The precursor was obtained by the reaction of NiSO$_4$ and 4,4'-bipyridine, using pyridine to block the free surface sites and control the growth of the crystals, and pyrolyzed to produce nickel sulfide/nickel metal nanoparticles covered by a graphene shell (Ni–Ni$_3$S$_2$@carbon) directly on N-doped carbon nanoplates, as shown in Fig. 21A. This Ni–Ni$_3$S$_2$@carbon catalyst presented an overpotential at 10 mA cm^2 of 284.7 mV and Tafel
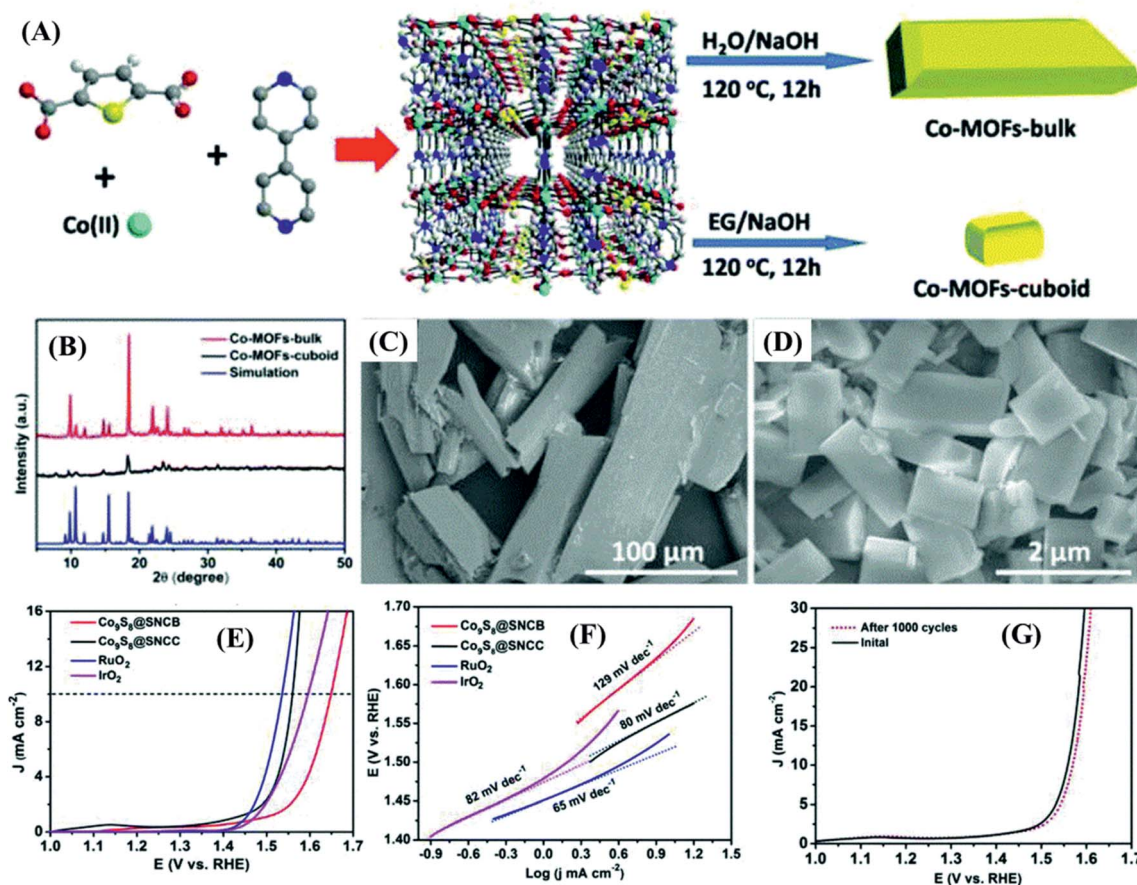

Fig. 20 (A) Schematic illustration of the preparation process of Co-MOF crystals in water and ethylene glycol as solvents. (B) XRD patterns of Co-MOFs-bulk and Co-MOFs-cuboid, and the respective (C) and (D) SEM images. (E) OER current densities of Co$_9$S$_8$@SNCC, Co$_9$S$_8$@SNCB, and RuO$_2$ electrodes in 0.1 M KOH solution, at a scan rate of 10 mV s^{-1}, and respective (F) Tafel plots. (G) Polarization curves for the Co$_9$S$_8$@SNCC electrocatalyst before and after 1000 cycles. Reproduced from ref. 72 with permission. Copyright Marketplace™, Royal Society of Chemistry.
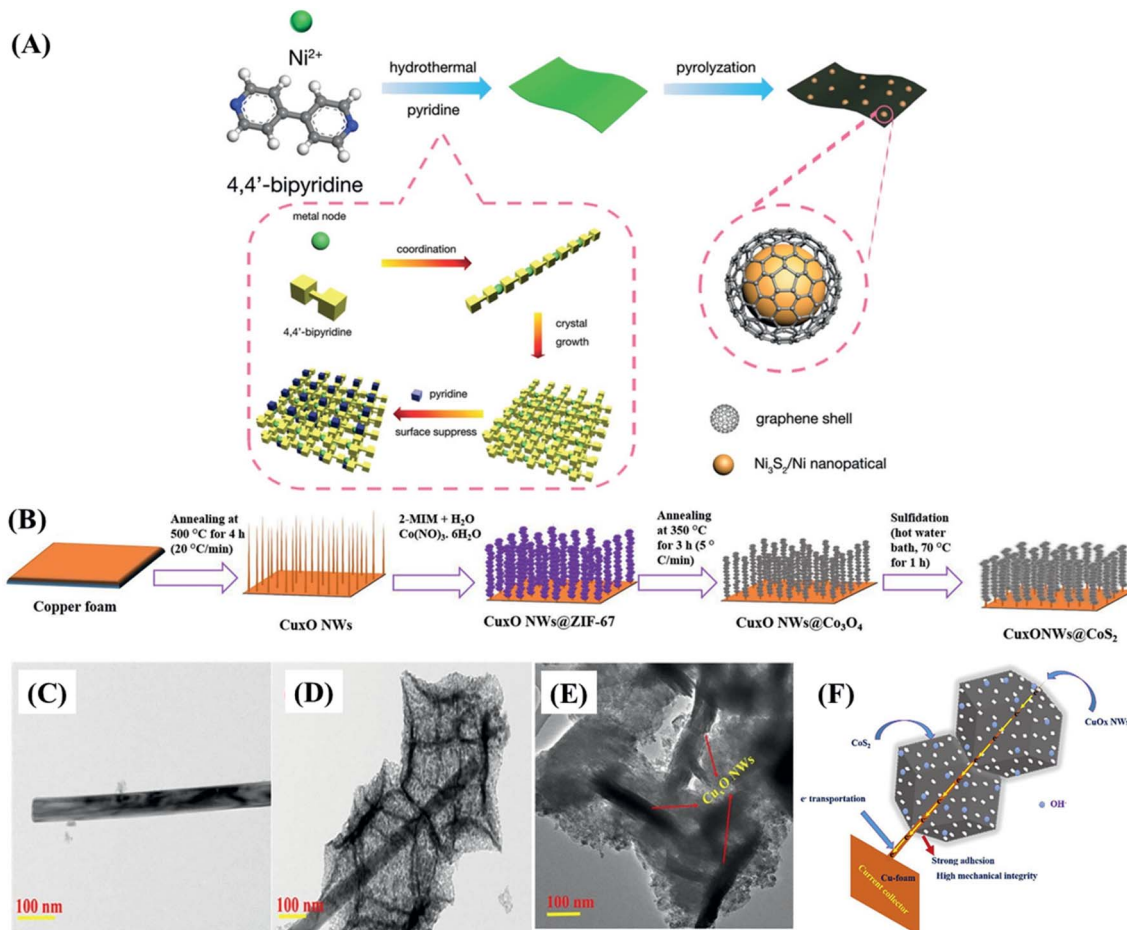
This journal is © The Royal Society of Chemistry 2022

J. Mater. Chem. A, 2022, **10**, 430–474 | **463**

Fig. 21 (A) Scheme illustrating the preparation of Ni–Ni$_3$S$_2$@carbon on N-doped 2D carbon nanoplates by pyrolysis of a Ni-based MOF precursor. Reproduced with permission.[97] Copyright© 2019 Wiley-VCH Verlag GmbH & Co. KGaA, Weinheim. Scheme depicting (B) the synthetic protocol and the TEM images of (C) pristine Cu$_x$O NWs, (D) Cu$_x$O NW@Co$_3$O$_4$, and (E) Cu$_x$O NW@CoS$_2$. (F) Scheme showing the adhesion of this nanocomposite to the Cu-foam, ensuring the mechanical stability and conductivity of the Cu$_x$O NW@CoS$_2$ electrode. Reproduced with permission.[98] Copyright© 2020 Elsevier B.V. All rights reserved.

slope equal to 56 mV dec^{-1}, making it an even better OER catalyst than other nickel-based composites discussed up to this point. The authors attributed such a good performance to the interactions of different crystalline phases of Ni and Ni$_3$S$_2$, promoting the enhancement of charge-transfer interactions and suggesting the important role played by metallic Ni in the composite.[97]

The possibility of employing MOF precursors incorporating strategic heteroatoms to reduce the number of steps, thus simplifying the preparation of the electrocatalyst, is very appealing and has been frequently explored. For example, Lin *et al.* prepared the Ni–Ni$_3$S$_2$@carbon electrocatalyst in a process of "self-sulfurization" by using a NiSO$_4$ Ni-MOF-based precursor whose residual anion SO$_4^{2-}$ was used as an internal sulfur source upon reduction to S^{2-}. It is interesting to note that while other MOF-based sulfides with an inner sulfur source used sulfur-containing MOFs, having S atoms as part of the MOF structure (as in Co/Co$_9$S$_8$@NSOC fabrication), in contrast, the Ni–Ni$_3$S$_2$@carbon case where the inner sulfur source was the counter anion in the Ni-MOF synthesis, is an alternative strategy for the preparation of MOF-derived sulfides.

In addition to the nanocomposites and nanostructures combining transition metal sulfides with carbon materials, electrocatalysts incorporating metal oxides into metal sulfides have also been developed in an attempt to improve their performance. In this context, Xu *et al.*[99] combined cobalt sulfide, prepared by the reaction of ZIF-67 with thioacetamide, with cerium oxide obtain CeO$_x$/CoS, a material presenting a low η_{10} overpotential of 269 mV and a Tafel slope of 50 mV dec^{-1}. Such a good OER performance was assigned to a fast oxygen gas diffusion through the oxygen vacancies in the cerium oxide structure, induced by the flipping of the cerium ions between the Ce^{3+} and Ce^{4+} oxidation states. Furthermore, the presence of CeO$_x$ in the structure decreased the surface energy for the formation of the Co–OOH activated complex and inhibited the oxidation of the material, thus increasing the Co^{2+}/Co^{3+} molar ratio (especially for the induced defects), which contributed to increase the stability of the electrocatalyst.

Prasad Ojha and collaborators[98] employed a similar strategy to prepare the CuO$_x$ NWs@CoS$_2$ catalyst as depicted in Fig. 21B. Copper oxide nanowires (CuO$_x$ NWs, Fig. 21C) were grown on copper foam by a vapor-solid phase process (the as-dried copper

464 | *J. Mater. Chem. A*, 2022, **10**, 430–474

This journal is © The Royal Society of Chemistry 2022

foam was subjected to annealing at 500 °C for 4 h to form Cu_2O, the precursor of CuO as the major product). The resultant material was immersed in a reaction medium for the deposition of ZIF-67, generating the CuO_x NWs@ZIF-67 core@shell material that was subsequently annealed to convert it into Cu_xO NW@Co_3O_4 (Fig. 21D), which was reacted with thioacetamide to obtain the desired Cu_xO NW@CoS_2 nanocomposite material (Fig. 21E). The CuO_x NWs play two fundamental roles in this material: (a) they are the support for the deposition of CoS_2, improving the electric contact with the copper foam while increasing the specific electroactive surface area, and (b) enhancing the conductivity and charge-transfer rate induced by the difference in the electronegativity of the O^{2-} and S^{2-} ions (Fig. 21F). This strategy generated a material with η_{10} of 210 mA cm^{-2} and a Tafel slope of 180 mV dec^{-2}.

Sulfides derived from MOFs are quite versatile materials and can be easily combined with other metal sulfides to enhance their electrocatalytic properties. The synergic properties obtained from the interaction of cobalt sulfide with MoS_2 were explored by Yang and collaborators[84] to produce hollow CoS_x@MoS_2 microcubes based on a three-step process. The $[(CH_3)_2NH_2][Co(HCOO)_3]$ Co-MOF was prepared and reacted with thioacetamide under solvothermal conditions to produce C_9S_8 hollow microcubes, which were reacted with Na_2MoO_4 and thiourea to produce the electrocatalytic material. The incorporation of electrocatalytically inactive MoS_2 into cobalt sulfide enhanced the surface area and diminished the diffusion length of ions and electrons in the CoS_x@MoS_2 composite (η_{10} =347 mV and Tafel slope = 147 mV dec^{-1}), which presented slightly better electrocatalytic properties than the Co_9S_8 hollow microcubes (η_{10} = 378 mV and Tafel slope = 157 mV dec^{-1}), but can be improved by incorporation of RuO_2.

A much better result was achieved by Li *et al.*,[85] who first deposited a layer of cobalt MOF and 2-methylimidazole on titanium sheets, which was reacted with Na_2MoO_4 solution to get Co-MOF arrays. This was heated with sulfur at 400 °C under N_2 flux, to get CoS_2–MoS_2 hetero-nanosheet arrays on Ti, denoted CoS_2–MoS_2HNAs/Ti, as shown in Fig. 16. This material exhibited good stability for 24 h and a η_{10} = 266 mV, an overpotential lower than that measured for materials such as IrO_2/Ti (310 mV), CoS_2NAs/Ti (330 mV), and MoS_2/Ti (364 mV) for the OER. Furthermore, the electrode kinetics for the OER was significantly improved, resulting in a Tafel slope of 104 mV dec^{-1}, similar to that of IrO_2/Ti (105 mV dec^{-1}), and consistent with the charge-transfer resistance as low as 17.6 Ω measured by electrochemical impedance spectroscopy, and lower than that for CoS_2HNAs/Ti (25.1 Ω) and MoS_2/Ti (33.2 Ω).

A similar strategy was used to prepare WS_2/Co_{1-x}S/N, the S-co-doped porous carbon nanocomposite by reacting ZIF-67 with phosphotungstic acid (PTA) at 600, 800, and 1000 °C, under H_2S atmosphere.[88] The best result was obtained when the material was processed at the highest temperature due to the formation of carbon with a high concentration of defect sites modulating the electronic and surface properties, thus changing the adsorption energy for the formation of the activated complex. There was also an increase in the surface area associated with a topological change facilitating the

detachment of the oxygen gas bubbles, improving the access to and performance of the metal sulfides electrocatalytic active sites. Thus, the WS_2/Co_{1-x}S/N electrode was more active (η_{10} = 365 mV; Tafel slope = 53 mV dec^{-1}) than the material prepared only with ZIF-67 (η_{10} = 396 mV; Tafel slope = 70 mV dec^{-1}) and the commercial IrO_2 catalyst (η_{10} = 417 mV; Tafel slope = 54 mV dec^{-1}). The incorporation of W into cobalt sulfide was beneficial due to the strong electron transfer between Co and W through the S-atoms of the Co_{1-x}S-WS_2 phase.

Despite the many possibilities for the combination of metal ions, bimetallic Ni–Co has been one of the most successful in the preparation of OER electrocatalysts exhibiting synergic effects.[100–102] For example, polyhedric cobalt and nickel sulfide on N-doped carbon ($CoNi_xS_y$/NCP, Fig. 22A),[103] prepared by pyrolysis at 800 °C of a material generated by the reaction of Ni/ZIF-67 with thiourea, was shown to exhibit good OER electrocatalytic activity. The cubic geometry of the MOF precursor was preserved in the Co/NCP and $CoNi_x$/NCP prepared by the pyrolysis of ZIF-67 and Ni/ZIF-67 deposited on N-doped carbon, as well as in $CoNi_xS_y$/NCP, as shown in Fig. 22B–E. Nevertheless, in contrast to Co/NCP (Fig. 22C), $CoNi_x$/NCP (Fig. 22D) and the sulfidation product (Fig. 22E) exhibited porous structures. Interestingly, the incorporation of Ni seemed to increase the degree of crystallinity of cobalt metal in $CoNi_x$/NCP, but that tendency vanished upon sulfidation, giving rise to nine XRD peaks, characteristic of a mixture of $NiCo_2S_4$ and NiS_2, in not well-defined proportions. Such structural and morphologic differences are reflected in the OER overpotentials of the Co/NCP, $CoNi_x$/NCP, and $CoNi_xS_y$/NCP composites, respectively, of 1.62, 1.56, and 1.51 V *vs.* RHE, where the effects of Ni addition and sulfidation are clearly demonstrated. More significant differences were observed in the respective Tafel slopes of 127, 108, and 71 mV, reflecting the increase in the surface area and density of effective active sites, in addition to possible synergic effects enhancing the electrocatalytic activity for the OER.

Wang *et al.* also reacted ZIF-67 with Ni^{2+} but generated a Co–Ni layered double hydroxide (CoNi-LDH) that was hydrothermally reacted with Na_2S in the presence of carbon cloth to grow $NiCo_2S_4$ nanorods directly on the surface ($NiCo_2S_4$@CC). This material exhibited an excellent overpotential of 370 mV at 100 mA cm^{-2},[73] whereas Co/Co_9S_8@NSOC showed η_{50} = 451 mV.[94] Such an enhanced performance of the former at high current densities was attributed to the low internal resistance due to easy ion diffusion and the good electric contact of the nanorods with the carbon cloth, associated with the sulfidation process that also contributed to the increase in the available concentration of active sites while decreasing the metal-anion binding energy.

Zou *et al.*[104] used a similar strategy to prepare a NiCoS composite on $Ti_3C_2T_x$ nanosheets, where T represents terminal groups such as –$(F)_x$ and –$(OH)_x$, denoted NiCoS/$Ti_3C_2T_x$. First, the ZIF-67/$Ti_3C_2T_x$ precursor was reacted with nickel ion and calcined in the presence of CS_2 vapor (Fig. 22G) to obtain a material with η_{10} = 365 mV and Tafel slope = 58.2 mV dec^{-1}, superior to commercial RuO_2 (397 mV and 88.3 mV dec^{-1}). This is an interesting result, considering that MXenes such as $Ti_3C_2T_x$ are known to have good stability and electric
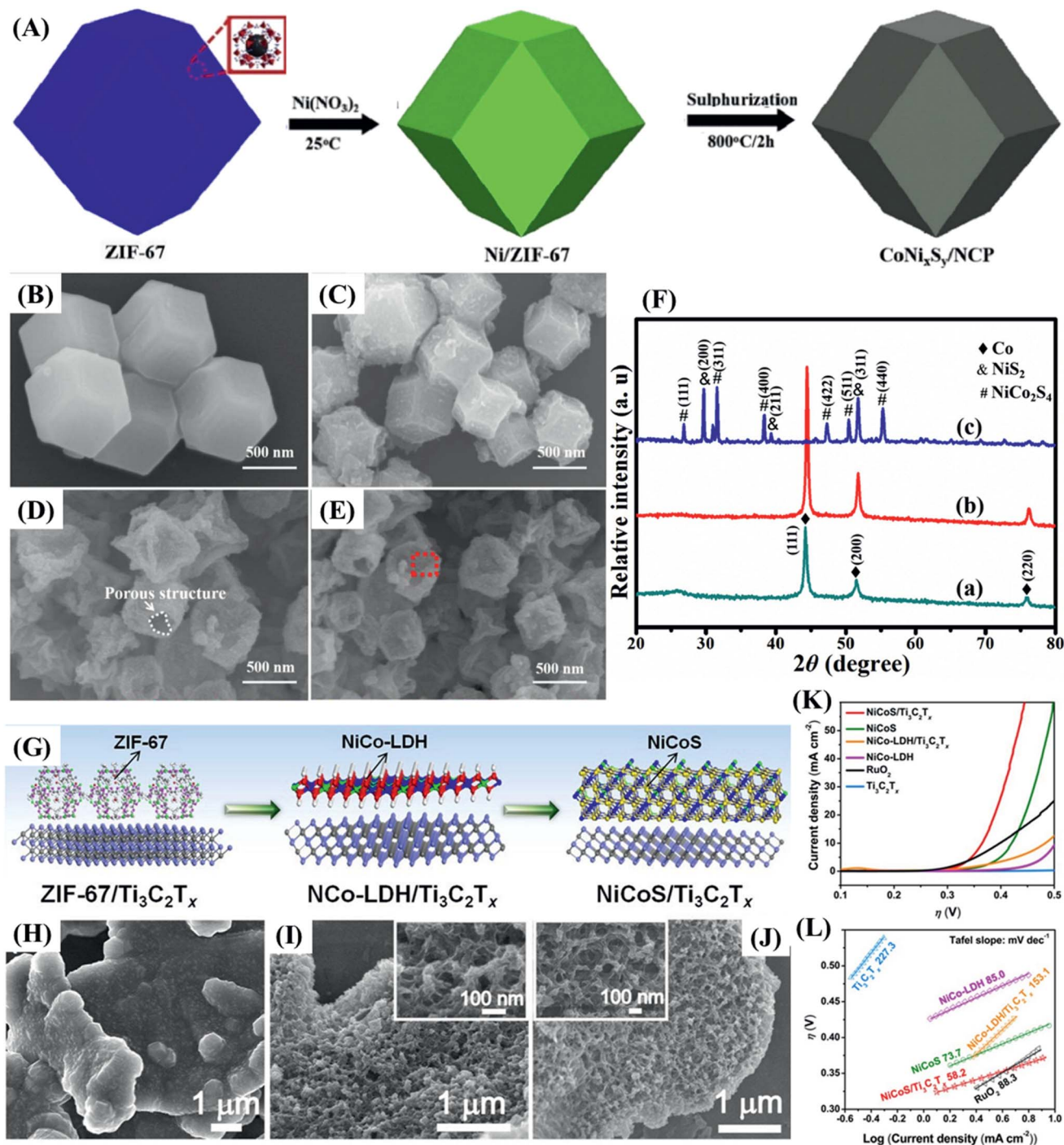
This journal is © The Royal Society of Chemistry 2022

J. Mater. Chem. A, 2022, 10, 430–474 | 465

Fig. 22 (A) Scheme showing the fabrication of the $CoNi_xS_y/NCP$ composite. SEM images of (B) ZIF-67, (C) Co/NC, (D) $CoNi_x/NCP$, and (E) $CoNi_xS_y/NCP$. (F) XRD patterns of (a) Co/NC, (b) $CoNi_x/NCP$, and (c) $CoNi_xS_y/NCP$. Adapted with permission from ref. 103. Copyright© 2019 Hydrogen Energy Publications LLC. Published by Elsevier Ltd. All rights reserved. (G) Scheme depicting the preparation of $NiCoS/Ti_3C_2T_x$. SEM images of (H) $ZIF-67/Ti_3C_2T_x$, (I) $NiCo-LDH/Ti_3C_2T_x$, and (J) $NiCoS/Ti_3C_2T_x$. Inset: the high-magnification SEM images of the samples. (K) LSV curves and (L) Tafel plots of $NiCoS/Ti_3C_2T_x$, NiCoS, $NiCo-LDH/Ti_3C_2T_x$, NiCo-LDH, and RuO_2. Reproduced with permission from ref. 104. Copyright© 2018, American Chemical Society.

conductivity, as well as a favorable hydrophilic surface;[105,106] however, it is not a good catalyst for the OER, presenting a Tafel slope as large as 227.3 mV dec^{-1}. Nevertheless, $NiCoS/Ti_3C_2T_x$ was shown to be the material with the best catalytic performance as compared to NiCoS, $NiCo-LDH/Ti_3C_2T_x$, NiCo-LDH,

and RuO_2 (Fig. 22K and L), clearly demonstrating the relevance of synergic effects.

Interestingly, the doping of NiCo-based materials with Fe ions has proven to be beneficial for the OER catalytic activity.[107–111] One hypothesis is that Fe^{3+} ions can facilitate the

466 | *J. Mater. Chem. A*, 2022, **10**, 430–474

This journal is © The Royal Society of Chemistry 2022

evolution of O_2, or can form the more active Fe^{4+} species that can oxidize water in neutral and alkaline conditions. Another possibility is that the incorporation of Fe^{3+} into Co_3O_4 pushes the Co ions to more active tetrahedral sites. Finally, there is the possibility of synergic interactions of electrochemically generated Ni^{4+} and Fe^{4+} sites, where this species stabilizes the oxyl radical while the former one helps the formation of the O=O bond.[112]

The semi-vulcanization of a Co, Fe-ZIF precursor and graphene oxide, followed by calcination, was used by Liu et al.[113] to prepare $S-Co_{9-x}Fe_xS_8@rGO$, a hybrid $Co_{9-x}Fe_xS_8/Co$, Fe–N–C nanoparticle material wrapped by rGO. This material delivered a $\eta_{10} = 290$ mV, 90 mV less than IrO_2 and up to 115 mV lower than $S-Co_9S_8@rGO$, the monometallic cobalt counterpart, under the same experimental conditions. The corresponding Tafel slopes were respectively 66 and 149 mV dec^{-1}, clearly demonstrating the beneficial effect of Fe-doping on the OER.

Similar results were achieved by Shen et al.[114] who prepared a hybrid N-doped mixed sulfide and carbide of Fe–Ni on carbon cloth, denoted as N–NiFe–S/C@CC, using a one-step carbonization/sulfidation process of NiFe-MOF@CC in the presence of sulfur powder. The material with a molar amount of Ni/Fe of 8:2 (N–NiFe–S/C-8/2@CC) delivered superior OER catalytic performance ($\eta_{10} = 232$ mV) as compared to the monometallic N–Ni–S/C@CC ($\eta_{10} = 308$ mV) and N–Fe–S/C@CC ($\eta_{10} = 329$ mV). Interestingly, all materials exhibited quite low Tafel slopes of 58, 51 and 52 mV dec^{-1}, respectively, as expected for reactions with fast kinetics, as well as good performance in a 20 h stability test at the standard current density of 10 mA cm^{-2}.

The above-mentioned examples led us to infer that trimetallic Ni–Co–Fe catalysts tend to perform even better than their bimetallic counterparts. Wang and collaborators[115] prepared a Ni–Co–Fe–S/rGO composite by the solvothermal reaction of Ni–Co–Fe-PBA/GO with thioacetamide (Fig. 23A), where PBA is a Prussian blue analogue. The mixed sulfide prepared at 160 °C demonstrated the highest activity, which was attributed to the rapid electron transfer rate resulting from the uniform distribution of unidimensional sulfide structures formed at that temperature. The ternary sulfide reached a current density of 10 mA cm^{-2} with an overpotential of 251 mV, significantly less than Co–Fe–S (348 mV), Ni–Co–S/rGO (415 mV), Ni–Fe–S/rGO (366 mV), and RuO_2 (295 mV) under the same conditions (Fig. 23B and E). These good results were confirmed by fast kinetics indicated by the low Tafel slope of 56.4 mV dec^{-1} in comparison with 106.1 (Ni–Co–Fe–S), 98.5 (Ni–Co–S/rGO), 64.6 (Ni–Fe–S/rGO) for the related materials, and 63.5 mV dec^{-1} for RuO_2 (Fig. 23C and D). The ternary material outperformed all others, demonstrating the effect of those metals in decreasing the overpotential and Tafel slope; however, the beneficial effects of the incorporation of highly conducting rGO were also indicated.

It was suggested by Wang et al.[115] that the significant interactions of the 3d orbital in the Ni–Fe–C–S are responsible for an electron density redistribution that optimized the binding energy of oxygen intermediates such as OH* and OOH*, thus minimizing the activation energy (Fig. 23F) and boosting the

OER activity. The electronic configuration of the Ni^{2+} ion is $3d^8$ ($t_{2g}^6 e_g^2$) with fully occupied t_{2g} orbitals, whereas Co^{2+} is $3d^7$ ($t_{2g}^5 e_g^2$) and Fe^{3+} is $3d^5$ ($t_{2g}^3 e_g^2$); the latter one possesses half-filled 3d orbitals that can withdraw electronic density, especially from the sulfide ligands but also from the Ni^{2+} and Co^{2+} ions, consistent with the binding energies measured by XPS, while providing holes for electron diffusion.[115] Such a model is in accord with the Sabatier principle,[116] and the mechanism of four monoelectronic steps proposed for the oxygen evolution reaction.[117,118]

A CoNiFe–S catalyst was produced by the solvothermal processing of ZIF-67 modified with cysteine by Agarwal et al.[120] who studied the influence of the thermal pretreatment of the precursor in the OER activity of that material. The untreated MOF precursor generated CoNiFe–S@ZIF-67, a low crystallinity product with the absence of carbon materials or carbides, suggesting that the carbon present in the precursor dissolved into the solution during the sulfidation stage, or reacted with cysteine to form CS_2. In contrast, when the precursor MOF was heated to 950 °C under an argon atmosphere, and then submitted to the same sulfidation process, CoNiFe–S@GC (GC refers to graphitized carbon) was produced, a material with a higher degree of crystallinity incorporating a pure carbon material and C_3N_4. This material presented an onset potential of 1.56 V as compared with 1.66 V for CoNiFe–S@ZIF-67, a small difference attributed to the formation of carbon–metal covalent bonds that increased the electrical conductivity and durability of the catalyst. The formation of carbon–metal bonds makes the catalyst less susceptible to oxidation, as demonstrated by a 50 h stability test in 1 mol L^{-1} KOH solution, under a current density of 20 mA cm^{-2}.

Another interesting trimetallic combination was presented by Qin et al.[119] who prepared MoCoNiS/NF sulfide on a nickel sponge from a cobalt MOF precursor. This was doped with molybdenum to form MoCo-LDH/NF, whose sulfidation with CH_3CSNH_2 in an autoclave resulted in the desired product (Fig. 23G–J). The sulfide material presented a similar overpotential of $\eta_{10} = 151$ mV in comparison with 175 mV of CoNiS/NF but the Tafel slope decreased from 220.7 mV dec^{-1} to 44.7 mV dec^{-1}, indicating a change in the reaction mechanism leading to a remarkably beneficial effect of Mo (Fig. 23K) in the electrode kinetics.

All the relevant information on the OER electrocatalysts discussed so far are listed in Table 3 where they are classified according to the number of metal ions, as well as the number of citations, the respective precursor MOFs, synthesis routes, catalytic properties and catalytic test conditions. Also, in order to provide a rapid overview of the best strategies for the preparation of high-performance metal sulfide-based OER catalysts, the ten electrodes with the lowest η_{10} overpotential values and Tafel slopes are respectively shown in Fig. 24.

On initially analyzing the values of η_{10} (Fig. 24A), it was observed that carbon materials provide high conductivity and beneficial effects to the electrocatalytic properties of composites for both the HER and OER. However, the monometallic sulfide materials represent one-third of the catalysts in Table 3, and only $Co_{1-x}S@C^{93}$ and $Co_9S_8/NSCNF^{92}$ exhibited overpotentials

This journal is © The Royal Society of Chemistry 2022

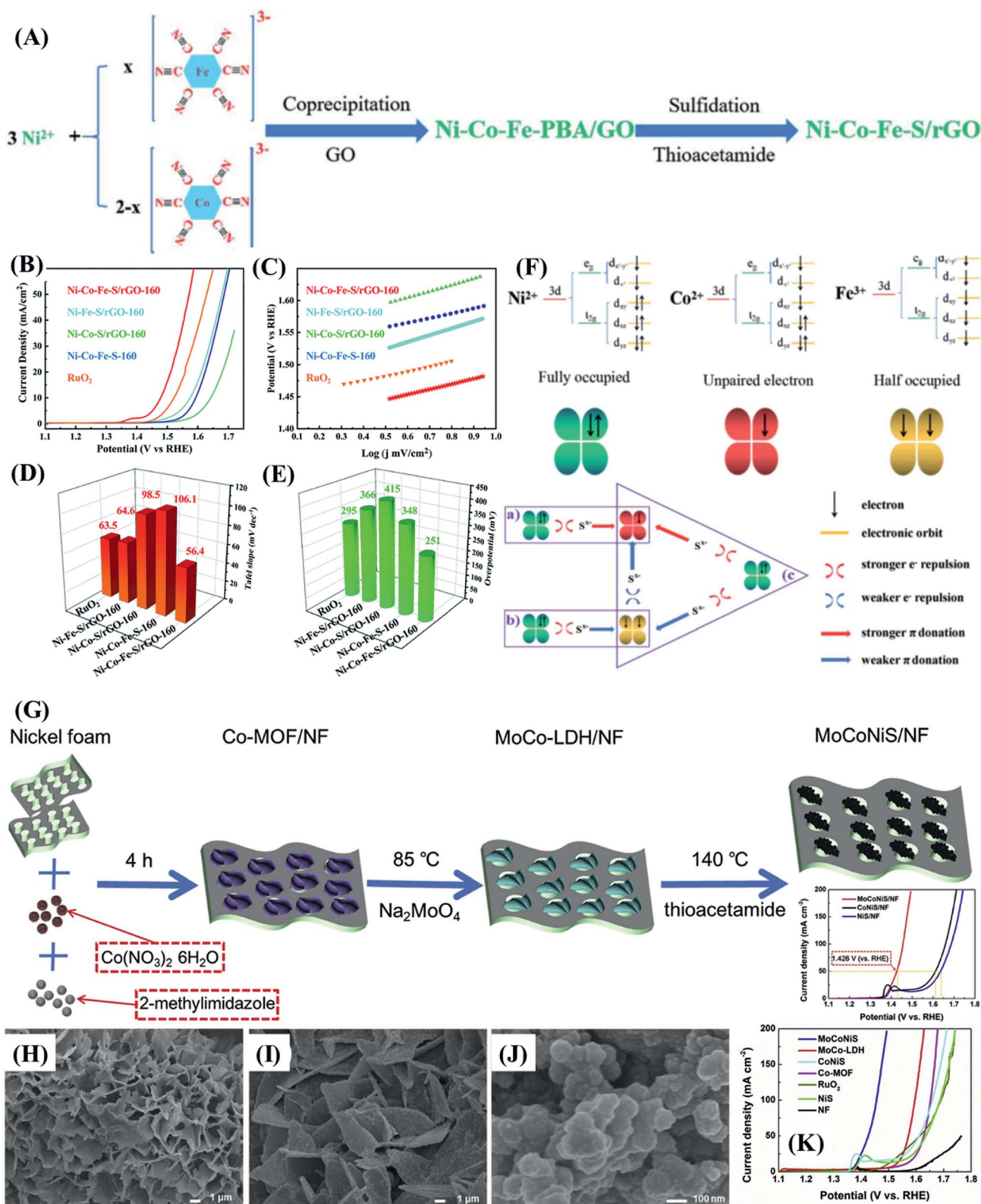J. Mater. Chem. A, 2022, **10**, 430–474 | **467**

Fig. 23 (A) Schematic illustration of the preparation of the Ni–Co–Fe–S/rGO composite, the respective (B) polarization curves, and (C) Tafel plots. Comparison chart of (D) the Tafel slopes and (E) overpotential values of Ni–Co–Fe–S/rGO, Ni–Co–Fe–S, Ni–Co–S/rGO, Ni–Fe–S/rGO and RuO$_2$. (F) (Top) 3d orbital configuration of Ni^{2+}, Co^{2+}, and Fe^{3+}, and (a–c) schematic representations of their electronic coupling in Ni–Co–S/rGO, Ni–Fe–S/rGO, and Ni–Co–Fe–S/rGO. Reproduced with permission.[115] Copyright Marketplace™, Royal Society of Chemistry. (G) Scheme illustrating the synthetic route of the MoCoNiS/NF ternary metal sulfides. SEM images of (H) Co-MOF/NF, (I) MoCo-LDH/NF, and (J) MoCoNiS/NF. (K) Polarization curves of MoCoNiS/NF, MoCo-LDH/NF, Co-MOF/NF, CoNiS/NF, NiS/NF, RuO$_2$/NF, and NF showing their OER performance in 1 M KOH. Reproduced with permission.[119] Copyright© 2019 Hydrogen Energy Publications LLC. Published by Elsevier Ltd. All rights reserved.

Table 3 Relevant performance parameters of recently reported MOF-derived sulfide-based OER electrocatalysts: overpotential at 10 mA cm⁻², onset potential, Tafel slope, stability, and pH conditions used in the activity test[a]

	OER Catalyst derivatives	Precursors	Preparation method	Conducting substrate	Overpotential at 10 mA cm⁻² (η_{10}) (mV vs. RHE)	Tafel slope (mV dec⁻¹)	Stability (h)	pH	Ref
Monometallic	Co_9S_8/GN	ZIF-67	Solvothermal and calcination	GC-RDE	450	176.2	3000 cycles	13	121
	Co_xS_y@C	ZIF-67	Pyrolysis	GCE	470		3.7	13	91
	Co_9S_8/NSCNF	CdS@ZIF	Pyrolysis	GCE	302	54	1000 cycles	14	92
	Co_{1-x}S@C	ZIF-67	Calcination, sulfidation and calcination	CFP	260	85	80	13.6	93
	Co/Co_9S_8@NSOC	Co-NSOMOF	Calcination	GCE	373	80	10	14	94
	Co_9S_8@SNCC	$[Co(Tdc)(Bpy)]_n$	Pyrolysis	GC-RDE	330	80	4.16	13	72
	NiS@N/S–C	Ni-vanillicthio-semicarbazo (NiL_2)	Pyrolysis	CFP	417	48	10	14	95
	NGO/Ni_7S_6	NGO/MOF-74	Solvothermal	GCE	380	45.4	12	13	96
	Ni–Ni_3S_2@carbon	Ni 4,4′-Bpy MOF	Pyrolysis	GCE	284.7	56	8	14	97
	CeO_x/CoS	ZIF-67	Sulfidation and solvothermal	GCE	269	50	20	14	99
	CuO_x NWs@CoS_2	CuO_x NWs@ZIF-67	Calcination and sulfidation	Cu foam	210	180	14	14	98
	CoS_x@MoS_2	Co-MOF	Two-step solvothermal	GCE	347	147	500 cycles	14	84
	CoS_2-MoS_8HNSa/Ti	Co-MOF arrays/Ti	Na_2MoO_4 etching and pyrolysis	Ti	266	104	24	14	85
Bimetallic	WS_2/Co_{1-x}S/N,S co-doped carbon	ZIF-67	Pyrolysis	GCE	365	53	2.2	14	88
	$CoNi_xS_y$/NCP	Ni/ZIF-67	Pyrolysis	GCE	1.51 V (absolute potential)	71	10	14	103
	$NiCo_2S_4$@CC	Ni/ZIF-67	Pyrolysis	CCE	370 (at 100 mA cm⁻²)	95.76	20	14	73
	NiCoS/$Ti_3C_2T_x$	Ni/ZIF-67/$Ti_3C_2T_x$	Pyrolysis	GCE	365	58.2	6	14	104
	S–$Co_{9-x}Fe_xS_8$@rGO	Co, Fe-ZIF	Semi-vulcanization and calcination	GC-RDE	290	66	11	13	113
Trimetallic	N–NiFe-S/C-8/2@CC	NiFe-MOF@CC	Sulfidation	CCE	232	58	20	14	114
	Ni–Co–Fe-S/rGO	Ni–Co–Fe-PBA/GO	Solvothermal	GCE	251	56.4	36	14	115
	CoNiFe-S@GC	ZIF-67	Calcination and solvothermal	Carbon paper			50	13	120
	MoCoNiS/NF	ZIF-67	Solvothermal	NF	151	44.7	10	14	119

[a] GCE = glassy carbon electrode; GC-RDE = glassy carbon rotating disk electrode; CFP = carbon fiber paper; CC = carbon cloth; NF = nickel foam.
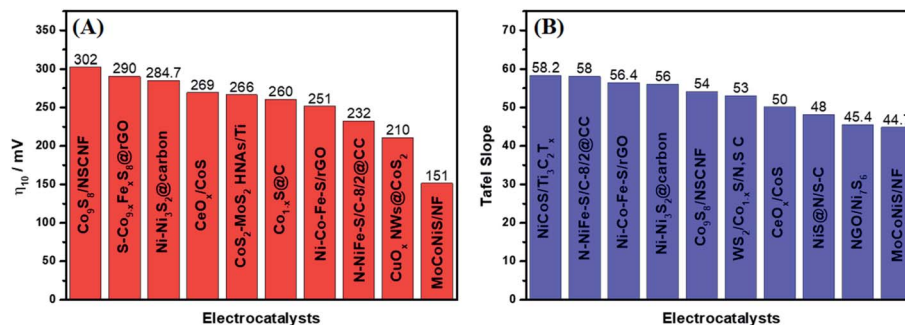
Fig. 24 The top ten sulfide-based electrocatalysts derived from MOFs considering (A) the η_{10} overpotential values and (B) the Tafel slopes.

that were low enough (Fig. 24). Ni–Ni$_3$S$_2$@carbon[97] cannot be strictly considered since it contains, in addition to Ni^{2+}, metallic nickel, which contributes to further lowering its overpotential to a value inferior to that of catalysts such as NiS@N/S–C (417 mV)[95] and NGO/Ni$_7$S$_6$ (380 mV)[96] based only on nickel ions. Also, it is remarkable that there are two composites based on oxide catalysts (CuO$_x$ NWs@CoS$_2$ and CeO$_x$/CoS[98,99]), which exhibit low η_{10}; however, the studies on such materials are few, and more studies are necessary to support further assumptions.

Doping with iron ions as shown in Fig. 24A is a positive factor influencing the overpotential in bi- and trimetallic sulfides. Trimetallic sulfides are considered one of the most promising materials, as evidenced by the fact that two of the three trimetallic composites are in the group of materials with the lowest overpotentials, including the best of all, the MoCoNiS/NF trimetallic sulfide electrode. A similar conclusion can be reached by considering Fig. 24B, where the monometallic materials with the ten lowest Tafel slopes are few, indicating that more than one metallic element tends to enhance the electrode kinetics for the OER of trimetallic materials such as CoNiFe–S@GC.[120] It is also evident on comparing Fig. 24A and B that catalysts with low overpotentials do not necessarily exhibit fast reaction kinetics and low Tafel slopes. This can be illustrated by the NiS@N/S–C and NGO/Ni$_7$S$_6$, which have high overpotentials for the OER but very low Tafel slopes similar to that of MoCoNiS/NF, the material exhibiting the lowest value, according to the best of our knowledge. This means that the best should probably be applied in electrocatalytic materials with the best combination of overpotential and electrode kinetics, as well as high performance at high current densities. MoCoNiS/NF seems to fulfill such requirements, exhibiting $\eta_{100} = 226$ mV, which is lower than the 370 mV achieved with NiCo$_2$S$_4$@CC.[73]

6. Summary and outlook

The urgent need for sustainable energy sources makes the development of robust, highly efficient, and low-cost energy conversion and storage technologies highly desired. In this sense, a water society relying on hydrogen from water-splitting as a renewable energy source is strongly appealing but efficient electrocatalytic materials are required to decrease the overpotential of that reaction and overcome the kinetically

limited multielectronic and multiprotonic process of H$_2$ and O$_2$ production. In this context, high-performance, high-density energy storage materials and devices, especially at high power densities, such as batteries and supercapacitors, as well as fuel cells, are key and complementary technologies.

Transition metal sulfides are among the most studied materials for these applications, having high theoretical specific capacitance, redox reversibility, and intrinsic conductivity in comparison to other promising materials such as transition metal hydroxides and oxides. Even though transition metal oxides are the most studied among these three materials, the substitution of oxygen by sulfur generates more flexible systems due to sulfur's lower electronegativity, which reduces the volume variation during charge/discharge processes, leading to more stable structures. Those properties are even more optimized in transition metal sulfides composed of mixed metallic centers, such as bi- and trimetallic sulfides, presenting multielectronic redox-active sites, superior stability, higher charge/electron transfer rates, more controllable structural features and lower band-gaps, due to synergistic effects provided by the different active sites with multiple oxidation states. However, these properties are not enough to make the materials competitive. Their electrical conductivity and cycling stability can hinder their electrochemical performances and need to be further improved.

Fabricating nanostructures with advantageous new architectures has been considered an effective strategy for improving the electrochemical performance and overcoming the downsides of transition metal sulfides. Thus, MOF-derived transition metal sulfides are among the most promising materials since they take advantage of all the inherent structural tunability of the MOF precursor, which can exhibit several morphologies, well-ordered structures with large surface area, high porosity, abundant available faradaic reaction sites, and decreased diffusion resistance of electrolytes, features that can be preserved or improved in the active materials. Their electrochemical performance can be further increased by the production of the following. (1) Hollow porous transition metal sulfide nanoparticles with larger specific surface area, plenty of electroactive sites in contact with the electrolyte, greatly shorten the ion and charge diffusion distances, speed up the charge–discharge processes and increase the effective electroactive surface areas, thus enhancing both the energy storage and

electrocatalytic activity, in addition to alleviating the volume expansion during electrochemical processes due to their hollow nature, preventing structural distortion and increasing the cycling stability. (2) Nanocomposites and hybrid materials with supported, embedded, and interconnected structures, *e.g.*, by the production of transition metal sulfide nanoparticles during the sulfidation of MOF nanoarrays directly grown on carbon nanotubes (CNTs) or reduced graphene oxide (rGO), providing stronger adhesion and tight contact of the conductive and electroactive materials, increased electroactive surface area and preventing agglomeration due to the oriented growth of MOF nanoarrays. (3) Binder-free electrodes by the direct growth of MOFs nanoarrays on, *e.g.*, nickel foam (NF) and carbon cloth (CC), for the production of self-supporting electrodes, eliminating the binder additive and reducing the "dead-mass" loading may introduce unacceptable series resistances while reducing the effective electroactive surface area. (4) Core@shell heterostructures with highly conductive cores, acting as support and electron transmission channels, and highly electroactive shells, providing abundant multi-redox electrochemical active sites and enhanced double-layer capacitance, as well as superior overall stability, porosity, electroactive surface area, density of active sites, ion-diffusion rate and electrical conductivity. Most of the best materials presented in this review were based on binder-free electrodes composed of transition metal sulfides in a core@shell nanostructure and hybrid nanocomposite materials, especially bi- and trimetallic ones, as inferred by analyzing Fig. 14 and comparing the top 10 OER and HER electrocatalysts and supercapacitor electrode materials. Such structural strategies could be explored given the unique characteristics of MOFs and MOF-derived materials, which provide incredibly suitable morphology and composition control, enabling the production of new materials with impressive OER and HER electrocatalytic performances, and also application in supercapacitor devices.

Despite the promising progress made in the design of MOF-derived sulfides, it is important to highlight that the challenges that still need to be overcome to realize electrode materials suitable for real application and commercialization of energy conversion and storage devices are great. For instance, the optimization of the mass ratio of TMSs/conductive carbon is crucial for obtaining materials with higher energy and power densities. Furthermore, in the case of supercapacitor devices, the rational development of both electrodes and electrolytes is equally important.[20]

Considering the great feasibility of using MOF-derived sulfides and other MOF-derived materials in energy storage and conversion technologies, another important challenge is the development of simple fabrication protocols to realize low-cost devices. Considering the large-scale production of affordable energy electrode materials, the use of laser-based techniques in the synthesis[122] and improvement of electrode materials[123] is an excellent alternative to the time-consuming step of thermal treatment for the preparation of MOF-derived materials. It is also possible to highlight the design of miniaturized and flexible energy storage and conversion devices by the incorporation of MOF-derived materials and composites in inks to realize mass production by screen-printing, ink-jet printing, or 3D printing, toward a more sustainable society in the future. In short, despite all the theoretical and experimental background on electrodes and electrocatalytic materials, which clearly describe all ideal features, the quest continues for materials based on low-cost transition metal ions and elements with suitable electronic, binding, electrochemical and mechanical properties in order to fulfill the continuously growing energy needs of our society.

Conflicts of interest

There are no conflicts to declare.

Acknowledgements

References

1 H. Zhao, L. Liu and Y. Lei, *Front. Chem. Sci. Eng.*, 2018, **12**, 481–493.

2 L. Zhang and Z. Chen, *Int. J. Energy Res.*, 2020, **44**, 3316–3346.

3 J. M. Gonçalves, M. N. T. Silva, K. K. Naik, P. R. Martins, D. P. Rocha, E. Nossol, R. A. A. Munoz, L. Angnes and C. S. Rout, *J. Mater. Chem. A*, 2021, **9**, 3095–3124.

4 Y. Liu, X. Xu, Z. Shao and S. P. Jiang, *Energy Storage Mater.*, 2020, **26**, 1–22.

5 S. Sanati, R. Abazari, J. Albero, A. Morsali, H. García, Z. Liang and R. Zou, *Angew. Chem., Int. Ed.*, 2021, **60**, 11048–11067.

6 G. Yilmaz, K. M. Yam, C. Zhang, H. J. Fan and G. W. Ho, *Adv. Mater.*, 2017, **29**, 1606814.

7 Y. Wang, B. Li, B. Zhang, S. Tian, X. Yang, H. Ye, Z. Xia and G. Zheng, *J. Electroanal. Chem.*, 2020, **878**, 114576.

8 J. M. Gonçalves, P. R. Martins, B. G. Santos, K. Araki and L. Angnes, in *Reference Module in Biomedical Sciences*, Elsevier, 2021, DOI: 10.1016/B978-0-12-822548-6.00002-9.

9 J. M. Gonçalves, P. Roberto Martins, D. P. Rocha, T. A. Matias, M. S. Julião, R. A. Abarza Munoz and L. Angnes, *J. Mater. Chem. C*, 2021, **9**, 8718–8745.

10 Y. Li, J. Zhang and M. Chen, *Sustainable Mater. Technol.*, 2020, **26**, e00217.

11 R. Ahmad, U. A. Khan, N. Iqbal and T. Noor, *RSC Adv.*, 2020, **10**, 43733–43750.

12 D. Chen, L. Wei, J. Li and Q. Wu, *J. Energy Storage*, 2020, **30**, 101525.

13 Z. Ye, Y. Jiang, L. Li, F. Wu and R. Chen, *Nano-Micro Lett.*, 2021, **13**, 203.

14 X. Wen and J. Guan, *Appl. Mater. Today*, 2019, **16**, 146–168.

This journal is © The Royal Society of Chemistry 2022

J. Mater. Chem. A, 2022, **10**, 430–474 | **471**

15 Q. Shao, J. Yang and X. Huang, *Chem.–Eur. J.*, 2018, **24**, 15143–15155.

16 R. B. Choudhary, S. Ansari and M. Majumder, *Renewable Sustainable Energy Rev.*, 2021, **145**, 110854.

17 B. Yan, X. Li, W. Xiao, J. Hu, L. Zhang and X. Yang, *J. Mater. Chem. A*, 2020, **8**, 17848–17882.

18 Y.-Y. Liu, L. Xu, X.-T. Guo, T.-T. Lv and H. Pang, *J. Mater. Chem. A*, 2020, **8**, 20781–20802.

19 Y. V. Lim, X. L. Li and H. Y. Yang, *Adv. Funct. Mater.*, 2021, **31**, 2006761.

20 Y. Gao and L. Zhao, *Chem. Eng. J.*, 2022, **430**, 132745.

21 A. Sakuda, T. Takeuchi, K. Okamura, H. Kobayashi, H. Sakaebe, K. Tatsumi and Z. Ogumi, *Sci. Rep.*, 2014, **4**, 4883.

22 J. M. Gonçalves, M. I. da Silva, M. Hasheminejad, H. E. Toma, K. Araki, P. R. Martins and L. Angnes, *Batteries Supercaps*, 2021, **4**, 1397.

23 R. Zhang, C. Pan, R. G. Nuzzo and A. A. Gewirth, *J. Phys. Chem. C*, 2019, **123**, 8740–8745.

24 L. G. Beka, X. Li, X. Wang, C. Han and W. Liu, *RSC Adv.*, 2019, **9**, 26637–26645.

25 Y. Li, Z. Yin, M. Cui, X. Liu, J. Xiong, S. Chen and T. Ma, *J. Mater. Chem. A*, 2021, **9**, 2070–2092.

26 Y. Zhao, M. Bi, F. Qian, P. Zeng, M. Chen, R. Wang, Y. Liu, Y. Ding and Z. Fang, *ChemElectroChem*, 2018, **5**, 3953–3960.

27 L. Shang, H. Yu, X. Huang, T. Bian, R. Shi, Y. Zhao, G. I. N. Waterhouse, L.-Z. Wu, C.-H. Tung and T. Zhang, *Adv. Mater.*, 2016, **28**, 1668–1674.

28 H. Zhou, D. He, A. I. Saana, J. Yang, Z. Wang, J. Zhang, Q. Liang, S. Yuan, J. Zhu and S. Mu, *Nanoscale*, 2018, **10**, 6147–6154.

29 S. Soni, P. K. Bajpai and C. Arora, *Charact. Appl. Nanomater.*, 2020, **3**, 87–106.

30 N. Stock and S. Biswas, *Chem. Rev.*, 2012, **112**, 933–969.

31 Y.-R. Lee, J. Kim and W.-S. Ahn, *Korean J. Chem. Eng.*, 2013, **30**, 1667–1680.

32 C. M. Oliva González, B. I. Kharisov, O. V. Kharissova and T. E. Serrano Quezada, *Mater. Today: Proc.*, 2021, **46**, 3018–3029.

33 C. Singh, S. Mukhopadhyay and I. Hod, *Nano Convergence*, 2021, **8**, 1.

34 X. F. Lu, Y. Fang, D. Luan and X. W. D. Lou, *Nano Lett.*, 2021, **21**, 1555–1565.

35 Y. Jiang and J. Liu, *Energy Environ. Mater.*, 2019, **2**, 30–37.

36 J. M. Gonçalves, P. R. Martins, K. Araki and L. Angnes, *J. Energy Chem.*, 2021, **57**, 496–515.

37 N. R. Chodankar, H. D. Pham, A. K. Nanjundan, J. F. S. Fernando, K. Jayaramulu, D. Golberg, Y.-K. Han and D. P. Dubal, *Small*, 2020, **16**, 2002806.

38 P. Simon, Y. Gogotsi and B. Dunn, *Science*, 2014, **343**, 1210.

39 J. M. Gonçalves, M. I. da Silva, H. E. Toma, L. Angnes, P. R. Martins and K. Araki, *J. Mater. Chem. A*, 2020, **8**, 10534–10570.

40 A. P. Gomes, J. M. Gonçalves, K. Araki and P. R. Martins, *Energy Technol.*, 2019, **7**, 1800980.

41 J. M. Goncalves, R. R. Guimaraes, C. V. Nunes, A. Duarte, B. B. N. S. Brandao, H. E. Toma and K. Araki, *RSC Adv.*, 2016, **6**, 102504–102512.

42 J. G. Ruiz-Montoya, V. L. Quispe-Garrido, J. C. Calderón Gómez, A. M. Baena Moncada and J. M. Gonçalves, *Sustainable Energy Fuels*, 2021, **5**, 5332–5365.

43 L. Cheng, S. Chen, Q. Zhang, Y. Li, J. Chen and Y. Lou, *J. Energy Storage*, 2020, **31**, 101663.

44 J. Liu, X. Deng, S. Zhu, N. Zhao, J. Sha, L. Ma and F. He, *Electrochim. Acta*, 2021, **368**, 137528.

45 T. S. Mathis, N. Kurra, X. Wang, D. Pinto, P. Simon and Y. Gogotsi, *Adv. Energy Mater.*, 2019, **9**, 1902007.

46 J. M. Gonçalves, A. Kumar, M. I. da Silva, H. E. Toma, P. R. Martins, K. Araki, M. Bertotti and L. Angnes, *Energy Technol.*, 2021, **9**, 2000927.

47 Y. Zhai, X. Ren, J. Yan and S. Liu, *Small Struct.*, 2021, **2**, 2000096.

48 J. M. Gonçalves, M. Ireno da Silva, L. Angnes and K. Araki, *J. Mater. Chem. A*, 2020, **8**, 2171–2206.

49 B. Seo and S. H. Joo, *Nano Convergence*, 2017, **4**, 19.

50 R. Guidelli, R. G. Compton, J. M. Feliu, E. Gileadi, J. Lipkowski, W. Schmickler and S. Trasatti, *Pure Appl. Chem.*, 2014, **86**, 245–258.

51 N.-T. Suen, S.-F. Hung, Q. Quan, N. Zhang, Y.-J. Xu and H. M. Chen, *Chem. Soc. Rev.*, 2017, **46**, 337–365.

52 H. Jia, Z. Wang, X. Zheng, Y. Cai, J. Lin, H. Liang, J. Qi, J. Cao, J. Feng and W. Fei, *Electrochim. Acta*, 2019, **312**, 54–61.

53 Q. Yang, Y. Liu, L. Xiao, M. Yan, F. Bai, F. Zhu, Y. Lei and W. Shi, *Chem. Eng. J.*, 2018, **354**, 716–726.

54 Q. Yang, Y. Liu, M. Yan, Y. Lei and W. Shi, *Chem. Eng. J.*, 2019, **370**, 666–676.

55 M. S. Javed, H. Lei, J. Li, Z. Wang and W. Mai, *J. Mater. Chem. A*, 2019, **7**, 17435–17445.

56 Y. Wang, J. Huang, Y. Xiao, Z. Peng, K. Yuan, L. Tan and Y. Chen, *Carbon*, 2019, **147**, 146–153.

57 K. Le, M. Gao, W. Liu, J. Liu, Z. Wang, F. Wang, V. Murugadoss, S. Wu, T. Ding and Z. Guo, *Electrochim. Acta*, 2019, **323**, 134826.

58 Y.-P. Liu, X.-H. Qi, L. Li, S.-H. Zhang and T. Bi, *Ceram. Int.*, 2019, **45**, 17216–17223.

59 B. Chameh, M. Moradi and S. Kaveian, *Synth. Met.*, 2020, **260**, 116262.

60 W. Zhao, Y. Zheng, L. Cui, D. Jia, D. Wei, R. Zheng, C. Barrow, W. Yang and J. Liu, *Chem. Eng. J.*, 2019, **371**, 461–469.

61 Z.-X. Li, B.-L. Yang, Y.-F. Jiang, C.-Y. Yu and L. Zhang, *Cryst. Growth Des.*, 2018, **18**, 979–992.

62 K.-Y. Zou, Y.-C. Liu, Y.-F. Jiang, C.-Y. Yu, M.-L. Yue and Z.-X. Li, *Inorg. Chem.*, 2017, **56**, 6184–6196.

63 M. Yi, C. Zhang, C. Cao, C. Xu, B. Sa, D. Cai and H. Zhan, *Inorg. Chem.*, 2019, **58**, 3916–3924.

64 Y. Yang, M.-L. Li, J.-N. Lin, M.-Y. Zou, S.-T. Gu, X.-J. Hong, L.-P. Si and Y.-P. Cai, *Inorg. Chem.*, 2020, **59**, 2406–2412.

65 R. Tian, Y. Zhou, H. Duan, Y. Guo, H. Li, K. Chen, D. Xue and H. Liu, *ACS Appl. Energy Mater.*, 2018, **1**, 402–410.

66 H. Chen, M. Q. Wang, Y. Yu, H. Liu, S.-Y. Lu, S.-J. Bao and M. Xu, *ACS Appl. Energy Mater.*, 2017, **9**, 35040–35047.

67 Q. Yang, Q. Wang, Y. Long, F. Wang, L. Wu, J. Pan, J. Han, Y. Lei, W. Shi and S. Song, *Adv. Energy Mater.*, 2020, **10**, 1903193.

68 Y. Huang, L. Quan, T. Liu, Q. Chen, D. Cai and H. Zhan, *Nanoscale*, 2018, **10**, 14171–14181.

69 H. Niu, Y. Liu, B. Mao, N. Xin, H. Jia and W. Shi, *Electrochim. Acta*, 2020, **329**, 135130.

70 Q. Cheng, C. Yang, K. Tao and L. Han, *Electrochim. Acta*, 2020, **341**, 136042.

71 G.-C. Li, M. Liu, M.-K. Wu, P.-F. Liu, Z. Zhou, S.-R. Zhu, R. Liu and L. Han, *RSC Adv.*, 2016, **6**, 103517–103522.

72 S. Liu, M. Tong, G. Liu, X. Zhang, Z. Wang, G. Wang, W. Cai, H. Zhang and H. Zhao, *Inorg. Chem. Front.*, 2017, **4**, 491–498.

73 D. Wang, L. Tian, J. Huang, D. Li, J. Liu, Y. Xu, H. Ke and Q. Wei, *Electrochim. Acta*, 2020, **334**, 135636.

74 C. Qu, L. Zhang, W. Meng, Z. Liang, B. Zhu, D. Dang, S. Dai, B. Zhao, H. Tabassum, S. Gao, H. Zhang, W. Guo, R. Zhao, X. Huang, M. Liu and R. Zou, *J. Mater. Chem. A*, 2018, **6**, 4003–4012.

75 W. Sun, Y. Du, G. Wu, G. Gao, H. Zhu, J. Shen, K. Zhang and G. Cao, *J. Mater. Chem. A*, 2019, **7**, 7138–7150.

76 Q. Yang, Y. Liu, C. Deng, M. Yan and W. Shi, *J. Mater. Chem. A*, 2019, **7**, 26131–26138.

77 Q. Wang, F. Gao, B. Xu, F. Cai, F. Zhan, F. Gao and Q. Wang, *Chem. Eng. J.*, 2017, **327**, 387–396.

78 S. Fu, L. Ma, M. Gan, J. Shen, T. Li, X. Zhang, W. Zhan, F. Xie and J. Yang, *J. Alloys Compd.*, 2021, **859**, 157798.

79 P. Cai, T. Liu, L. Zhang, B. Cheng and J. Yu, *Appl. Surf. Sci.*, 2020, **504**, 144501.

80 Z. Liang, R. Zhao, T. Qiu, R. Zou and Q. Xu, *EnergyChem*, 2019, **1**, 100001.

81 Y. Liu, D. Huang, M. Cheng, Z. Liu, C. Lai, C. Zhang, C. Zhou, W. Xiong, L. Qin, B. Shao and Q. Liang, *Coord. Chem. Rev.*, 2020, **409**, 213220.

82 K. Ao, Q. Wei and W. A. Daoud, *ACS Appl. Energy Mater.*, 2020, **12**, 33595–33602.

83 W. He, R. Ifraemov, A. Raslin and I. Hod, *Adv. Funct. Mater.*, 2018, **28**, 1707244.

84 L. Yang, L. Zhang, G. Xu, X. Ma, W. Wang, H. Song and D. Jia, *ACS Sustainable Chem. Eng.*, 2018, **6**, 12961–12968.

85 Y. Li, W. Wang, B. Huang, Z. Mao, R. Wang, B. He, Y. Gong and H. Wang, *J. Energy Chem.*, 2021, **57**, 99–108.

86 G. Yilmaz, T. Yang, Y. Du, X. Yu, Y. P. Feng, L. Shen and G. W. Ho, *Adv. Sci.*, 2019, **6**, 1900140.

87 H. Xu, X. Niu, Z. Liu, M. Sun, Z. Liu, Z. Tian, X. Wu, B. Huang, Y. Tang and C.-H. Yan, *Small*, 2021, 2103064.

88 Z. Huang, Z. Yang, M. Z. Hussain, B. Chen, Q. Jia, Y. Zhu and Y. Xia, *Electrochim. Acta*, 2020, **330**, 135335.

89 C. Wu, Y. Du, Y. Fu, W. Wang, T. Zhan, Y. Liu, Y. Yang and L. Wang, *Composites, Part B*, 2019, **177**, 107252.

90 M. Tahir, L. Pan, F. Idrees, X. Zhang, L. Wang, J.-J. Zou and Z. L. Wang, *Nano Energy*, 2017, **37**, 136–157.

91 B. Chen, R. Li, G. Ma, X. Gou, Y. Zhu and Y. Xia, *Nanoscale*, 2015, **7**, 20674–20684.

92 L.-L. Wu, Q.-S. Wang, J. Li, Y. Long, Y. Liu, S.-Y. Song and H.-J. Zhang, *Small*, 2018, **14**, 1704035.

93 D. He, X. Wu, W. Liu, C. Lei, C. Yu, G. Zheng, J. Pan, L. Lei and X. Zhang, *Chin. Chem. Lett.*, 2019, **30**, 229–233.

94 J. Du, R. Wang, Y.-R. Lv, Y.-L. Wei and S.-Q. Zang, *Chem. Commun.*, 2019, **55**, 3203–3206.

95 L. Yang, M. Gao, B. Dai, X. Guo, Z. Liu and B. Peng, *Electrochim. Acta*, 2016, **191**, 813–820.

96 K. Jayaramulu, J. Masa, O. Tomanec, D. Peeters, V. Ranc, A. Schneemann, R. Zboril, W. Schuhmann and R. A. Fischer, *Adv. Funct. Mater.*, 2017, **27**, 1700451.

97 Y. Lin, G. Chen, H. Wan, F. Chen, X. Liu and R. Ma, *Small*, 2019, **15**, 1900348.

98 G. Prasad Ojha, A. Muthurasu, A. Prasad Tiwari, B. Pant, K. Chhetri, T. Mukhiya, B. Dahal, M. Lee, M. Park and H.-Y. Kim, *Chem. Eng. J.*, 2020, **399**, 125532.

99 H. Xu, J. Cao, C. Shan, B. Wang, P. Xi, W. Liu and Y. Tang, *Angew. Chem., Int. Ed.*, 2018, **57**, 8654–8658.

100 Y. Zhang, X. Cao, H. Yuan, W. Zhang and Z. Zhou, *Int. J. Hydrogen Energy*, 1999, **24**, 529–536.

101 Z.-Q. Liu, G.-F. Chen, P.-L. Zhou, N. Li and Y.-Z. Su, *J. Power Sources*, 2016, **317**, 1–9.

102 F. J. Pérez-Alonso, C. Adán, S. Rojas, M. A. Peña and J. L. G. Fierro, *Int. J. Hydrogen Energy*, 2015, **40**, 51–61.

103 Y. Zheng, L. Zhang, H. Huang, F. Wang, L. Yin, H. Jiang, D. Wang, J. Yang and G. Zuo, *Int. J. Hydrogen Energy*, 2019, **44**, 27465–27471.

104 H. Zou, B. He, P. Kuang, J. Yu and K. Fan, *ACS Appl. Energy Mater.*, 2018, **10**, 22311–22319.

105 M. R. Lukatskaya, O. Mashtalir, C. E. Ren, Y. Dall'Agnese, P. Rozier, P. L. Taberna, M. Naguib, P. Simon, M. W. Barsoum and Y. Gogotsi, *Science*, 2013, **341**, 1502.

106 L. Zhao, B. Dong, S. Li, L. Zhou, L. Lai, Z. Wang, S. Zhao, M. Han, K. Gao, M. Lu, X. Xie, B. Chen, Z. Liu, X. Wang, H. Zhang, H. Li, J. Liu, H. Zhang, X. Huang and W. Huang, *ACS Nano*, 2017, **11**, 5800–5807.

107 S. Klaus, Y. Cai, M. W. Louie, L. Trotochaud and A. T. Bell, *J. Phys. Chem. C*, 2015, **119**, 7243–7254.

108 M. S. Burke, M. G. Kast, L. Trotochaud, A. M. Smith and S. W. Boettcher, *J. Am. Chem. Soc.*, 2015, **137**, 3638–3648.

109 L. Trotochaud, S. L. Young, J. K. Ranney and S. W. Boettcher, *J. Am. Chem. Soc.*, 2014, **136**, 6744–6753.

110 J. M. Gonçalves, P. R. Martins, L. Angnes and K. Araki, *New J. Chem.*, 2020, **44**, 9981–9997.

111 J. M. Gonçalves, T. A. Matias, K. C. F. Toledo and K. Araki, in *Advances in Inorganic Chemistry*, ed. R. v. Eldik and C. Hubbard, Elsevier, 2019, vol. 74, p. 63.

112 S. Anantharaj, S. Kundu and S. Noda, *Nano Energy*, 2021, **80**, 105514.

113 T. Liu, F. Yang, G. Cheng and W. Luo, *Small*, 2018, **14**, 1703748.

114 Y. Shen, L. Wang, P. Jiang, W. S. V. Lee and J. Xue, *ChemElectroChem*, 2019, **6**, 2741–2747.

115 B. Wang, Y. Chen, X. Wang, J. Ramkumar, X. Zhang, B. Yu, D. Yang, M. Karpuraranjith and W. Zhang, *J. Mater. Chem. A*, 2020, **8**, 13558–13571.

116 K. S. Exner, *ACS Catal.*, 2019, **9**, 5320–5329.

This journal is © The Royal Society of Chemistry 2022

J. Mater. Chem. A, 2022, **10**, 430–474 | **473**

117 N. Yu, W. Cao, M. Huttula, Y. Kayser, P. Hoenicke, B. Beckhoff, F. Lai, R. Dong, H. Sun and B. Geng, *Appl. Catal., B*, 2020, **261**, 118193.

118 F. Godínez-Salomón, L. Albiter, S. M. Alia, B. S. Pivovar, L. E. Camacho-Forero, P. B. Balbuena, R. Mendoza-Cruz, M. J. Arellano-Jimenez and C. P. Rhodes, *ACS Catal.*, 2018, **8**, 10498–10520.

119 J.-F. Qin, M. Yang, T.-S. Chen, B. Dong, S. Hou, X. Ma, Y.-N. Zhou, X.-L. Yang, J. Nan and Y.-M. Chai, *Int. J. Hydrogen Energy*, 2020, **45**, 2745–2753.

120 S. Agarwal, X. Yu and A. Manthiram, *Mater. Today Energy*, 2020, **16**, 100405.

121 X. Sun, Q. Gong, Y. Liang, M. Wu, N. Xu, P. Gong, S. Sun and J. Qiao, *ACS Appl. Energy Mater.*, 2020, **12**, 38202–38210.

122 P. García Lebière, A. Pérez del Pino, C. Logofatu and E. György, *Appl. Surf. Sci.*, 2021, **563**, 150234.

123 D. P. Rocha, V. N. Ataide, A. de Siervo, J. M. Gonçalves, R. A. A. Muñoz, T. R. L. C. Paixão and L. Angnes, *Chem. Eng. J.*, 2021, **425**, 130594.

474 | *J. Mater. Chem. A*, 2022, **10**, 430–474

This journal is © The Royal Society of Chemistry 2022